

2011-07-18

# The Design of a Polarimeter and its Use for the Study of the Variation of Downwelling Polarized Radiance Distribution with Depth in the Ocean

Purushottam Bhandari

*University of Miami*, [puru@physics.miami.edu](mailto:puru@physics.miami.edu)

Follow this and additional works at: [https://scholarlyrepository.miami.edu/oa\\_dissertations](https://scholarlyrepository.miami.edu/oa_dissertations)

---

## Recommended Citation

Bhandari, Purushottam, "The Design of a Polarimeter and its Use for the Study of the Variation of Downwelling Polarized Radiance Distribution with Depth in the Ocean" (2011). *Open Access Dissertations*. 605.

[https://scholarlyrepository.miami.edu/oa\\_dissertations/605](https://scholarlyrepository.miami.edu/oa_dissertations/605)

This Open access is brought to you for free and open access by the Electronic Theses and Dissertations at Scholarly Repository. It has been accepted for inclusion in Open Access Dissertations by an authorized administrator of Scholarly Repository. For more information, please contact [repository.library@miami.edu](mailto:repository.library@miami.edu).

UNIVERSITY OF MIAMI

THE DESIGN OF A POLARIMETER AND ITS USE FOR THE STUDY OF THE  
VARIATION OF DOWNWELLING POLARIZED RADIANCE DISTRIBUTION  
WITH DEPTH IN THE OCEAN

By

Purushottam Bhandari

A DISSERTATION

Submitted to the Faculty  
of the University of Miami  
in partial fulfillment of the requirements for  
the degree of Doctor of Philosophy

Coral Gables, Florida

August 2011

©2011  
Purushottam Bhandari  
All Rights Reserved

UNIVERSITY OF MIAMI

A dissertation submitted in partial fulfillment of  
the requirements for the degree of  
Doctor of Philosophy

THE DESIGN OF A POLARIMETER AND ITS USE FOR THE STUDY OF THE  
VARIATION OF DOWNWELLING POLARIZED RADIANCE DISTRIBUTION  
WITH DEPTH IN THE OCEAN

Purushottam Bhandari

Approved:

\_\_\_\_\_  
Kenneth J. Voss, Ph.D.  
Chairman of Dissertation Committee  
Professor and Chair of Physics Department

\_\_\_\_\_  
Terri A. Scandura, Ph.D.  
Dean of the Graduate School

\_\_\_\_\_  
Howard R. Gordon, Ph.D.  
Professor of Physics

\_\_\_\_\_  
Olga Korotkova, Ph.D.  
Assistant Professor of Physics

\_\_\_\_\_  
Robert Evans, Ph.D.  
Professor of Meteorology and  
Physical Oceanography

BHANDARI, PURUSHOTTAM

(Ph.D., Physics)

(August 2011)

The Design of a Polarimeter and its Use for the Study  
of the Variation of Downwelling Polarized Radiance  
Distribution with Depth in the Ocean.

Abstract of a doctoral dissertation at the University of Miami.

Dissertation supervised by Professor Kenneth J. Voss.

Number of pages in text (104)

The spectral polarized radiance distribution provides the most complete description of the light field that can be measured. However, this is a very difficult parameter to measure near the surface because of its large dynamic range, dependence on incoming sky conditions, and waves at the air-sea interface. The measurement of the Stokes vector of the downwelling polarized light field requires the combination of at least four images, all of which must be obtained simultaneously. To achieve this, a new polarimeter (which we call DPOL) has been designed, characterized, calibrated and deployed. The description of the DPOL, its calibrations and characterizations are discussed. The uncertainties in the retrieval of Stokes vector and other derived parameters are also discussed. This instrument is equipped with four fish-eye lenses (180° field of view) with polarizers behind each lens in a different orientation, a coherent optical fiber bundle with 4 arms, a spectral filter changer assembly and a charged coupled-device (CCD) imaging camera. With this system, a single image contains 4 separate fisheye images, each a whole hemisphere of the same scene, each with different polarization information. Using these 4 images and applying appropriate calibration parameters allows us to calculate the four-element Stokes vector and then the total degree of polarization and the angle of plane of polarization of the incoming light field in a

hemisphere of desired directions. Under the Office of Naval Research RaDyO (Radiance under a Dynamic Ocean) program, DPOL has been used in the Santa Barbara Channel and Hawaii field experiments. In most cases, data on sky polarization were collected with a separate camera (Sky-Cam) simultaneously with the DPOL. The data and results with these two camera systems in these experiments are presented and are compared. Data on the inherent optical properties of water from the same field experiments collected by collaborators will be shown. Our measurements show that very near the surface, for clear sky conditions, the dominant source of polarization is the refracted sky light. As one progresses in the water column, the polarization due to light scattering by the water increases and polarization due to the water becomes dominant. The dependence of the in-water light field polarization on the sky and surface wave conditions, solar zenith and azimuth angles, the depth of the instrument, the viewing angle, the wavelength of light, the inherent optical properties (IOP's) of water are discussed.

## ACKNOWLEDGEMENTS

I heartily thank my supervisor, Professor Kenneth J. Voss, whose encouragement, guidance and support from the initial to the final level has enabled me to develop an understanding of the subject and complete my Ph. D. I would also like to thank him for providing me with great opportunities to take part in field experiments and to attend many conferences and meetings. I would like to thank Professor Howard R. Gordon for his support and the impartment of his experience and knowledge either personally or through seminars. I want to express my gratitude to Assistant Professor Olga Korotkova for her support and continuous effort to conduct uncountable optics seminars. My gratitude also extends to all the other members of my dissertation committee for their time and valuable advice. Special thanks also go to Mr. Luke Logan, who was with me during all the field measurements and without whom the experiments would have been almost impossible. Bill DeReutyer, Juan Lopez and Paul Kleindienst also contributed in building the DPOL instrument. A very special “Thanks” also goes to Mr. Marco Monti for sharing his tremendous knowledge of computers and for his readiness to help. I want to thank all the professors, staff and students in the Department of Physics for making this department a suitable academic environment.

I must thank my parents, Ishwar and Sushma, and relatives for their unconditional support and inspiration. I would like to thank my loving wife Prativa for giving birth to and taking care of my daughter, Puspa, and son, Prabhakar, who fill my heart with joy.

Last but not least, I gratefully acknowledge that my research assistantship and work were supported by the ONR (Office of Naval Research).

## TABLE OF CONTENTS

<b>1. INTRODUCTION .....</b>	<b>1</b>
<b>2. THEORETICAL BACKGROUND .....</b>	<b>5</b>
2.1 Polarized light and Polarization Ellipse .....	5
2.2 Stokes Parameters and Polarization Ellipse .....	7
2.3 Frame of Reference System .....	9
2.4 Degenerate Forms of Polarization Ellipse .....	11
2.5 Optical Devices, Muller Matrix and Stoke's Parameters .....	12
2.6 Mueller Matrix Representation of a Polarimeter .....	13
2.7 Basic Physical Concepts .....	15
2.7.1 Solid Angle .....	15
2.7.2 Radiance and Irradiance .....	16
2.7.3 Inherent Optical Properties of Seawater .....	17
2.7.4 Aerosol and Aerosol Optical Depth .....	19
<b>3. DOWNWELLING POLARIZED CAMERA (DPOL) .....</b>	<b>20</b>
3.1 Overview .....	20
3.2 DPOL Description .....	23
<b>4. DPOL CHARACTERIZATIONS AND CALIBRATIONS .....</b>	<b>31</b>
4.1 Linearity Calibration .....	32
4.2 Spectral Characterization .....	33
4.3 Flatfield Calibration .....	34
4.4 Angular Calibration, Geometrical Projection .....	36
4.5 Rolloff Calibration .....	38
4.6 Polarization Calibration .....	40
4.6.1 Transmission Axis Angle .....	43
4.6.2 Fast Axis Angle and Retardation Angle .....	44

4.6.3	Polarization Calibration of DPOL .....	46
4.7	Absolute Calibration .....	50
4.8	Immersion Calibration .....	53
4.9	Tilt-Roll Calibration .....	56
4.10	Pressure Transducer Calibration .....	58
4.11	Uncertainty in Stokes Vector Retrievals .....	59
<b>5.</b>	<b>FIELD EXPERIMENTS AND DATA REDUCTION OVERVIEW .....</b>	<b>61</b>
5.1	Field Experiments .....	61
5.2	Data Description .....	63
5.3	IOP's and AOD Data .....	65
<b>6.</b>	<b>DATA AND RESULTS .....</b>	<b>68</b>
6.1	SBC Experiment .....	68
6.2	Hawaii Experiment .....	81
<b>7.</b>	<b>CLOUDLIGHT AND ELLIPTICAL POLARIZATION .....</b>	<b>91</b>
7.1	Cloudlight Polarization .....	91
7.2	Elliptical Polarization (EP) .....	95
<b>8.</b>	<b>CONCLUSION .....</b>	<b>97</b>
<b>9.</b>	<b>REFERENCES .....</b>	<b>100</b>

## CHAPTER 1. INTRODUCTION

Polarization is one of the fundamental properties of a light field. Its study can lead us to a deeper understanding of the nature of light itself. The existence of polarization of light in nature confirms the fact that light is a transverse wave. Polarization of an electromagnetic wave determines the direction and magnitude of the vibrating electric field. In an unpolarized light field the vibrations of the electric vectors take place in random directions about the axis of propagation. In linearly polarized light waves the vibrations are confined to a single plane, containing the direction of propagation and the vibration direction. In circularly polarized waves the electric vector rotates about the propagation direction, either in a clockwise or counterclockwise fashion. Light may be polarized by reflection, scattering or by passing through a polarization filter. While sunlight is unpolarized before entering the earth's atmosphere, it becomes partially polarized due to scattering by atmospheric constituents (gases, aerosols, water droplets, ice crystals). The analysis of light polarization has useful applications in crystallography, liquid-crystal displays, optical filters, and identification of optically active compounds. Furthermore, the knowledge of the polarization of the light in both air and water can facilitate studies about behavior of many terrestrial and aquatic animals such as honeybees, butterflies and moths, ants, octopuses, squids, fishes etc., which are found to be sensitive to it.

The investigation of polarization of light began in 1669 by Erasmus Bartholinus (1625-1698) when he discovered the phenomenon of double refraction in calcite crystals

(Goldstein, 2003). The first account of polarization of skylight is given in 1808 by Malus (1775-1812) who observed the reflection of sunlight from a windowpane through a calcite crystal. He found that two images obtained by double refraction would extinguish alternately as he rotated the crystal. Arago (1786-1853) was the first to discover polarization in skylight in 1809 (Horvath and Varju, 2004). The quantitative study of polarization began in 1812 when Brewster derived a relation between the refractive index and an angle at which the reflected field is completely polarized, now known as Brewster angle. In the early 1800s, scientists were still convinced that the Newton's corpuscular theory of light was correct. Huygens was the first to suggest that a light field was a vector field. In 1804 Thomas Young presented results of his famous double slits interference experiment which illustrated the wave nature of light (Young, 1804). Around 1818, Fresnel and Arago performed the Young's double slit experiment with polarized light. From this experiment they discovered that light wave exhibited a transverse nature i.e., it has two mutually perpendicular transverse components that are perpendicular to the direction of propagation. Stokes in 1852 discovered that the light polarization could be characterized in terms of the observable quantities (called the Stoke's parameters), which was a breakthrough for the qualitative and quantitative study of polarization. The studies of the skylight polarization by many theoretical and experimental investigators (Chandrasekhar, 1950; Van de Hulst, 1981; Sekera, 1957; Coulson, 1988; Kattawar and Adams, 1989) have helped us understand the effect of atmospheric turbidity (dust, haze, pollution), surface properties and behavior of many polarization sensitive animals. However, in seawater, the systematic measurement of light polarization was only started around 1954 (Waterman, 1954). A light field propagating in water is generally partially

linearly polarized except for a small amount of elliptical polarization near the water surface and just beyond the critical angle (Ivanoff and Waterman, 1958). At shallow depths, surface waves are the main cause of the variation in the underwater light field (Synder and Dera, 1970) where (within a few meters) the polarization behavior is influenced by the skylight within the Snell's cone (Waterman, 1954). The polarization outside the Snell's cone arises mainly from scattering and internal reflection at the water surface (Ivanoff, 1974). Horvath and Varju (1995) calculated the underwater polarization pattern within the Snell's cone with the celestial polarization pattern including the distortion of the polarization within Snell's window by ripples and surface waves. As one goes deeper into the water column, the effect of skylight decreases relative to scattered sunlight thereby decreasing the degree of polarization (*DoP*) (Ivanoff, 1974). With increasing depth, it has also been found that the peak of the radiance distribution shifts towards the zenith from the refracted position of the sun (Jerlov and Fukuda, 1960; Tyler, 1960). Previous measurements have found that the maximum *DoP* occurs in directions  $60^\circ$  to  $90^\circ$  to that of the solar beam (Waterman, 1954, 1955; Ivanoff, 1974).

To measure the downwelling polarization in the open ocean in the near surface, and following recent work (Voss and Liu, 1997; Voss and Soudia, 2010), we have developed the Downwelling Polarization Radiance Distribution instrument, DPOL (Bhandari et al., 2010). Briefly, this instrument consists of four fisheye camera lenses with a polarizer behind each lens. Behind each polarizer is a coherent fiber bundle. These four bundles are brought together and imaged onto a CCD camera (Apogee Alta E2000) through a filter changer consisting of seven spectral filters with wavelengths ranging from 410 nm to 650 nm. Thus, in a single image we obtain four separate fisheye images

of the same scene, each with different polarization information. After performing the various calibration and characterization steps of the DPOL, we can calculate the four Stokes parameters ( $I$ ,  $Q$ ,  $U$  and  $V$ ) from each CCD image and then calculate the  $DoP$  and the angle of plane of polarization ( $PoP$  denoted by  $\chi$ ). This instrument can be used for the measurement of the upwelling radiance distribution as well. In this dissertation, I will give a detailed description of the DPOL along with its calibration/characterization procedures, and its uncertainties in the measurements.

We participated in two field experiments under the Office of Naval Research RaDyO (Radiance under a Dynamic Ocean) program in Santa Barbara Channel (SBC) on September 9-23, 2008 and in Hawaii on September 1-12, 2009. I will present data collected from the R/P Flip from these experiments. Along with DPOL we collected data on the downwelling polarized sky radiance distribution using the Sky-Cam system, similar to that in Voss and Liu (1997). In most cases we collected simultaneous sky and in-water data using the two camera systems (DPOL and Sky-Cam). In this dissertation, I will present and compare the four Stokes parameters, the  $DoP$  and the  $\chi$  for DPOL and Sky-Cam systems. I will also present the inherent optical properties (IOP's) of water collected by collaborators on this project. I will discuss and show the dependence of polarization on sky and water surface waves, position of sun, instrument depth, viewing direction, wavelength of light and the inherent optical properties of water. Finally, I will discuss the effect of clouds on the polarization of a light field and, in particular on the circular/elliptical polarization in the water from our measurements.

## CHAPTER 2. THEORETICAL BACKGROUND

### 2.1. Polarized light and Polarization Ellipse

The propagation of a monochromatic electromagnetic field ( $\mathbf{E}$ ) along  $z$ -direction at any instant of time  $t$  can be represented by the following equation:

$$\nabla^2 \mathbf{E}(z, t) = \frac{1}{v^2} \frac{\partial^2 \mathbf{E}(z, t)}{\partial t^2} \quad (2.1)$$

Here,  $v$  is the speed of propagation.

The solution of Eq. (2.1) for a transverse wave is given by,

$$\mathbf{E}(z, t) = E_l(z, t)\mathbf{l} + E_r(z, t)\mathbf{r} \quad (2.2a)$$

where the transverse components are represented as,

$$E_l(z, t) = a_l \cos(\omega t - kz + \delta_l) \quad (2.2b)$$

$$E_r(z, t) = a_r \cos(\omega t - kz + \delta_r) \quad (2.2c)$$

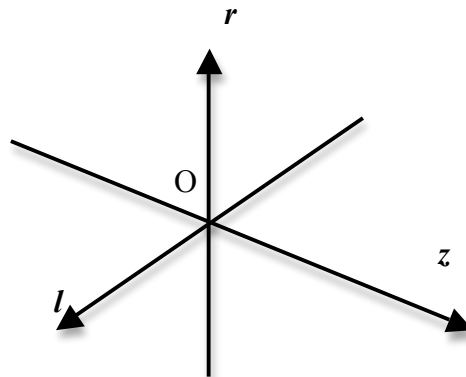


Fig. 2.1 Propagation of electromagnetic wave.

The components  $E_l$  and  $E_r$  represent the magnitude and phase of the electric field vectors parallel ( $l$ ) and perpendicular ( $r$ ) to a reference plane such that  $z = r \times l$  (Fig. 2.1). The reference plane is a plane containing the direction of propagation and another convenient direction. Here,  $\omega = \frac{2\pi}{T} = k\nu$  is the angular frequency,  $k = \frac{2\pi}{\lambda}$  is the wave number, and  $T$  is the time period of oscillation.  $a_l$  and  $a_r$  represents the amplitudes, and  $\delta_r$  and  $\delta_l$  are arbitrary phase constants whose signs can be positive or negative. If we eliminate the propagator,  $\tau = \omega t - kz$ , between Eqs. (2.2b) and (2.2c) and with some simplification, we can arrive at the following equation:

$$\frac{E_l^2}{a_l^2} + \frac{E_r^2}{a_r^2} - 2\frac{E_l E_r}{a_l a_r} \cos \delta = \sin^2 \delta, \quad (2.3a)$$

$$\text{with } \delta = \delta_r - \delta_l \quad (2.3b)$$

Equation (2.3a) is the equation of an ellipse. This shows that as the electromagnetic wave propagates in space, at any instant of time, the locus of points described by the tip of the electric field is an ellipse. This behavior describes the optical polarization.

The ellipse can be inscribed within a rectangle as shown in Fig. 2.2. The sides of the rectangle have lengths  $2 a_l$  and  $2 a_r$  and are parallel to the x- and y-axes. The ellipse is tangent to the sides of the rectangle at  $(\pm a_r, \pm a_r \cos \delta)$  and  $(\pm a_l \cos \delta, \pm a_r)$ . The third term on the left hand side of Eq. (2.3a) represents the rotation of the ellipse (see Fig. 2.2).

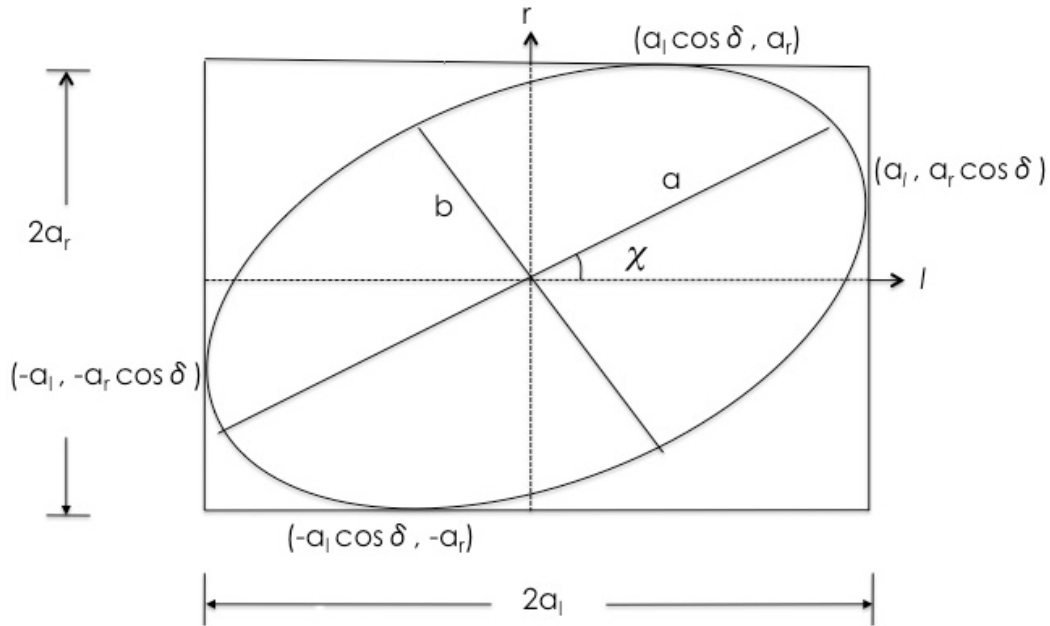


Fig. 2.2 Polarization ellipse.

## 2.2. Stokes Parameters and Polarization Ellipse

The polarization ellipse is very important because it enables us to describe the various states of fully polarized light. When light propagates in space, the tracing of the ellipse, or some special form of it such as a circle or a straight line, takes place in a time interval of about  $10^{-15}$  sec. This time interval is too short for most measurement purposes. In addition, the total light field can contain unpolarized and random components, therefore we require a representation of the light field in terms of observables such as the time average of the optical fields.

Sir George Gabriel Stokes (1819-1903), in 1852, first described the different states of polarization of light in terms of measurable quantities, called the Stokes parameters (Stokes, 1852). These parameters are denoted by  $I$ ,  $Q$ ,  $U$  and  $V$  or  $S_0$ ,  $S_1$ ,  $S_2$

and  $S_3$ . The first parameter ( $I$ ) is a measure of the total intensity of light. The second parameter ( $Q$ ) is a measure of the intensity of linear horizontally or vertically polarized light. The third parameter ( $U$ ) is a measure of the intensity of light linearly polarized at  $\pm 45^\circ$  to the horizontal plane. The fourth parameter ( $V$ ) is a measure of the intensity of left or right circular polarization. From these four parameters we can derive other important parameters such as  $DoP$ , orientation angle ( $\chi$ ) of the  $PoP$ , and the ellipticity angle ( $\beta$ ) of the ellipse.

For monochromatic fields, we can define the Stokes parameters in terms of complex amplitudes or the components of intensity of the wave as (Coulson, 1988; Van de Hulst, 1981; Goldstein, 2003):

$$I = \langle a_l^2 \rangle + \langle a_r^2 \rangle = \langle E_l E_l^* \rangle + \langle E_r E_r^* \rangle = I_l + I_r \quad (2.4a)$$

$$Q = \langle a_l^2 \rangle - \langle a_r^2 \rangle = \langle E_l E_l^* \rangle - \langle E_r E_r^* \rangle = I_l - I_r \quad (2.4b)$$

$$U = \langle 2a_l a_r \cos \delta \rangle = \langle E_l E_r^* \rangle + \langle E_r E_l^* \rangle = I_{45} - I_{-45} \quad (2.4c)$$

$$V = \langle 2a_l a_r \sin \delta \rangle = i(\langle E_l E_r^* \rangle - \langle E_r E_l^* \rangle) = I_{RCP} - I_{LCP} \quad (2.4d)$$

The operator  $\langle \rangle$  represents the time average for a time interval  $(t_1, t_2)$ .

Using Eqs. (2.4a to 2.4d), it can easily be shown that

$$I^2 \geq Q^2 + U^2 + V^2, \quad (2.5)$$

where the equality holds for fully polarized light. In all other cases the light is said to be partially polarized except when  $Q=U=V=0$ , which is the case of unpolarized light. The

$DoP$ ,  $\chi$ , and  $\beta$  can be expressed in terms of the Stokes parameters by the following equations:

$$DoP = \frac{(Q^2 + U^2 + V^2)^{1/2}}{I}, \quad 0 \leq DoP \leq 1, \quad (2.6)$$

$$\tan 2\chi = \frac{U}{Q}, \quad -90^\circ \leq \chi \leq 90^\circ, \quad (2.7)$$

$$\sin 2\beta = \frac{2a_l a_r \sin \delta}{a_l^2 + a_r^2} = \frac{V}{(Q^2 + U^2 + V^2)^{1/2}}. \quad (2.8)$$

The degree of linear polarization ( $DoLP$ ) is calculated by setting  $V = 0$  in Eq. (2.6).

### 2.3. Frame of Reference System

As a rule, one should transform the Stokes parameters measured in the instrument frame into a more common frame such as the sky frame (Liu, 1996; Kattawar and Adams, 1989). In the sky frame (Fig. 2.3), we consider the light propagating along  $z = \mathbf{r} \times \mathbf{l}$  direction and  $\chi$  is measured from  $\mathbf{l}$  to  $\mathbf{r}$  such that  $\mathbf{r}$  and  $\mathbf{l}$  are perpendicular and parallel to the meridian plane (containing the view and zenith direction) respectively. The transformation of the Stokes parameters from instrument frame  $(\mathbf{l}, \mathbf{r})$  to sky frame  $(\mathbf{l}', \mathbf{r}')$  is a rotation of the  $(\mathbf{l}, \mathbf{r})$  axes by an angle  $\gamma$  (Fig. 2.4).  $I$  and  $V$  are invariant under such a rotation as they are independent of  $\chi$ . Thus the Stokes parameters in the new frame are given by (Coulson, 1988; Kattawar and Adams, 1989):

$$\begin{aligned}
 I' &= I \\
 Q' &= Q \cos 2\gamma + U \sin 2\gamma \\
 U' &= -Q \sin 2\gamma + U \cos 2\gamma \\
 V' &= V
 \end{aligned}
 \tag{2.9}$$

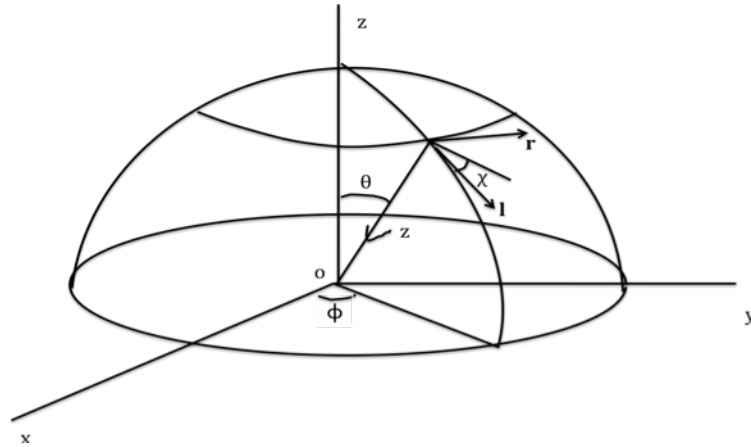


Fig. 2.3 Illustration of the coordinate system in the sky frame.

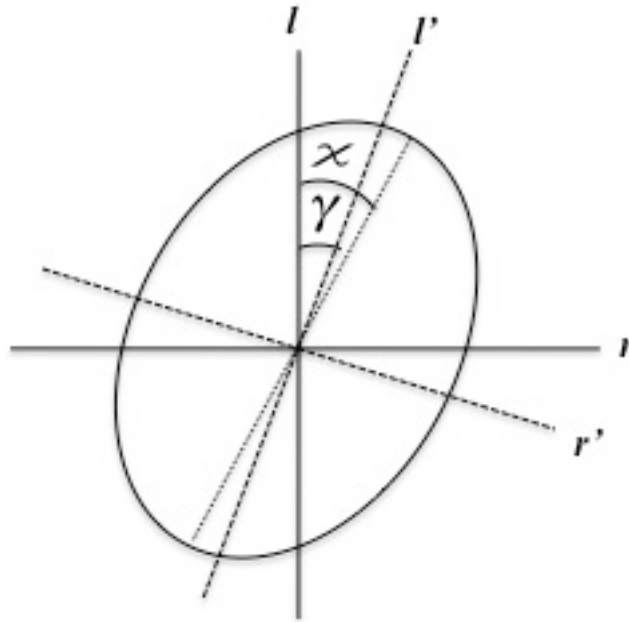


Fig. 2.4 Diagram showing a rotation of axes from instrument frame ( $l, r$ ) to sky frame ( $l', r'$ ) by an angle  $\gamma$ .

## 2.4. Degenerate Forms of Polarization Ellipse

Elliptical polarization is the most general case of polarization. There are many states of polarization which depend on the values of the amplitudes ( $a_l$  and  $a_r$ ) and phase difference ( $\delta = \delta_r - \delta_l$ ) between orthogonal transverse components. When  $a_r = 0$ , the oscillation is only along  $l$  direction and the light is said to be linearly horizontally polarized (LHP). When  $a_l = 0$ , the oscillation is only along  $r$  direction and the light is said to be linearly vertically polarized (LVP).

For  $\delta = 0$  or  $\pi$ , Eq. (2.3a) can be written as

$$E_r = \pm \left( \frac{a_r}{a_l} \right) E_l \quad (2.10)$$

For  $a_l = a_r$  and  $\delta = 0$ , it is seen that the oscillation is in a plane  $45^\circ$  to  $l$  and the light is said to be L +45. For  $a_l = a_r$  and  $\delta = \pi$ , the oscillation is in a plane  $-45^\circ$  to  $l$  and the light is said to be L -45.

The polarization is right-handed (or left-handed) if the tip of the electric vector rotates clockwise (or counterclockwise) as seen by an observer looking into the direction from which the light is coming. In this case, if  $a_l = a_r$  and  $\delta = \pi/2$  or  $3\pi/2$ , Eq. (2.3a) becomes the equation of a circle and the light is said to be right circularly polarized (RCP, for  $\delta = \pi/2$ ) or left circularly polarized (LCP, for  $\delta = 3\pi/2$ ).

These degenerate forms of polarization are summarized in table 2.1.

Table 2.1 Degenerate forms of polarization.

	LHP	LVP	L +45	L -45	RCP	LCP
amplitude	$a_r = 0$	$a_l = 0$	$a_l = a_r = a$	$a_l = a_r = a$	$a_l = a_r = a$	$a_l = a_r = a$
intensity	$I_0 = a_l^2$	$I_0 = a_r^2$	$I_0 = 2a^2$	$I_0 = 2a^2$	$I_0 = 2a^2$	$I_0 = 2a^2$
phase			$\delta = 0^\circ$	$\delta = 180^\circ$	$\delta = 90^\circ$	$\delta = -90^\circ$
Stokes vector	$S = I_0 \begin{pmatrix} 1 \\ 1 \\ 0 \\ 0 \end{pmatrix}$	$S = I_0 \begin{pmatrix} 1 \\ -1 \\ 0 \\ 0 \end{pmatrix}$	$S = I_0 \begin{pmatrix} 1 \\ 0 \\ 1 \\ 0 \end{pmatrix}$	$S = I_0 \begin{pmatrix} 1 \\ 0 \\ -1 \\ 0 \end{pmatrix}$	$S = I_0 \begin{pmatrix} 1 \\ 0 \\ 0 \\ 1 \end{pmatrix}$	$S = I_0 \begin{pmatrix} 1 \\ 0 \\ 0 \\ -1 \end{pmatrix}$

## 2.5. Optical Devices, Mueller Matrix and Stokes Parameters

To design a polarimeter, one must know the action of optical devices such as polarizer, retarder, rotator, and depolarizer used in the instrument. These optical devices change the polarization states of the light field, so one must have a way to describe these changes in terms of the Stokes vector. The Stokes parameters of the transmitted beam can be related to the Stokes parameters of the incident beam in terms of a 4 x 4 real matrix, called the Mueller matrix. The Mueller matrix, which was first introduced by Hans Mueller in 1943, describes how the Stokes vectors of the incident light are transformed by the device.

Suppose we have an instrument (polarimeter) which consists of ‘ $n$ ’ number of optical devices such that the first device encountered by the incident beam has its Mueller

matrix  $M_1$ , the second has  $M_2$  and the  $n^{\text{th}}$  has  $M_n$ . Then the emerging Stokes vector,  $S'$ , in terms of incident Stokes vector,  $S$ , is given by the product,

$$S' = M_n \dots M_3 \cdot M_2 \cdot M_1 \cdot S \quad (2.11)$$

For a single optical device its Mueller matrix is related to the Stokes vector of the incident light,  $S$ , and transmitted light,  $S'$ , by:

$$\begin{pmatrix} I' \\ Q' \\ U' \\ V' \end{pmatrix} = \begin{pmatrix} M_{11} & M_{12} & M_{13} & M_{14} \\ M_{21} & M_{22} & M_{23} & M_{24} \\ M_{31} & M_{32} & M_{33} & M_{34} \\ M_{41} & M_{42} & M_{43} & M_{44} \end{pmatrix} \begin{pmatrix} I \\ Q \\ U \\ V \end{pmatrix} \quad (2.12a)$$

or

$$S' = M S \quad (2.12b)$$

## 2.6. Mueller Matrix Representation of a Polarimeter

In the DPOL system, we record only the total intensity of the light field emerging from many optical components such as the fisheye lens, linear or circular polarizer, coherent optical fiber bundle and assembly of collimating lenses. To measure the Stokes parameters of a scene, it is easier to consider the whole system as one unit and relate the emerging intensities ( $I_i$ ,  $i = 1, 2, 3, 4$ ) for each image or lens/polarizer system, with the Stokes parameters of the incident light field in terms of a transformation matrix  $T$  using the following equation.

$$\begin{pmatrix} I \\ Q \\ U \\ V \end{pmatrix} = \begin{pmatrix} \mathcal{I}_{11} & \mathcal{I}_{12} & \mathcal{I}_{13} & \mathcal{I}_{14} \\ \mathcal{I}_{21} & \mathcal{I}_{22} & \mathcal{I}_{23} & \mathcal{I}_{24} \\ \mathcal{I}_{31} & \mathcal{I}_{32} & \mathcal{I}_{33} & \mathcal{I}_{34} \\ \mathcal{I}_{41} & \mathcal{I}_{42} & \mathcal{I}_{43} & \mathcal{I}_{44} \end{pmatrix} \begin{pmatrix} I_1 \\ I_2 \\ I_3 \\ I_4 \end{pmatrix} \quad (2.13a)$$

or

$$S = \mathcal{T} I \quad (2.13b)$$

Here, in our case with DPOL system, the  $I$ 's can be treated as the camera counts as recorded by each fisheye lens.

Equations (2.12b) and (2.13b) can also be written as:

$$S = M^{-1} S' \quad (2.13c)$$

$$I = T^{-1} S', \quad (2.13d)$$

where  $M^{-1}$  and  $T^{-1}$  are the inverse of the matrices  $M$  and  $T$  respectively.

From Eq. 2.12a, since,

$$I_1 = M_{11}^1 I + M_{12}^1 Q + M_{13}^1 U + M_{14}^1 V \quad (2.14a)$$

$$I_2 = M_{11}^2 I + M_{12}^2 Q + M_{13}^2 U + M_{14}^2 V \quad (2.14b)$$

$$I_3 = M_{11}^3 I + M_{12}^3 Q + M_{13}^3 U + M_{14}^3 V \quad (2.14c)$$

$$I_4 = M_{11}^4 I + M_{12}^4 Q + M_{13}^4 U + M_{14}^4 V \quad (2.14d)$$

then

$$I = M' S, \quad (2.14e)$$

or

$$S = [M']^{-1} I \quad (2.14f)$$

where  $M'$  is formed by combining the first row of the Mueller matrix for each lens/polarizer system. Therefore, comparing Eqs. (2.13b) and (2.14f), we find that

$$T = [M']^{-1}. \quad (2.14g)$$

Thus we could determine the combined  $M$  of each lens/polarizer system, from  $M'$ , then calculate the inverse to get  $T$ . In the end it is easier, and more accurate, to determine  $T$  directly through calibration rather than  $M'$  and then  $[M']^{-1}$ . Chapter 4 will detail the determination of the  $T$ -matrix.

## 2.7. Basic Physical Concepts

### 2.7.1. Solid Angle

Solid angle (denoted by  $\Omega$ ) is a conical angle in three dimensional space that an object subtends at a point. It is a measure of how large that object appears to an observer looking from that point and its unit is steradians (sr). It is shown in Fig. 2.5, and mathematically, it is expressed as

$$\Omega = \iint \frac{\hat{n} \cdot d\vec{A}}{r^2} \quad (2.15)$$

In spherical coordinate, it is given by the following equation.

$$\Omega = \iint_{\theta \phi} \sin \phi \, d\theta \, d\phi \quad (2.16)$$

Therefore, the solid angle of a whole sphere is  $4\pi$  steradians.

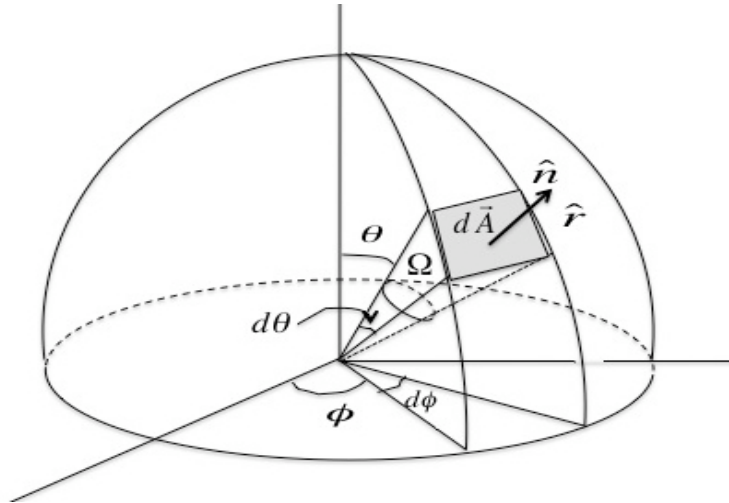


Fig. 2.5 Illustration of a solid angle representation in polar coordinates.

### 2.7.2. Radiance and Irradiance

The most important quantities that can be measured in radiometry are radiance and irradiance. Consider that a differential amount of radiant power  $d^2 P_\lambda$  at wavelength  $\lambda$  within a wavelength interval  $d\lambda$  crosses an element of area  $d\vec{A}$ , which has a differential solid angle  $d\Omega$ , in a direction making an angle  $\theta$  to the normal of  $d\vec{A}$  (Fig. 2.5). This power can be related to the radiance  $L_\lambda$  by

$$d^2 P_\lambda(\theta, \phi) = L_\lambda(\theta, \phi) \cos \theta \, dA \, d\Omega \, d\lambda, \quad (2.17)$$

or,

$$L_{\lambda}(\theta, \phi) = \frac{d^2 P_{\lambda}(\theta, \phi)}{\cos \theta dA d\Omega d\lambda}. \quad (2.18)$$

Therefore, the radiance can be defined as the amount of radiant power per unit wavelength crossing a unit area within a unit solid angle (Boyd, 1983). Its SI unit is  $W m^{-2} nm^{-1} sr^{-1}$ . Chapter 6 will detail the measurement of radiance.

The spectral irradiance (SI unit:  $W m^{-2} nm^{-1}$ ) of radiant energy to a surface is defined by the normal component of  $L_{\lambda}$  integrated over a solid angle  $\Omega$  subtended by the surface and can be written as

$$E_{\lambda}(\theta, \phi) = \int_{\theta} \int_{\phi} L_{\lambda}(\theta, \phi) \cos \theta \sin \theta d\theta d\phi. \quad (2.19)$$

### 2.7.3. Inherent Optical Properties of Seawater

In general, the optical properties of seawater are described in terms of inherent and apparent properties. The inherent optical properties (IOPs) of water depend only on the medium and therefore are independent of the ambient light field. On the other hand, the apparent optical properties (AOPs) depend both on the medium and on the directional structure of the ambient light field (Mobley, 2000a). In this dissertation I will only use the IOPs data (in Chapter 5). The absorption coefficient  $a_{\lambda}(\lambda)$  and the scattering coefficient  $b_{\lambda}(\lambda)$  are the two fundamental IOPs, usually employed in radiative transfer theory. Below is a brief description of these properties.

Let us consider a small volume  $\Delta V$  and thickness  $\Delta r$  of water illuminated by a collimated beam of monochromatic light of wavelength and spectral radiant power  $\Phi_i(\lambda)$  ( $W\ m^{-2}$ ), as schematically illustrated in Fig. 2.6. Here, some part  $\Phi_a(\lambda)$  is absorbed by the volume  $\Delta V$  of water. Some part  $\Phi_s(\theta, \lambda)$  is scattered out of the beam at an angle  $\theta$ , and the remaining power  $\Phi_t(\lambda)$  is transmitted through this volume without any change in

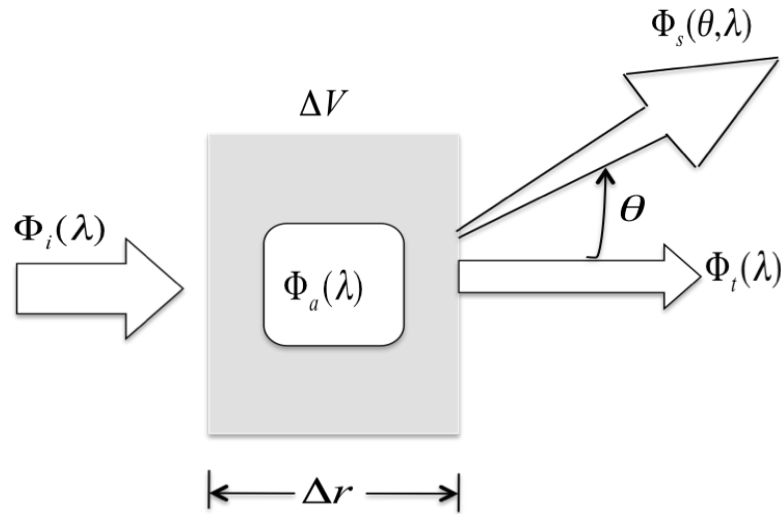


Fig. 2.6 Schematic diagram showing the absorption and scattering of the incident light radiation by a volume of water.

direction. Then  $a_r(\lambda)$ , the absorption coefficient, is defined as the limit of the fraction of  $\Phi_i(\lambda)$  that is absorbed within  $\Delta V$  when  $\Delta r$  becomes small (Mobley, 2000a):

$$a_r(\lambda) = \lim_{\Delta r \rightarrow 0} \frac{1}{\Phi_i(\lambda)} \frac{\Phi_a(\lambda)}{\Delta r} \quad m^{-1}. \quad (2.20)$$

Similarly the scattering coefficient  $b_r(\lambda)$  is defined as the limit of the fraction of  $\Phi_i(\lambda)$  that is scattered out of the beam within  $\Delta V$  when  $\Delta r$  becomes small (Mobley, 2000a):

$$b_r(\lambda) = \lim_{\Delta r \rightarrow 0} \frac{1}{\Phi_r(\lambda)} \frac{\Phi_s(\theta, \lambda)}{\Delta r} \quad m^{-1}, \quad (2.21)$$

Then, the beam attenuation coefficient  $c_r(\lambda)$ , which is a quantity that characterizes the total loss in a beam of light, is given by,

$$c_r(\lambda) = a_r(\lambda) + b_r(\lambda). \quad (2.22)$$

#### 2.7.4. Aerosol and Aerosol Optical Depth

Tiny solid and liquid particles suspended in the atmosphere are called aerosols. Their size ranges from several nanometers to hundreds of microns (Shettle and Fenn, 1979). Windblown dust, pollution from factories, smoke, sea salts, volcanic ash, haze, fog, and clouds are some examples of aerosols.

The attenuation of solar beam intensity  $I$  in the atmosphere is given by the equation (Kokhanovsky, 2008)

$$I = I_0 \exp(-\tau / \cos \vartheta_0), \quad (2.23)$$

where  $\tau$  is called the aerosol optical depth (AOD),  $I_0$  is the intensity at the top of the atmosphere, and  $\vartheta_0$  is the solar zenith angle. From Eq. 2.23,  $\tau$  can be expressed in the form

$$\tau = \cos \vartheta_0 \ln(I_0 / I). \quad (2.24)$$

Eq. 2.24 implies that  $\tau$  is a dimensionless quantity. In Chapter 5, I will present a Table showing the AOD values from field measurements.

## CHAPTER 3. DOWNWELLING POLARIZED CAMERA (DPOL)

### 3.1. Overview

An instrument used to measure the polarization of the light field is called a polarimeter. The first polarimeter was designed by Arago in 1811 for the observation of extraterrestrial polarization (Dougherty and Dollfus, 1989). Early measurements of radiance and polarization of sky and water were performed with collimated polarimeters as used by Waterman (1954), Ivanoff and Waterman (1958), Sekera (1957), Timofeeva (1962), Shaw (1975), Brian & Gould (1982), Aas and Hojerslev (1999), and others. These polarimeters had a very narrow (1-6 degree) field of view. Therefore, to measure the hemispherical radiance distribution one needed a large number of individual measurements pointing into different directions. This requires a considerable period of time, and during this time the celestial polarization pattern can change, at a minimum with changes in the sun angle. To shorten the measurement time, scientists were interested in developing wide-field-of-view imaging polarimeters. Walraven (1981), Egan (1986), Wolff (1994), Cronin et al. (1994), Shashar et al. (1995), for example, designed polarimeters with fields of view of up to 45°. North and Duggin (1997) designed a polarimeter to obtain 3 components of the Stokes vector of the polarized sky-dome by suspending a 4-lens stereoscopic camera directly above a dome mirror. Voss and Liu (1997), Gal et al. (2001) and Horvath et al. (2002) designed polarimeters consisting of fisheye lens systems which could produce 180° field of view images of the

sky-dome. Since circularly polarized radiation almost never exists in the atmosphere (Coulsen, 1988), one needs to record only three images of a scene, in a time interval as short as possible, to determine the radiance and polarization behavior of the sky. To study the sky polarization behavior most polarimeters record three sequential images, for example Gal et al. (2001). These systems can not be used if the sky conditions are changing rapidly. To take into account rapid changes in the optical properties of the sky, Horvath et al. (2002) designed a three-lens, three-camera full sky polarimeter that records the three images of a scene simultaneously. On the other hand, to study the radiance and polarization behavior of the light field in the ocean, where circular polarization has been found in certain conditions (Ivanoff and Waterman, 1958), we require four simultaneous images of the same scene.

Using an electro-optic camera system, including a filter changer and a fisheye lens, the unpolarized spectral upwelling radiance distribution in the ocean has been studied (Voss, 1989b) with the development of RADS (Voss, 1989) and NuRADS (Voss and Chapin, 2005). These systems have been used in various investigations including validation of the angular correction of ocean color algorithms (Voss et al., 2007).

In Wolf and Andreau (1995) and Tyo et al. (2006) techniques for determining the polarization of the light field and different kinds of polarimeters have been reviewed and discussed. The techniques include Division of Amplitude (DOA), Division of Time (DOT), Division of Aperture, Division of focal plane, and co-boresighted. For the computation of a complete Stokes image the DOA type polarimeter consists of four separate cameras. The cameras are mounted such that a single objective lens is used in combination with a series of polarizing beam splitters, retarders, and relay lenses. The

common approach of a DOT type polarimeter is to rotate polarization elements in front of the camera system. In clear sky conditions, DOT is the simplest method and has been used by many, including Voss and Liu (1997). The division of aperture polarimeter subdivides the image into separate images which can be treated individually with polarization elements. The division of focal-plane polarimeter consists of micro-optical elements with different polarization states which are integrated onto the focal plane array. In this type of polarimeter the simultaneity of all the images is guaranteed. In the co-boresighted technique the polarization is measured by using separate cameras and optics that are exactly aligned. In the ocean where the light field is rapidly changing due to the interaction of the incident radiance with surface waves (Schenck, 1957) the DOT technique is not applicable. In this case, the co-boresighted technique allows simultaneous measurement, is more practical, and was used in Polrads (Voss and Souaidia, 2010) and in the three-lens three-camera full sky polarimeter (Horvath et al., 2002). For the study of the downwelling polarized radiance distribution in the ocean and taking into account the rapid changes of the light field, we have designed a co-boresighted polarimeter (DPOL). This instrument can record four simultaneous hemispherical images of the same scene, each with different polarization information. Below, we describe this instrument in detail with its construction, characterization and calibration.

### 3.2. DPOL Description

This new system (DPOL) is designed for measurement of both the downwelling and upwelling polarized radiance distributions of the light field in the ocean. In order to measure all four Stokes parameters on the whole hemisphere, while ensuring the simultaneity of the data, we use four fisheye lenses. Behind three of the lenses are linear polarizers at different orientations, and behind the fourth lens is a circular analyzer. Each fisheye lens is focused on the end of a branch of a coherent fiber optic bundle and the four branches of the bundle are brought together and are arranged to form a 2 x 2 array. The image of this 2 x 2 array is then passed through a spectral filter changer and lens relay system and is finally imaged onto a CCD camera. Thus, in a single image we have four separate fisheye images of the same scene, each with different polarization information. Below is a more detailed description which follows the path of light entering the system.

The first element of the DPOL system is a non-coated hemispherical custom glass window (index of refraction=1.50, manufactured by Outland Technology). These windows have an inner and outer diameters of 7.6 and 8.3 cm respectively. Because the fisheye lens has such a short focal length and small aperture, these windows can be treated as if they were at infinity.

The light then enters a fisheye lens. We have used a Coastal Optics c-mount fisheye lens, with 2.16 mm focal length and f/3.3-f/16 f-number. It has a 185° field of view. We tested the polarization sensitivity of this lens by illuminating the lens with fully polarized light, rotating a polarizer behind the lens and measuring the extinction ratio

( $I_{\text{crossed}} / I_{\text{parallel}}$ ). The extinction ratio was found to be greater than 100:1 for all angles of incidence. After this test, the lens was mounted behind the glass dome in such a way as to make the effective first principal plane of the optical system at the center of curvature of the dome. In this manner the system uses the light which has entered the system perpendicular to the glass window, and thus the system acts the same way in air and in water. By performing an angular calibration of the system in water and in air, to be discussed later, we can test how well the lens is positioned.

Behind each of the three fisheye lenses is a linear polarizer and behind the fourth lens is a circular analyzer. The three linear polarizers are dichroic sheet polarizers (Melles Griot, 03 FPG 019) and are oriented at approximately  $0^\circ$ ,  $60^\circ$  and  $120^\circ$  relative to an arbitrary reference axis. The circular analyzer is a combination of a broadband mica quarter wave plate (Melles Griot, 02 WRM001) and a linear polarizer (Melles Griot, 03 FPG 019). It is placed behind the fourth lens such that the quarter wave plate is adjacent to the fisheye lens. With this combination of linear polarizers and circular analyzer we are able to calculate the 4 Stokes parameters of a scene.

The fisheye lens focuses the light onto the end of a custom coherent fiber optic bundle (Schott North America, Inc.). The fiber bundle has four branches and each branch is 4mm x 4mm. The bundle is made of  $10\ \mu\text{m}$  fibers. There is also a custom fiber optic taper which adjusts the size of the fisheye lens image (8 mm in diameter) to the size of the optical fiber bundle. The other ends of the four bundles are brought together to form a 2 x 2 array of individual fisheye images. The grouped end of the fiber bundle is imaged onto the CCD camera using a lens relay system and a spectral filter wheel.

We have used a spectral filter wheel (Optec IFW), which is placed between two relay lenses. The relay lenses are made up of compact C-mount lenses (Schneider, Xenoplan 2.8/50). The filter wheel has positions for eight 25.4 mm diameter filters. In seven positions we insert interference filters to select the spectral band of interest. The last position is blocked and is used to get a dark image. The filter wheel communicates via an RS-232 interface. The wheel is rotated by a stepper motor, and magnets inserted in the wheel opposite to each filter identify the filter position. It takes about 3 s to change the filter position.

The camera used in this system is an Apogee, Alta E2000. It uses the monochrome Kodak KAI-2020M CCD interline transfer array (1600 x 1200, with 7.4 x 7.4 micron pixels elements). It has a 100baseT Ethernet interface that allows us to control it from a considerable distance using a suitable cable and a laptop computer. This system also has two serial port outputs for control of peripheral devices, a programmable I/O port, an electronic shutter to allow very fast exposure times, and a programmable cooling system to cool to 50°C below ambient temperature. In addition, it has anti-blooming features to reduce the effect of bright features from “blooming” into the rest of the image. Figure 3.1 is a sample image with this system taken inside the optics laboratory.



Fig. 3.1 Sample image from DPOL camera system. There are 4 separate fisheye images shown in this one camera image, the result of our quadfricated fiber bundle. Each small fisheye image carries different polarization information. Three of the images have linear polarizers in line with the image optical path. The remaining image contains a circular polarization analyzer. By combining these images, the 4 Stokes parameters can be determined.

The additional non-optical devices used in the system are a gyro enhanced orientation sensor (3DM-GX1, Micro Strain) to give roll, pitch and yaw. This device communicates via an RS-232 interface. We also employ a pressure transducer (Model TJE, Honeywell) to find the instrument's depth. This device gives an analogue output signal (0-5 VDC), which is directly proportional to the pressure.

The system also includes other electronics such as an Ethernet hub (PRV-1059), a fiber transceiver (NM-102KIT, Netsys), and a microprocessor module (RabbitCore RCM4000). The fiber transceiver and Ethernet hub allows us to either use a fiber link, or a copper link, depending on the distances required. The fiber transceiver includes a

100Base-TX copper to 100Base-FX fiber media converter. Thus, we can use optical fiber to connect to the instrument enabling longer communication distances. In this system only the pressure transducer is connected to the microprocessor module, which distributes the pressure transducer signal and can be queried via Ethernet. We also use a DC-DC converter (Vicor) to convert an input voltage (24-36 VDC) into 12 VDC.

All these devices are arranged inside an aluminum housing. The external dimensions of the box are 48 x 30 x 20 cm<sup>3</sup>. The total mass of the whole system (including all the parts) is 27.3 kg (60 lb). The pressure housing was designed to be used to depths of 100 m in the ocean.

Figures 3.2 and 3.3 show pictures of DPOL after assembly, while Fig. 3.4 shows a block diagram of the electronic components and connections. Figure 3.5 shows the optical layout of DPOL camera system.



Fig. 3.2 Image of the top of the polarization camera system. One can see the four fisheye lenses all aligned in a row. On the left are connectors to allow the system to be used either over a dedicated cable (the big connector) and fiber, or through a copper ethernet connection.



Fig. 3.3 Image of the interior of the polarization camera system. On the far left is the camera (the blue box), in front of which is the IFW filter chamber. The coherent fiber bundle is shown, with each leg going to fisheye lenses in the lower portion of the box. We also have a pressure transducer, tilt and roll indicator, and other associated electronics. The system is controlled by the laptop shown on the left of the picture.

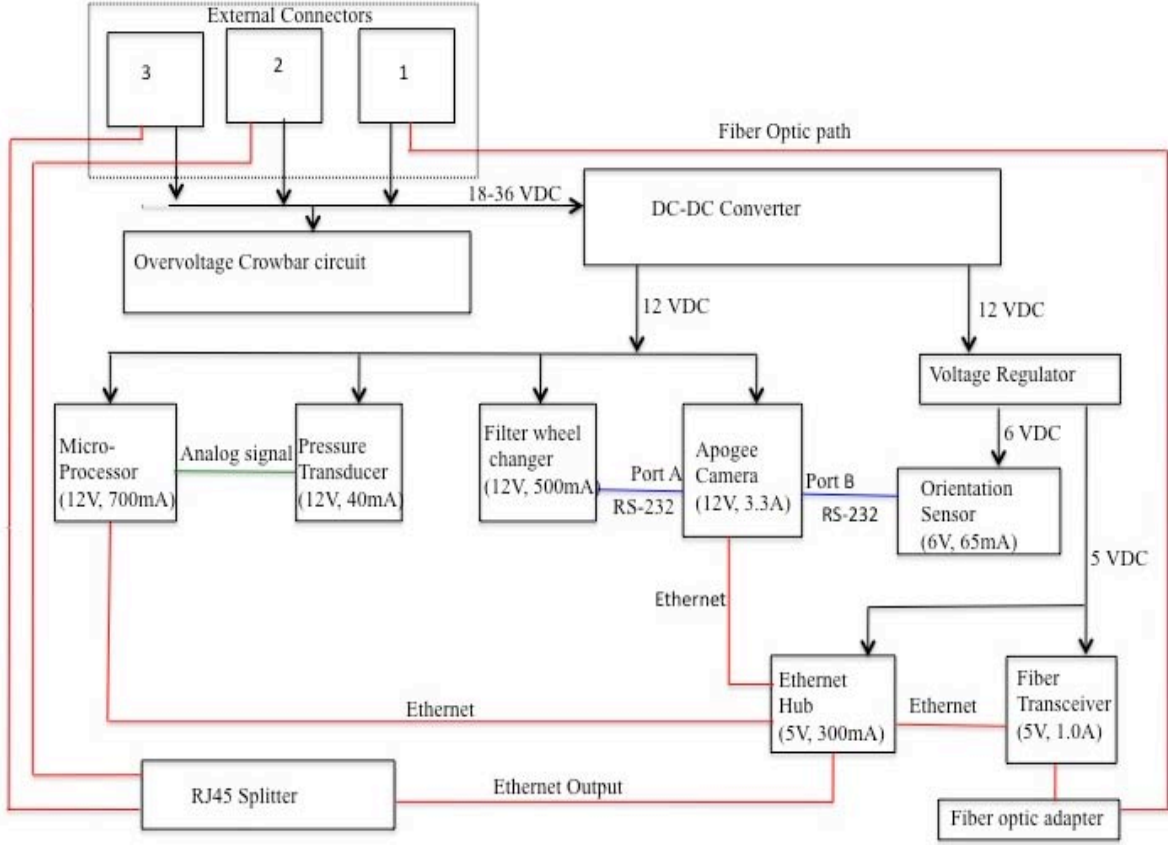


Fig. 3.4 Block diagram of the electronic parts used in the DPOL system. The black lines with arrows are used to denote the path of the power to the devices, the red lines represent the connection via Ethernet cable (RJ45), the green line represents the connection used for analog signals, and the blue lines represent the serial port communication via the RS-232.

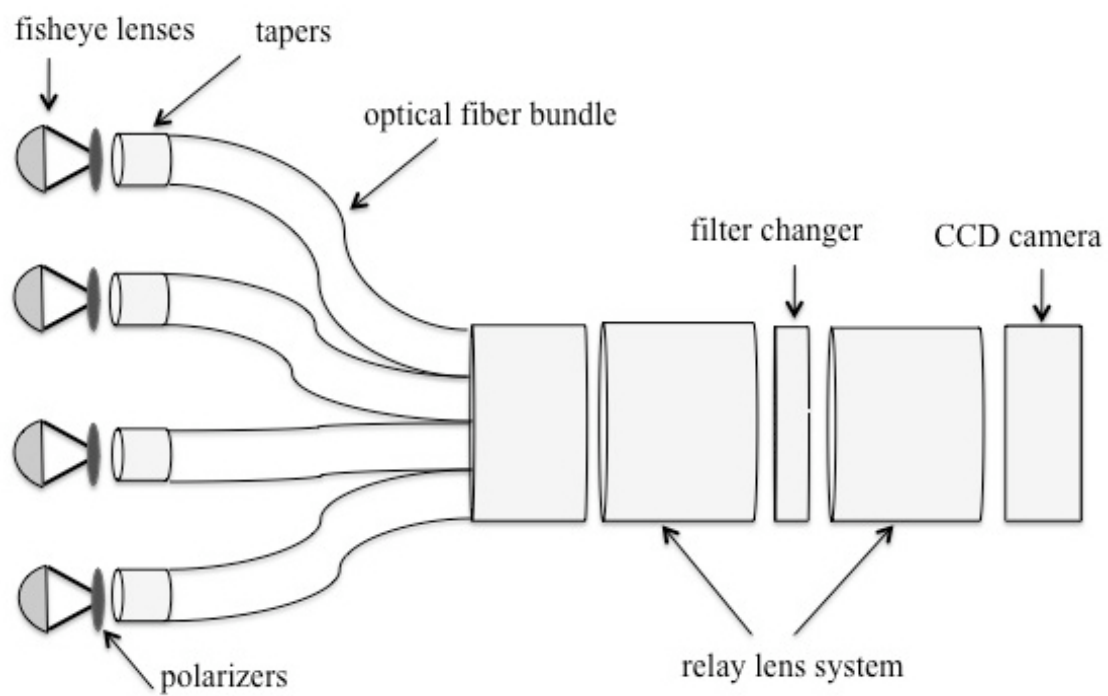


Fig. 3.5 Optical layout of DPOL camera system.

## CHAPTER 4. DPOL CHARACTERIZATIONS AND CALIBRATIONS

The objective of the DPOL calibration is to qualitatively and quantitatively characterize the instrument to obtain a relationship between the incident polarized radiance and the instrument output. The validity of the results obtained with the instrument totally depends on the ability to characterize the instrument and on the accuracy of each calibration step performed. To obtain the radiance distribution in S.I. units with polarization information we have performed the following calibrations and characterizations of the DPOL system, most of which follow in the footsteps of the non-polarized fisheye systems RADS and NuRADS (Voss and Zibordi, 1989; Voss and Liu, 1997; Voss and Chapin, 2005).

1. Linearity Characterization
2. Spectral Characterization
3. Flatfield Calibration
4. Angular or Geometric Calibration (Water and Air)
5. Rolloff Calibration
6. Polarization Calibration (Linear and Circular)
7. Absolute or Radiometric Calibration
8. Immersion Calibration
9. Orientation Sensor Calibration
10. Pressure Sensor Calibration

Each characterization and calibration is discussed in detail below.

#### 4.1. Linearity Calibration

In this calibration I placed the camera at a fixed distance from a uniform source of light and take images with exposure times from 1.0 s to 0.0001 s. For each image I also recorded a corresponding dark image. The camera counts versus the exposure time (or the shutter speed) were analyzed. I found that the counts are linear from 1.0 s to 7 ms exposure time. Below 7 ms the linearity began to break down as shown in Fig. 4.1.

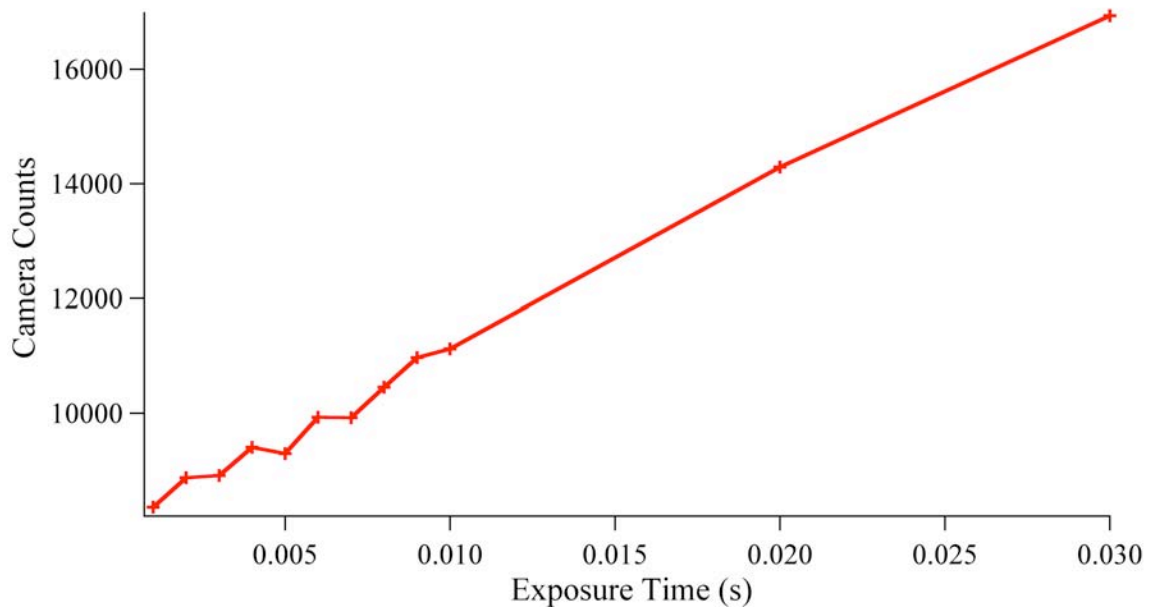


Fig. 4.1 A portion of the linearity calibration curve showing that the linearity breaks down below 0.007 s exposure time.

## 4.2. Spectral Calibration

In this calibration we use a monochromator (Optronics 740A) and a light source (740 -20A) to obtain monochromatic light (1 nm bandwidth), which is directed towards the system. We vary the wavelength of this incoming light by 20 nm on either side of the nominal center band of each filter, and make measurements every 1 nm for  $\pm 10$  nm and every 2 nm between  $\pm 20$  nm and  $\pm 10$  nm from the center band. With these images, the central wavelength and full-width at half maximum (FWHM) are calculated as shown in Table 4.1. Figure 4.2 shows the relative spectral system response of the different filters used in the DPOL.

Table 4.1 DPOL spectral calibration.

Filter No.	Band Center (nm)	Color	FWHM
1	520.6	green	10.8
2	550.1	green	15.3
3	589.1	yellow	10.3
4	649.2	red	9.2
5	Dark	---	---
6	411.1	violet	9.7
7	441.6	indigo	9.9
8	487.7	blue	10.4

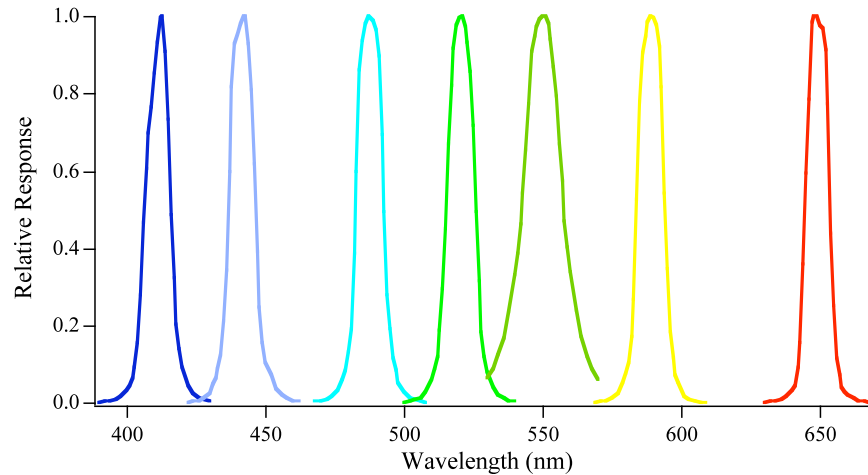


Fig. 4.2 Relative spectral system response for the DPOL system.

### 4.3. Flatfield Calibration

Because of nonuniformities in the optical fiber bundle, viewing a uniform source does not produce a uniform image. The fiber bundle has absorbing layers that are put into the bundle to reduce fiber cross talk. Some fibers also transmit better than others. In addition there is a variation in transmission at the fiber taper to fiber bundle connection. Therefore, we need to perform a calibration step to improve the image qualitatively and quantitatively. To do this calibration, I directly exposed the ends of the individual fiber bundles to the exit port of a 1 m integrating sphere without the fisheye lens or polarizers. I collected 20 to 30 images for each spectral filter. These images are then averaged together to form the flatfield image that is used in the rest of the calibration, and in data reduction. Figure 4.3 is an example image from this calibration and Fig. 4.4 shows the effect of the flatfield correction on a horizontal line of data.

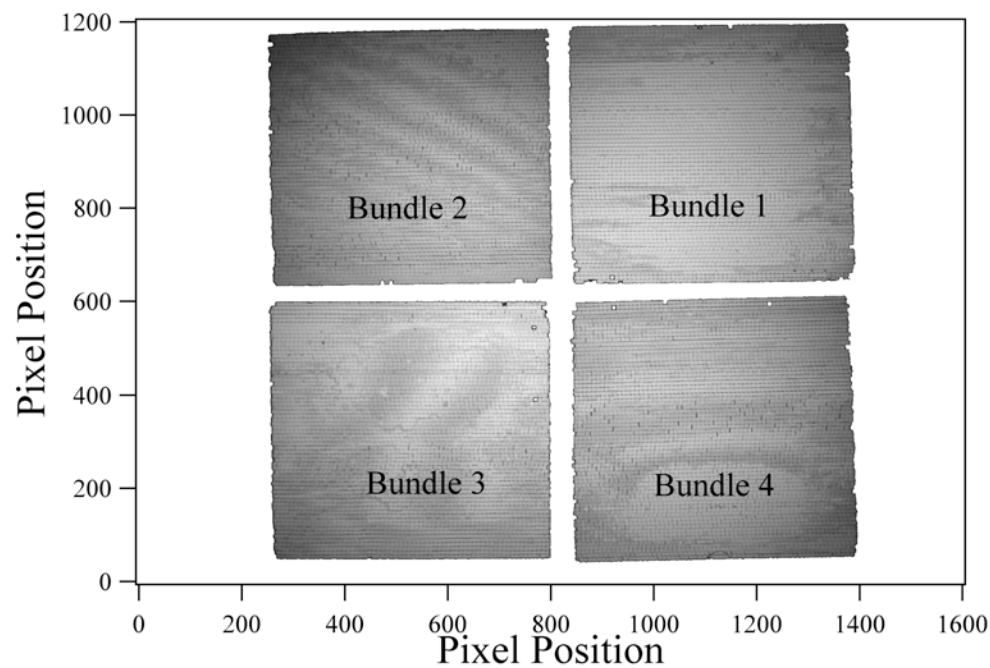


Fig. 4.3 The image resulting from illuminating the ends of the fibers with an integrating sphere.

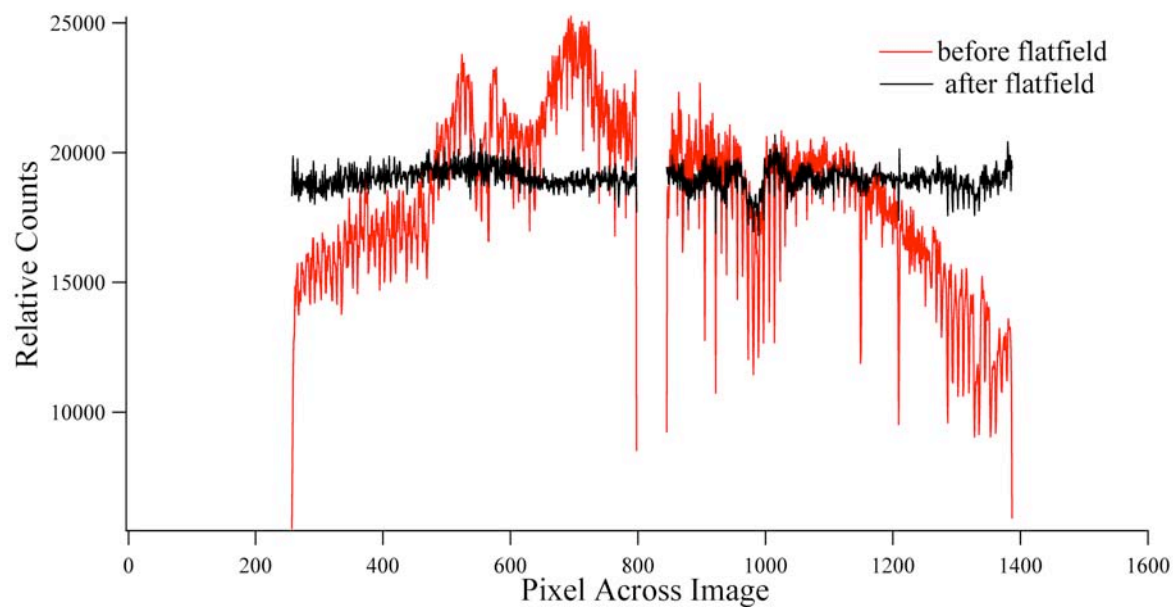


Fig. 4.4 Example line across a sample image showing the effect of using the flatfield correction.

To determine the effectiveness of this process another set of data was taken looking into the integrating sphere. The flatfield correction was applied to this image and a 20 x 20 pixel area in the center of the image of the integrating sphere exit port was extracted. The average and standard deviation was calculated for this area. The residual uncertainty, after the flatfield correction, was 5.3%.

#### 4.4. Angular Calibration, Geometrical Projection

A fisheye lens produces a hemispherical field of view of about 180°. The projection of the imaged light field onto the image is an equidistance projection for which the radial distance from the center on the image plane ( $r$ ) is given by Miyamoto (1964),

$$r = f\theta \quad (4.1)$$

where  $f$  is the focal length of the lens system and  $\theta$  is the view angle of a point source at infinity projected onto the image plane. I performed a calibration to determine the constant  $f$  for each lens system.

In this calibration, I place the camera system on a precision rotation mount at a distance of 3 meters from a small bright source and take images of this source while rotating the camera system from -80° to 80° in 10° steps. With these images, the distance of the image of the point source from the center of the image ( $r$ ) for the corresponding angle  $\theta$  can be found. The slope of the graph of  $\theta$  vs.  $r$  gives the radius-to-degree (rtd) conversion factor and is approximately equivalent to the inverse of the focal length  $f$  of the lens. Ultimately, the derived  $f$  allows us to compute the view angle (or zenith angle) for each element of the CCD array through Eq. (4.1). This calibration is done for all

lenses and to account for the effect of the dome window it is carried out in both air and water. The linearity of the data points in Fig. 4.5 shows that the optics exhibits a very linear-like projection- an almost ideal equidistance projection. Figure 4.5 presents the data for one of the lenses used. The rtd value obtained from this graph is  $0.357 \pm 0.0006$  pixels/degree with the correlation coefficient equal to 0.999. One of the important steps in the instrument construction is to place the effective 1<sup>st</sup> principal plane of the optics in the center of curvature of the dome window. To test how well this is done, we compare the conversion factors for this calibration step between the air measurements and in-water measurements. As can be seen below from data on Table 4.2, these factors are within 1.5% from each other. The rtd values in Table 4.2 suggest that 1 pixel in the CCD raw fisheye image integrates over nearly  $0.3^\circ$ .

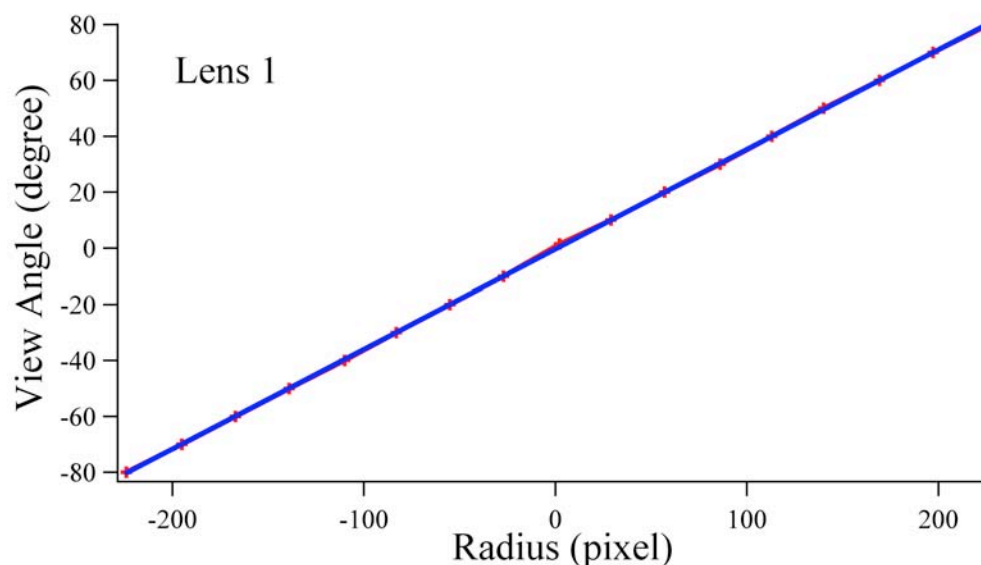


Fig. 4.5 Projection of the optics from angular calibration

Table 4.2 Lens radius-to-degree (rtd) conversion factors.

Lens	In water, pixel/degree	In air, pixel/degree
1	0.357±0.0006	0.354±0.0008
2	0.351±0.0009	0.347±0.0006
3	0.341±0.0012	0.338±0.0004
4	0.345±0.0014	0.340±0.0010

#### 4.5. Rolloff Calibration

The fisheye lens has a variation in transmission as a function of incidence angle, called the lens rolloff. This effect is more significant near the edge of the images, and must be accounted for in the data reduction process.

To do this calibration, the complete system is used with an integrating sphere as the source of uniform unpolarized light. Images are obtained with each lens, looking into the port of the integrating sphere and rotating the camera at many angles in both horizontal and vertical directions. For each image, corresponding dark images are recorded. For each lens, after subtracting the dark image from the corresponding light image, I superimpose all the images to form a single image. This single image contains all the field of views of the source for both horizontal and vertical directions of the camera. I then eliminate areas in the image that have not been illuminated. The camera counts and the corresponding radius are extracted for each pixel. Figure 4.6 shows the camera counts and corresponding radius and is fitted by a 5<sup>th</sup> order polynomial (represented by a blue curve). The 5<sup>th</sup> order polynomial is then used to characterize the

rolloff of these lens system. Figure 4.7 shows the rolloff factors for the 4 lenses (250 pixels radius corresponds to about 85 degrees zenith angle). The data images are then multiplied by an image generated with these polynomials to correct for the rolloff effect.

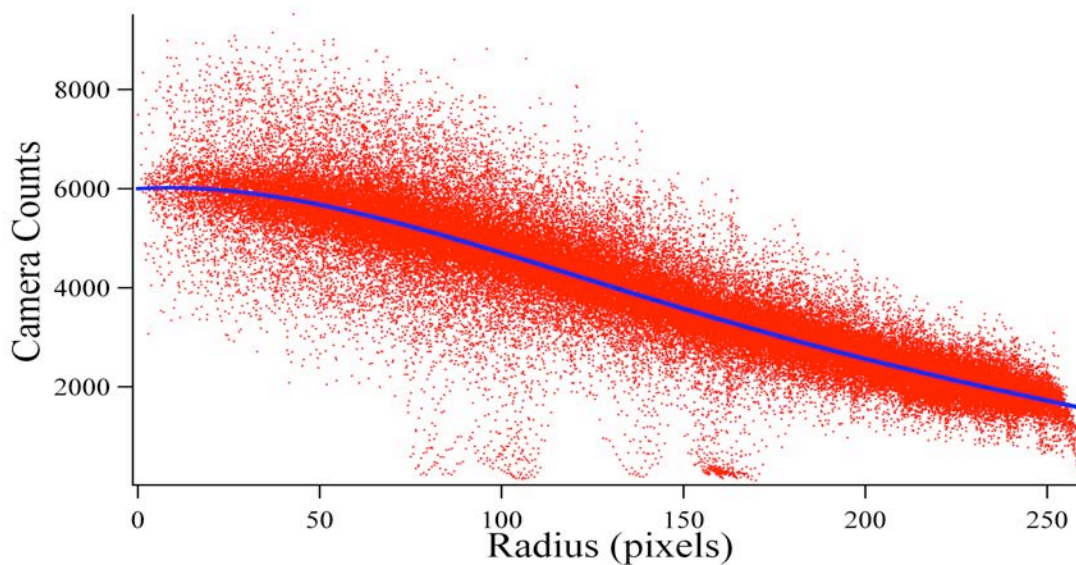


Fig. 4.6 Camera counts versus radius for a fisheye lens during rolloff calibration.

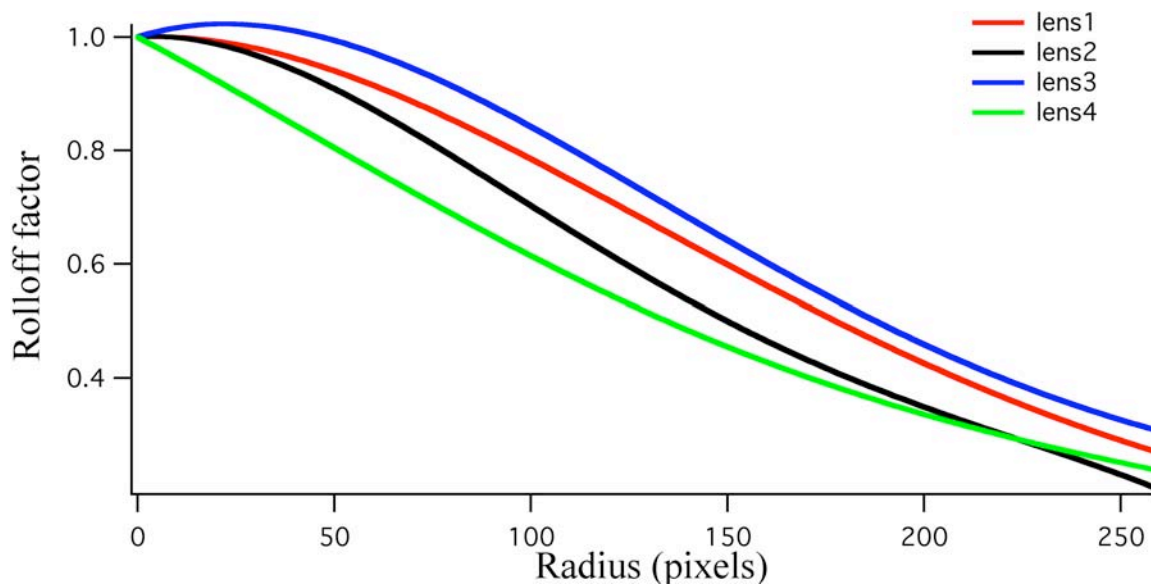


Fig. 4.7 Rolloff factor as a function of radius from center of image, for each lens.

#### 4.6. Polarization Calibration

We have used linear polarizers behind each of the three fisheye lenses in such a way that their transmission axes are oriented at approximately 0, 60 and 120 degrees relative to an axis aligned lengthwise along the instrument. The three linear polarizers are dichroic sheet polarizers (Melles Griot, 03 FPG 019). Behind the last fisheye lens is a circular analyzer which is a combination of a broadband mica quarter wave plate (Melles Griot, 02 WRM001) and a linear polarizer (Melles Griot, 03 FPG 019). To get polarization information from the images, we must understand how to combine the four images to get the Stokes vector. Various papers have been published on how to accomplish this (for example Tyo, 2002). As with most calibration steps, the basic premise is to introduce light with known characteristics (in this case polarization), and measure the instrument's response.

If we have  $n$  number of optical devices placed in order as shown in Fig. 4.8, then the incident Stokes vector ( $S$ ) is transformed into the emergent Stokes vector ( $S'$ ) by means of a linear transformation:

$$S' = M_n \dots M_3 \cdot M_2 \cdot M_1 \cdot S \quad (4.2)$$

where the  $M$ 's are the Mueller matrices of the optical elements.

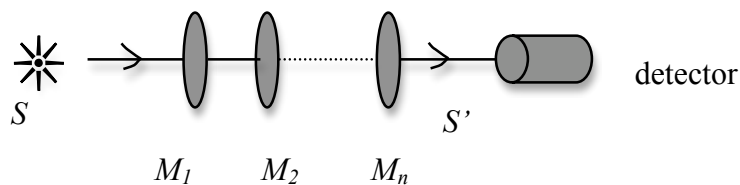


Fig. 4.8  $S$  is the incident Stokes vector,  $M$ 's are Mueller matrices of the optical devices and  $S'$  is the transmitted Stokes vector.

Many authors have used the polarization calibration to determine the effective system Mueller matrix for each polarizer position or, in our case, lens. Once this Mueller matrix is determined, the matrix can be inverted, and this inverted matrix is used to determine the unknown Stokes vector of incoming light in the experimental setting. In our case we take the measurements by each lens for a specific incoming polarization state, and compare this with what we expect the Stokes vector to be. We perform a multi-variable linear regression with the independent variables being the instruments counts for the 4 sub images, and the dependent variable being the known  $I$ ,  $Q/I$ ,  $U/I$ , or  $V/I$ . In this way we determine a 4 x 4 transformation matrix. This transformation matrix can then be directly used to transform the input intensity information from each lens into a normalized Stokes parameters, and then, with an absolute calibration, into S.I. based Stokes parameters.

For this calibration we have used a Left-Hand-Circular-Polarizer (LHCP, Alight PFC) which is a combination of a linear polarizer and a quarter wave plate. If the linear polarizer side is towards the detector (DPOL) it acts as a linear polarizer, otherwise it acts as a circular /elliptical polarizer. Before finding the transformation matrix, we need to characterize the LHCP in terms of its transmission axis (when used as a linear polarizer), retardation angle and the fast axis angle of the quarter wave plate (when used as a circular polarizer) with respect to a known reference axis.

For an unpolarized source of monochromatic light the Stokes vector  $S$  is given by

$$S = \begin{pmatrix} 1 \\ 0 \\ 0 \\ 0 \end{pmatrix}. \quad (4.3)$$

The Mueller matrix for a linear polarizer can be represented as follows:

$$M_{LP} = \begin{bmatrix} k_1 + k_2 & (k_1 - k_2)\cos 2\theta & (k_1 - k_2)\sin 2\theta & 0 \\ (k_1 - k_2)\cos 2\theta & (k_1 + k_2)\cos^2 2\theta + 2\sqrt{k_1 k_2} \sin^2 2\theta & (k_1 + k_2 - 2\sqrt{k_1 k_2})\cos 2\theta \sin 2\theta & 0 \\ (k_1 - k_2)\sin 2\theta & (k_1 + k_2 - 2\sqrt{k_1 k_2})\cos 2\theta \sin 2\theta & (k_1 + k_2)\sin^2 2\theta + 2\sqrt{k_1 k_2} \cos^2 2\theta & 0 \\ 0 & 0 & 0 & 2\sqrt{k_1 k_2} \end{bmatrix} \quad (4.4)$$

where  $k_1$  and  $k_2$  are the transmittances of the polarizer along the preferred axis and an axis perpendicular to this reference axis. For an ideal polarizer  $k_1 = 1$  and  $k_2 = 0$ .  $\theta$  is the angle between the polarizer transmittance plane and a reference plane. The Mueller matrix for a retarder having retardation angle  $\phi$  and whose fast axis angle is rotated by an angle  $\theta_f$  with respect to a reference axis is represented as follows (Goldstein, 2003):

$$M_{Ret} = \begin{bmatrix} 1 & 0 & 0 & 0 \\ 0 & \cos^2 2\theta_f + \cos \phi \sin^2 2\theta_f & (1 - \cos \phi)\sin 2\theta_f \cos 2\theta_f & -\sin \phi \sin 2\theta_f \\ 0 & (1 - \cos \phi)\sin 2\theta_f \cos 2\theta_f & \sin^2 2\theta_f + \cos \phi \cos^2 2\theta_f & \sin \phi \cos 2\theta_f \\ 0 & \sin \phi \sin 2\theta_f & -\sin \phi \cos 2\theta_f & \cos \phi \end{bmatrix} \quad (4.5)$$

#### 4.6.1. Transmission Axis Angle ( $\theta_p$ )

The LHCP is temporarily mounted on a circular mount inscribed with an index from 0 to 360 degrees. It is illuminated by a source of monochromatic light using a monochromator (Optronics 740A) and an unpolarized light source (740 - 20A). After the LHCP, which is placed with the linear polarizer side towards the detector, I placed an external linear polarizer with its transmission axis horizontal and then a detector. The linear polarizer (LHCP in this orientation) is rotated to find the minimum intensity, indicating that the transmission axes of the two polarizers are crossed. Then the LHCP is rigidly fixed in the circular mount so that its transmission axis is horizontal at  $0^\circ$  reading of the circular mount. To determine the transmission axis angle ( $\theta_p$ ) of this LHCP with respect to the transmission axis angle of the external linear polarizer, I set up an experiment as shown in Fig. 4.9. In Fig. 4.9,  $M_{LP}(\theta_p)$  and  $M_{Rc, \phi}(\theta_p, \phi)$  represent the linear polarizer and quarter wave plate in the circular polarizer and  $M_{LP}(\theta)$  is the external linear polarizer. I recorded the intensities,  $I(\theta)$ , at point D for every  $10^\circ$  clockwise (as viewed from source) rotation of the external linear polarizer through  $0^\circ$  to  $180^\circ$ . Then, the Stokes vector of the light field at point D can be represented as follows:

$$S' = M_n \cdot M_2 \cdot M_1 \cdot S. \quad (4.6)$$

From Eq. 4.6, and using Eqs. 4.3 and 4.4 for an ideal polarizer ( $k_1 = 1$  and  $k_2 = 0$ ), the intensity,  $I(\theta)$ , at the detector D is also given by,

$$I(\theta) = 1 + \cos 2\theta_p \cos 2\theta + \sin 2\theta_p \sin 2\theta. \quad (4.7)$$

By curve fitting to Eq. 4.7, the value of  $\theta_p$  with respect to the transmission axis angle of the external linear polarizer was calculated.

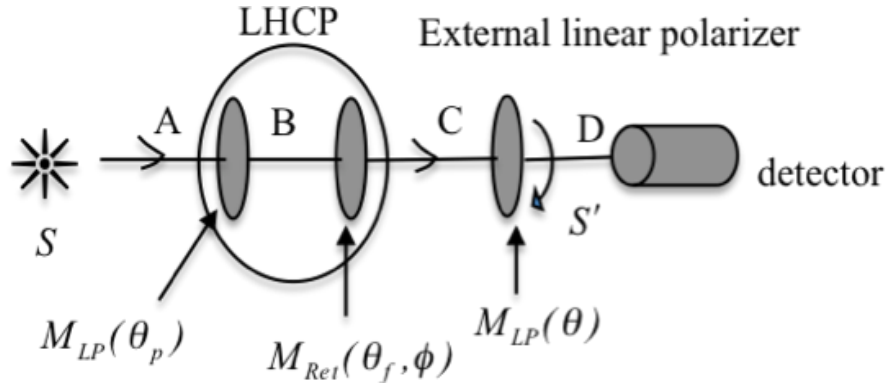


Fig. 4.9 Experimental set up for the measurement of the transmission axis angle of LHCP when used as a linear polarizer.  $S$  is a nearly unpolarized source of monochromatic light.

#### 4.6.2. Fast Axis Angle ( $\theta_f$ ) and Retardation Angle ( $\phi$ )

The experimental set up is similar to the previous case (Fig. 4.9) except that the LHCP is inverted. The LHCP is fixed with its transmission axis in a horizontal direction. For each central wavelength used in DPOL, the intensities were recorded as the external linear polarizer rotated clockwise as viewed from the source through  $180^\circ$  in  $10^\circ$  steps.

Then,  $S'$  at position D can be written as:

$$S' = M_{LP}(\theta)M_{Ret}(\theta_f, \phi)M_{LP}(\theta)S \quad (4.8)$$

By setting  $k_1 = 1$  and  $k_2 = 0$  and using Eqs. (4.3), (4.4), (4.5) and (4.8), the intensity at the detector (D) is given by the expression

$$I'(\theta) = 1 + \cos 2\theta [\cos 2\theta_p (\cos^2 2\theta_f + \cos \phi \sin^2 2\theta_f) + \sin 2\theta_p (1 - \cos \phi) \sin 2\theta_f \cos 2\theta_f] \\ + \sin 2\theta [\cos 2\theta_p (1 - \cos \phi) \sin 2\theta_f \cos 2\theta_f + \sin 2\theta_p (\sin^2 2\theta_f + \cos \phi \cos^2 2\theta_f)]$$

(4.9)

Here,  $\theta_p$ , which is already determined in section 4.6.1, has to be used, but with the opposite sign as the LHCP has been flipped. From curve fitting to Eq. (4.9), we can find the values of  $\theta_f$  and  $\phi$  for each spectral filter with respect to the same reference axis used to determine  $\theta_p$ . Table 4.3 shows these angles and the derived normalized Stokes vector of transmitted light obtained in the lab for unpolarized incident light. Table 4.4 shows the same parameters as in Table 4.3 but determined using the manufacture's specification of the circular polarizer.

Table 4.3 Transmission axis angle ( $\theta_p$ ), fast axis angle ( $\theta_f$ ), retardation angle ( $\phi$ ) and the derived values for the normalized Stokes vector for the LHCP determined in the lab.

Spectral filters nm	$\theta_p \pm \text{std}$ degrees	$\theta_f \pm \text{std}$ degrees	$\phi \pm \text{std}$ degrees	$Q/I$	$U/I$	$V/I$
411.1	2.86 $\pm$ 0.44	47.6 $\pm$ 0.15	104.9 $\pm$ 0.15	-0.257	-0.014	0.966
441.6	2.86 $\pm$ 0.44	47.4 $\pm$ 0.02	103.7 $\pm$ 0.06	-0.237	-0.004	0.971
487.7	2.86 $\pm$ 0.44	47.4 $\pm$ 0.03	103.8 $\pm$ 0.07	-0.239	-0.004	0.971
520.6	2.86 $\pm$ 0.44	47.5 $\pm$ 0.02	88.8 $\pm$ 0.03	0.020	0.014	1.000
550.1	2.86 $\pm$ 0.44	47.9 $\pm$ 0.08	84.7 $\pm$ 0.14	0.092	0.008	0.996
589.1	2.86 $\pm$ 0.44	48.0 $\pm$ 0.09	80.4 $\pm$ 0.15	0.166	0.013	0.986
649.2	2.86 $\pm$ 0.44	48.4 $\pm$ 0.07	73.3 $\pm$ 0.10	0.287	0.015	0.960

Table 4.4 Same parameters as in Table 4.3, but determined using manufacturer's specification.

Spectral filters nm	$\theta_p$ degrees	$\theta_f$ degrees	$\phi \pm$ variance degrees	$Q/I$	$U/I$	$V/I$
411.1	0	45	$122.6 \pm 8.8$	-0.539	0	0.842
441.6	0	45	$114.1 \pm 8.2$	-0.409	0	0.913
487.7	0	45	$103.3 \pm 7.4$	-0.231	0	0.973
520.6	0	45	$96.8 \pm 6.9$	-0.119	0	0.993
550.1	0	45	$91.6 \pm 6.5$	-0.028	0	1.000
589.1	0	45	$85.6 \pm 6.1$	0.077	0	0.997
649.2	0	45	$77.6 \pm 5.5$	0.214	0	0.977

#### 4.6.3 Polarization Calibration of DPOL

After finding  $\theta_p$ ,  $\theta_f$  and  $\phi$  of the LHCP we perform the polarization calibration of DPOL. For this we place the LHCP between an unpolarized uniform source of light (integrating sphere) and the lenses of DPOL (Fig. 4.10). Using both sides (circular and linear) of the LHCP, the LHCP is rotated through  $180^\circ$  in  $10^\circ$  steps in a clockwise direction as viewed from the source. Images are obtained at each step, for each lens, and for each wavelength. Because of the physical layout of the instrument, and the port size of the integrating sphere, we had to do this sequentially for each lens. It was also necessary to do this for each spectral filter. For each image, an area (5 x 5 pixels) in the center of the illuminated part of the array is extracted as representing the response of the system to that polarization state.

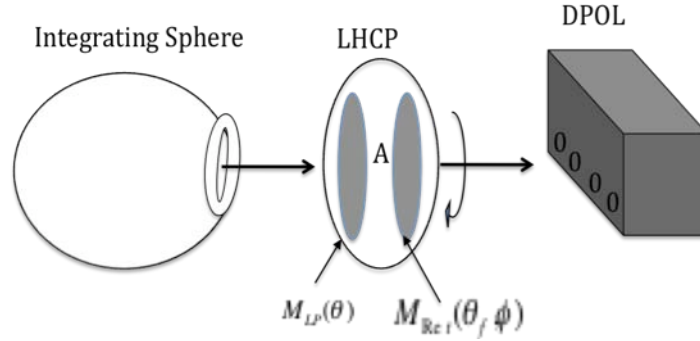


Fig. 4.10 Experimental set up of the circular (as well as linear) calibration of the DPOL.

Assuming the integrating sphere to be an unpolarized homogeneous source of light, the Stokes vector is given by Eq. 4.3. Then using the matrices for the linear polarizer (Eq. 4.4, assuming the ideal case) and the quarter wave plate (Eq. 4.5) of the LHCP, the normalized Stokes vector of the light incident on DPOL when the circular polarizer side is used is, represented as:

$$S = \begin{pmatrix} 1 \\ \cos 2\theta(\cos^2 2\theta_f + \cos \phi \sin^2 2\theta_f) + \sin 2\theta(1 - \cos \phi) \sin 2\theta_f \cos 2\theta_f \\ \cos 2\theta(1 - \cos \phi) \sin 2\theta_f \cos 2\theta_f + \sin 2\theta(\sin^2 2\theta_f + \cos \phi \cos^2 2\theta_f) \\ \cos 2\theta \sin 2\theta_f \sin \phi - \sin 2\theta \cos 2\theta_f \sin \phi \end{pmatrix}. \quad (4.10)$$

On the other hand, when the linear polarization side is used, then the normalized Stokes vector of the light incident on DPOL becomes

$$S = \begin{pmatrix} 1 \\ \cos 2\theta \\ \sin 2\theta \\ 0 \end{pmatrix} = \begin{pmatrix} 1 \\ Q/I \\ U/I \\ V/I \end{pmatrix}. \quad (4.11)$$

After determining the polarization angle ( $\theta_p$ , which is to be subtracted or added to the rotation angle  $\theta$ ), fast axis angle ( $\theta_f$ ), and the retardation angle ( $\phi$ ) of the LHCP, we can calculate the Stokes vector of light incident on DPOL using Eqs. (4.10) and (4.11). If  $I_1(\theta)$ ,  $I_2(\theta)$ ,  $I_3(\theta)$ , and  $I_4(\theta)$  represent the intensities for lens 1, lens 2, lens 3 and lens 4 respectively then we can relate these intensities to the incident Stokes vector in terms of the transformation matrix by the following equation.

$$\begin{pmatrix} 1 \\ Q/I \\ U/I \\ V/I \end{pmatrix} = \begin{pmatrix} T_{11} & T_{12} & T_{13} & T_{14} \\ T_{21} & T_{22} & T_{23} & T_{24} \\ T_{31} & T_{32} & T_{33} & T_{34} \\ T_{41} & T_{42} & T_{43} & T_{44} \end{pmatrix} \begin{pmatrix} I_1(\theta) \\ I_2(\theta) \\ I_3(\theta) \\ I_4(\theta) \end{pmatrix} \quad (4.12)$$

By performing a multi-variable linear regression for the 38 data points (19 for linear side and 19 for circular side) for each Stokes vector element in Eq. (4.12), we can determine the 4 x 4 transformation matrix. Note that if we are interested in only the linear polarization calibration then we use only the linear polarization side of the polarizer and the first three lenses of DPOL which have linear polarizer's behind them. In this case we ignore the fourth row and fourth column in Eq. (4.12) and obtain a 3 x 3 transformation matrix. Figure 4.11 shows the variation in the camera counts for the 550 nm channel as seen by each lens with the rotation of linear (A) and circular (B) polarizer's between the lens and the source.

Figure 4.12 shows the expected values of the normalized Stokes vector and the error in generating the Stokes vectors with the transformation matrix, as a function of polarizer angle of the external polarizer. This error is the difference (predicted – reconstructed) of the normalized Stokes vectors. The average error in these reconstructed

vectors is significantly less than 0.02%. The RMS difference is 0.005, 0.009, 0.008 and 0.029 for  $I$ ,  $Q/I$ ,  $U/I$ , and  $V/I$  respectively. In this analysis we have not included the filter at 410 nm because there is insufficient flux from the integrating sphere at this wavelength.

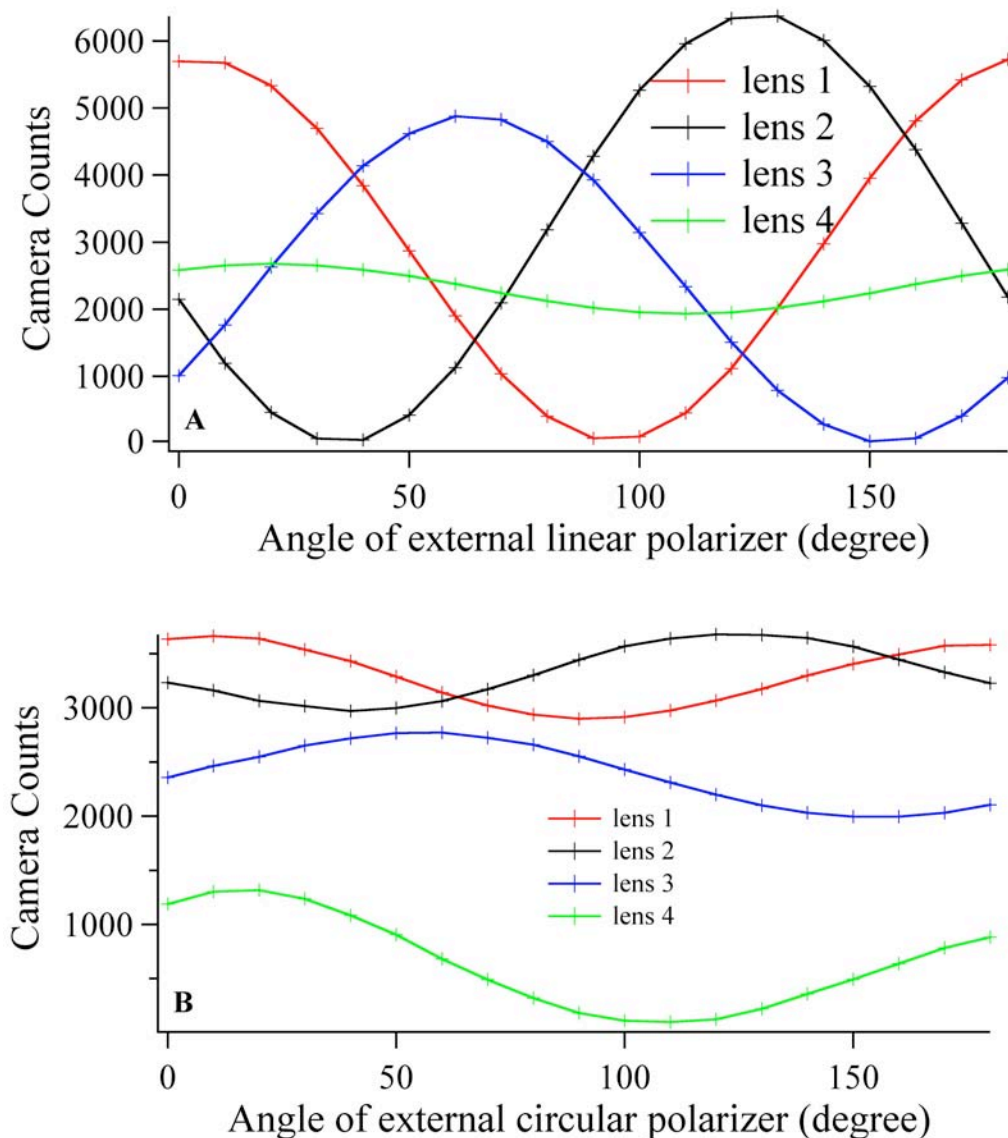


Fig. 4.11 The camera counts versus angle of the external linear (A) and circular (B) polarizer as seen by the different lenses for 550 nm wavelength. Behind lens 1, lens 2, lens 3 are linear polarizers at approximately 0, 60 and 120 degrees with respect to an arbitrary axis and behind the fourth lens is a circular analyzer. In the circular case, lens 4 data has been multiplied by a factor of 10.

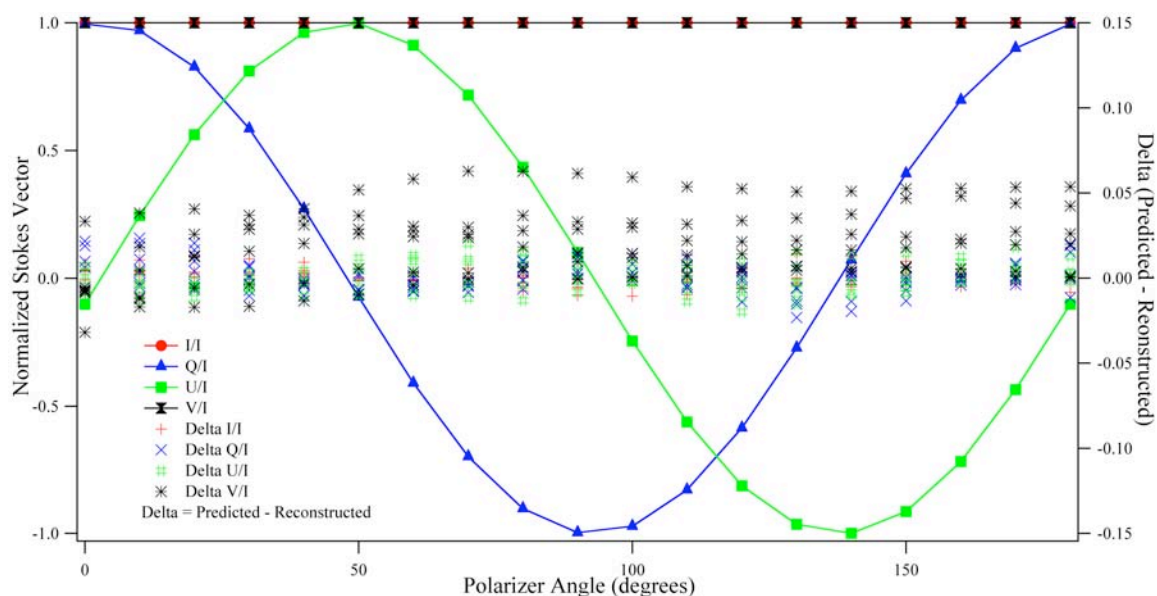


Fig. 4.12 Normalized Stokes Vectors and difference between predicted and constructed normalized Stokes vectors (Delta).

#### 4.7. Absolute Calibration

This calibration basically follows Voss and Zibordi (1989). However, in this case the camera information must first be processed with the transformation matrix to get the relative intensity, along with the other Stokes parameters. This intensity is converted into an absolute intensity by determining the absolute radiometric calibration factor. In the experimental set up, we combine four barium sulphate plaques (each has dimension of 25.4 cm x 25.4 cm) to form a single plaque (50.8 cm x 50.8 cm). This plaque is placed at a distance of 100 cm from a 1000 W standard spectral irradiance lamp (whose calibration is traceable to NIST) on an optical rail and is illuminated at normal incidence with the lamp. The centers of the lamp, plaque and that of the camera lenses are at the same height and the plaque is viewed with DPOL at  $45^\circ$  to the plaque normal about 90 cm from the plaque. Figure 4.13 shows a schematic diagram of the experimental setup.

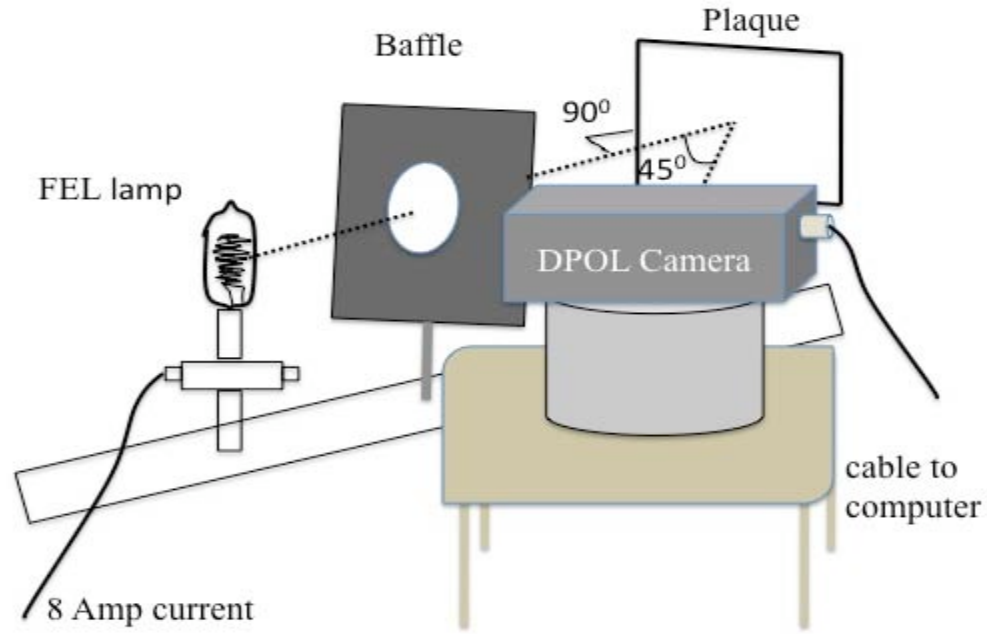


Fig. 4.13 Schematic diagram of experimental setup of the absolute calibration.

Considering the plaque to be Lambertian, its radiance ( $L$ ) is related to the irradiance of the lamp ( $E$ ) by the following equation (Carol et al., 1995),

$$L(\lambda) = \frac{R(0^\circ/45^\circ, \lambda)}{\pi} \left( \frac{50}{r} \right)^2 E(\lambda, 50 \text{ cm}) \quad (4.13)$$

where  $R(0^\circ/45^\circ, \lambda)$  is the directional/directional reflectance factor of the plaque for the typical measurement condition (illumination at normal incidence and viewing at  $45^\circ$ ) and is 1.00 in our spectral range,  $r$  is the distance of the plaque from the lamp in cm, and  $E(\lambda, 50 \text{ cm})$  is the known spectral irradiance of the lamp at 50 cm from the detector.

The absolute radiometric calibration factor  $A(\lambda)$  is then given by the formula

$$A(\lambda) = \alpha \frac{L(\lambda)}{L_i} \quad (4.14)$$

where  $L_r$  is the average relative intensity value obtained from images and  $\alpha$  is a constant which depends upon the conditions of the field data measurement. In the case of DPOL, we have used a glass dome to shield the fisheye lenses from water. In this case,  $\alpha$  is given by,

$$\alpha = \frac{1}{T_{w|g} \cdot T_{g|a}} = \frac{1}{(1 - R_{w|g})(1 - R_{g|a})} \quad (4.15a)$$

where

$$R_{1/2} = \frac{(n_1 - n_2)^2}{(n_1 + n_2)^2}. \quad (4.15b)$$

Here,  $T$  and  $R$  represent the Fresnel transmittance and reflectance coefficients respectively. The subscripts  $a$ ,  $w$  and  $g$  represent air, water and glass respectively.  $n_1$  and  $n_2$  are the refractive indices of the two media, air and glass or water and glass.

In the calibration procedure we take three separate images of the reflectance plaque for each of the wavelengths. Signal level counts (i.e., average linearized value) were determined by extracting a 10 x 10 pixel area from the center of the plaque image. We can then permute through the images from each lens to get 27 estimates of the intensity (and Stokes parameters  $Q$  and  $U$ ). When this was done, the standard deviation of these estimates was on the order of 0.5% or less, showing that the values obtained are fairly uniform.

#### 4.8. Immersion Calibration

This calibration is done to take into account the difference between the measurements made in air (where most of the calibrations are done) versus those in water where the desired measurements are performed. Since the four fisheye lenses and the 4 hemispherical dome windows may not be identical, we must perform this calibration for each lens and window. The whole purpose of this calibration is to find the immersion factor which includes the difference in the transmission effects between air-glass and water-glass, to consider the effects of index of refraction ( $n^2$ ) between air inside the instrument and water outside it, and to consider any other effects caused by the fisheye lenses. The calibration process is similar to the one described by Voss and Chapin (2005).

To do this calibration in the lab, the camera system (in field configuration) is placed in a bucket about 50 cm below a plaque oriented at  $45^\circ$  to the vertical and the plaque is illuminated by a 1000W FEL lamp. The center of the lens and dome window lies vertically below the center of the plaque. The bucket is filled with water up to 8 cm above the dome's upper surface. Then, by lowering the water level in the bucket, images of the plaque are taken for different water levels, with at least one image when the dome is barely wet and one image when it is completely dry. This is done for each lens and each spectral filter. A 10 x 10 pixel area from the center of the image, viewing the plaque, is extracted and averaged for each measurement. If  $L_{water}$  and  $L_{air}$  represent the apparent radiances of the plaque as seen by the camera lens when it is in water and in air respectively, we can write an equation to relate the water attenuation and to compensate for the air-water interface as,

$$L_{water} = L_{air} e^{-cr} n^2 T_{water/air} \quad (4.16)$$

where  $c$  represents the water attenuation coefficient,  $r$  is the water level height above the glass dome,  $n$  is the index of refraction of the water and  $T$  is the Fresnel transmission coefficient through the air-water interface. Finally, the immersion factor ( $M$ ) is calculated as

$$M = \frac{count_{dry} n^2 T_{air/water} T_{water/glass}}{count_{wet} T_{air/glass}}, \quad (4.17)$$

where  $count_{dry}$  and  $count_{wet}$  are the observed counts when the dome window is dry and wet respectively.

The average count extracted from a 10 x 10 pixel area from the center of the image ( $L_{avg}$ ) at a depth ( $r$ ) can be related to the count ( $L_o$ ) when the glass dome is barely wet by equation

$$L_{avg} = L_o e^{-cr} \quad (4.18)$$

Taking the logarithm on both sides of Eq. 4.18 we will get the following equation:

$$\ln(L_{avg}) = \ln(L_o) - cr. \quad (4.19)$$

The  $count_{wet}$ , which is  $L_o$  in this case, can also be obtained by plotting a graph of the logarithm of  $L_{avg}$  at various depths of the water versus the corresponding depths.  $L_o$  is the intercept of this line. This  $L_o / count_{dry}$  can be compared to the one obtained with the simple ratio ( $M = \frac{count_{dry}}{count_{wet}}$ ). Figure 4.14 shows this plot for one of the lenses and one of

the spectral filters in DPOL. However, this graph is not consistent with most of the other spectral filters and lenses. In many cases, because the water attenuation is not significant over an 8 cm path length, noise dominates the procedure. So we generally use the simple ratio (Eq. 4.17).

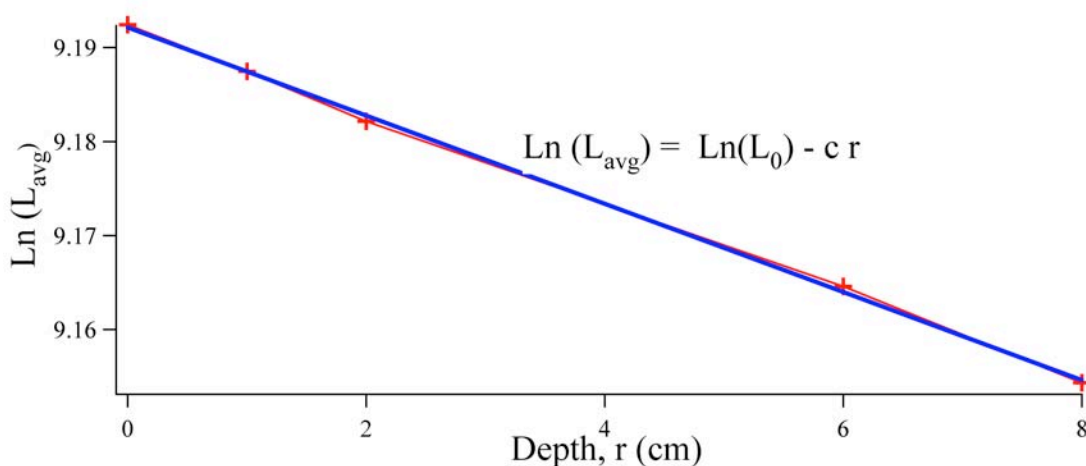


Fig. 4.14 An example of a plot of logarithm of the average counts vs. the depth of the instrument for the immersion calibration.

Table 4.5 presents the immersion coefficients  $M$  for the DPOL camera system obtained from calibration on different dates. Since the immersion factor does not vary much with the spectral filters used, the data for each lens corresponds to the average value of all the spectral filters for that lens. For each lens, values of  $M$  obtained from the experiment (using Eq. 4.17) and that obtained from the fit (as described in Fig. 4.14) have been shown. In the Table 4.5, the cells are denoted by 'na' when the fitting procedure did not work.

Table 4.5 Immersion coefficients from different calibration dates:

Date	Lens 1		Lens 2		Lens 3		Lens 4	
	expt.	fit	expt.	fit	expt.	fit	expt.	fit
Oct 10, 2009	1.80	1.79	1.80	1.79	1.83	1.80	1.82	1.84
Aug 06, 2009	1.79	na	1.80	na	1.80	na	1.81	na
May 11, 2009	1.80	1.81	1.77	1.79	1.78	1.78	1.79	1.76
Dec 04, 2008	1.85	1.84	1.81	1.80	1.81	1.77	1.80	1.79
Nov 25, 2008	1.80	na	1.78	na	1.69	na	1.76	na
Aug 06, 2008	1.81	na	1.81	na	1.79	na	1.80	na
Mar 03, 2008	1.80	1.82	1.78	1.78	1.79	1.80	na	na
Nov 28, 2007	1.80	na	1.84	na	1.78	na	1.81	na

#### 4.9. Tilt-Roll Calibration

We have a gyro-enhanced orientation sensor (3DM-GXI, Micro Strain), which communicates via an RS-232 interface, in the instrument. To obtain the information on the Euler angles (pitch, roll, and yaw) of the instrument during the data measurement this sensor must be calibrated. To do this calibration, I used a digital protractor (Lucas Model DP45), with accuracy of  $\pm 0.1^\circ$  between  $0^\circ$  to  $10^\circ$  and 1.5 % between  $10^\circ$  to  $45^\circ$ . The camera is placed with the lenses facing up. For the pitch calibration, the camera is rotated clockwise as well as counterclockwise about an axis which passes lengthwise through the center of the instrument. Similarly, for the roll calibration the camera is rotated about an

axis, which passes widthwise through the center of the instrument. At every  $\pm 5^\circ$  rotation, I recorded the corresponding pitch and roll values of the tilt-roll sensor. Figures 4.15 (A and B) show the pitch and roll output of the sensor versus the angle of rotation. In Fig. 4.15A for the pitch calibration, the positive values represent the counterclockwise rotation of the instrument as viewed from the connector side of the camera. In Fig. 4.14B for the roll calibration, the positive (negative) values represent the rotation of the camera such that the connector side goes down (up). I did not perform the yaw calibration, which requires a nonmagnetic environment, as it is not required at this point. We use the sun (for downwelling) or anti solar point (for upwelling) as an azimuthal reference.

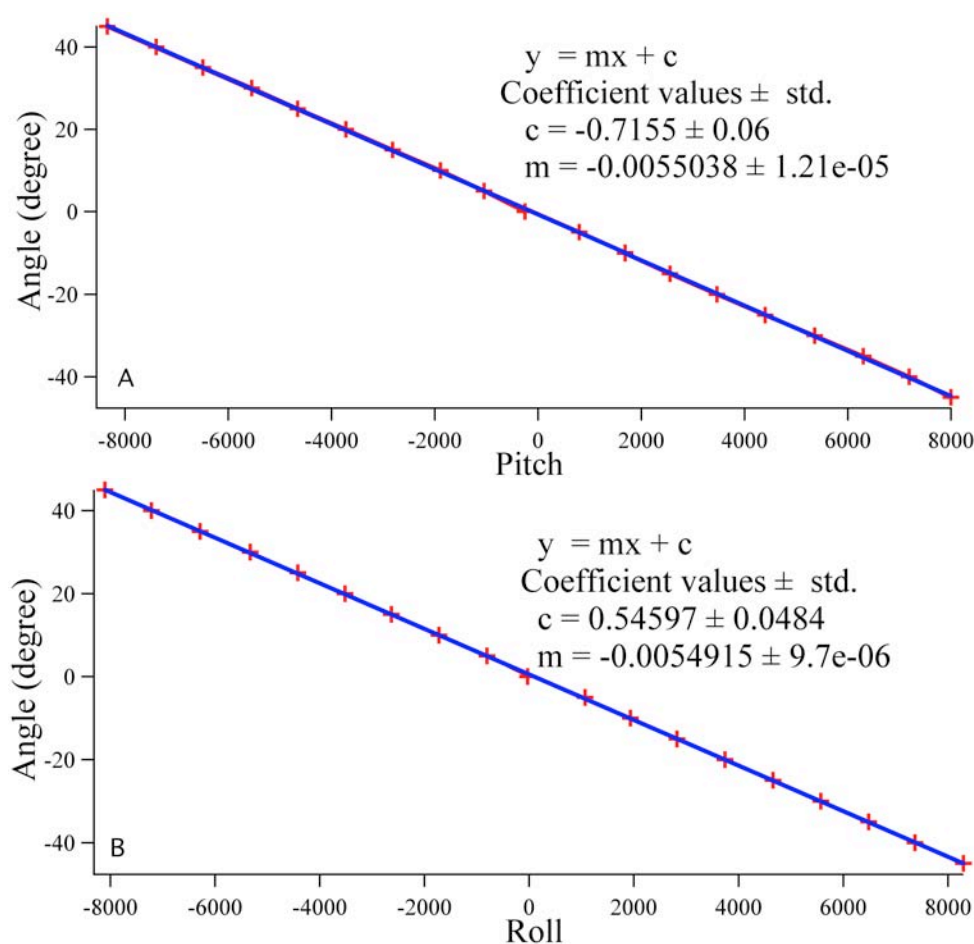


Fig. 4.15 Pitch (A) and Roll (B) calibration results of the tilt roll sensor.

#### 4.10. Pressure Transducer Calibration

We have used a pressure transducer (Model TJE, Honeywell) in the instrument to find the instrument depth during data measurement. Its output is an analog signal, ranging from 0 to 5 VDC, that is directly proportional to the external pressure. This analog output is converted to a digital value by the use of an analog to digital converter in the small microprocessor installed in the instrument. It was calibrated in the lab using a precision manometer and pressurized air. The result is shown in Fig. 4.16.

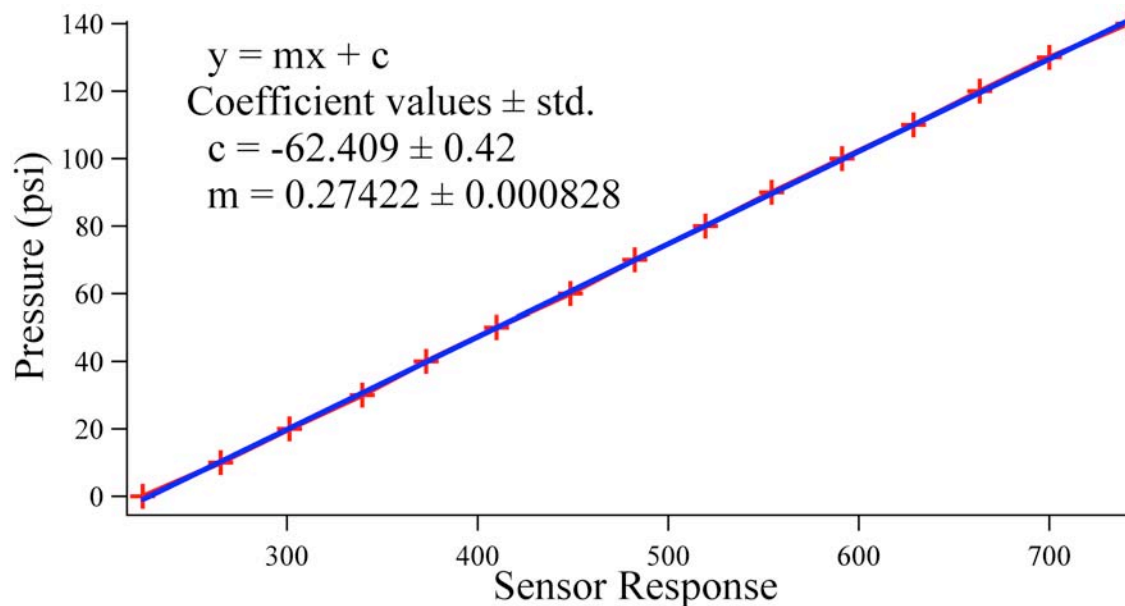


Fig. 4.16 Pressure transducer calibration result.

With these characterizations and calibrations, we are prepared to reduce the field data.

#### 4.11. Uncertainty in Stokes Vector Retrievals

The uncertainties in the retrieval of the Stokes vector and other derived parameters such as  $DoP$  and  $PoP$  come from several sources. In DPOL system since we use four fisheye images to retrieve the Stokes vector, the uncertainties in how each fisheye lens system is characterized can enter into the overall uncertainty or error. In the polarimeters consisting of more than one camera such as in PolRADS (Voss and Souidia, 2010), the major part of the uncertainties come from the differences in shutter timing between the cameras, and due to the misalignment of these cameras. We have avoided these uncertainties in the DPOL system by using a single camera. However, in this system, the optical fiber bundle that is required to split a single CCD image into four images has caused the major source of uncertainty. This is the residual uncertainty due to the fiber bundle irregularities. To estimate this source of uncertainty I performed the following numerical experiment. I inverted the transformation matrix and used Eq. 2.13d to determine the intensities that would result for each lens system, for a given Stokes vector input. I then added a random noise factor to each lens intensity that was distributed in a Gaussian fashion, with a width given by the residual uncertainty (5.3%) determined in section 4.3. This was done 10,000 times, and I calculated the resulting mean and standard deviation for the derivation of  $I$ ,  $Q/I$ ,  $U/I$ , and  $V/I$  along with the  $DoP$  and  $DoLP$ . In all cases the mean  $I$ ,  $Q/I$ ,  $U/I$  and  $V/I$  were found to lie within 0.1% for  $I$  and 0.001 for  $Q/I$ ,  $U/I$ , and  $V/I$  of the expected values. The standard deviation though varied between the parameters, and averaged 0.03%, 0.05, 0.05, 0.06 for  $I$ ,  $Q/I$ ,  $U/I$ , and  $V/I$  respectively. Because the  $DoP$  and  $DoLP$  are calculated from the squares of the  $Q/I$ ,  $U/I$  and  $V/I$  (the last in the case of  $DoP$ ), when the  $DoP$  or  $DoLP$  are large (near 1) the

mean value is within 1% of the expected value. The standard deviations for the *DoP* and *DoLP* average 0.04 and 0.03 respectively. However, when the input light is unpolarized, because the retrieved values of  $Q/I$ ,  $U/I$  and  $V/I$  will bounce around zero, the mean value for the *DoP* and *DoLP* was 0.07 and 0.05 respectively, biased slightly high.

The uncertainty in the calculation of the transformation matrix is estimated to be 2% based on the residual errors in the calibration and the uncertainty in deriving each matrix element. There is an additional uncertainty due to the absolute radiance calibration for  $I$  that is estimated to be 5% and is due to uncertainties in the lamp irradiance, laboratory setup, and spectralon plaque reflectance. The combination of these uncertainties leads to the measurement uncertainties for  $I$ ,  $Q/I$ ,  $U/I$ , and  $V/I$  of 6%, 0.06, 0.06, and 0.07 respectively. For the *DoP* and *DoLP* the uncertainty is 0.05 and 0.04 respectively, but there is an additional bias at low *DoP* and *DoLP*. The values of *DoP* and *DoLP* are within 0.01 for expected values  $> 0.20$ . However for values less than this the bias gradually increases and reaches a minimum value for the *DoP* and *DoLP* of 0.07 and 0.05 for unpolarized light.

## CHAPTER 5. FIELD EXPERIMENTS AND DATA REDUCTION OVERVIEW

### 5.1. Field Experiments

We participated in two field experiments under the Office of Naval Research RaDyO (Radiance under a Dynamic Ocean) program in Santa Barbara Channel (SBC) ( $34^{\circ}12.31' \text{ N } 119^{\circ}37.725' \text{ W}$ ) on September 9-23, 2008 and in Hawaii ( $17^{\circ}49' \text{ N } 155^{\circ} \text{ W}$ ) on September 1-12, 2009. In both experiments, we collected data from the R/P FLIP (Floating Instrument Platform) (Fig. 5.1A), which is a long vessel (108 m) designed to partially flood and pitch backward 90 degrees. When flipped, it still has about 90 m in the water, which helps the FLIP to become a stable platform mostly immune to wave action. The underwater part and three booms of the FLIP can be used to deploy various instruments to collect in-water and sky data. Besides the stability, the long booms (about 15 m) and the cylindrical shape with only about 8 m in diameter of the FLIP minimize the problem of shadow on the instruments during measurement. We used DPOL (Voss et al., 2008) in water and Sky-Cam (similar to that of Voss and Liu, 1997) in air to collect data on the downwelling polarized radiance distribution. In most cases simultaneous sky and in-water data were collected using the two camera systems (DPOL and Sky-Cam). The Sky-Cam was placed near the end of the face boom on R/P FLIP (Fig. 5.1A) and the DPOL camera was deployed in the water under the Sky-Cam (Fig 5.1B) at various depths from near the surface to 70 meters. The choice of integration time for each image in the seawater varies from 3 ms to 1 s depending upon the spectral filter used, the brightness of the sky, and the instrument depth. At each DPOL measurement depth, five sequences of

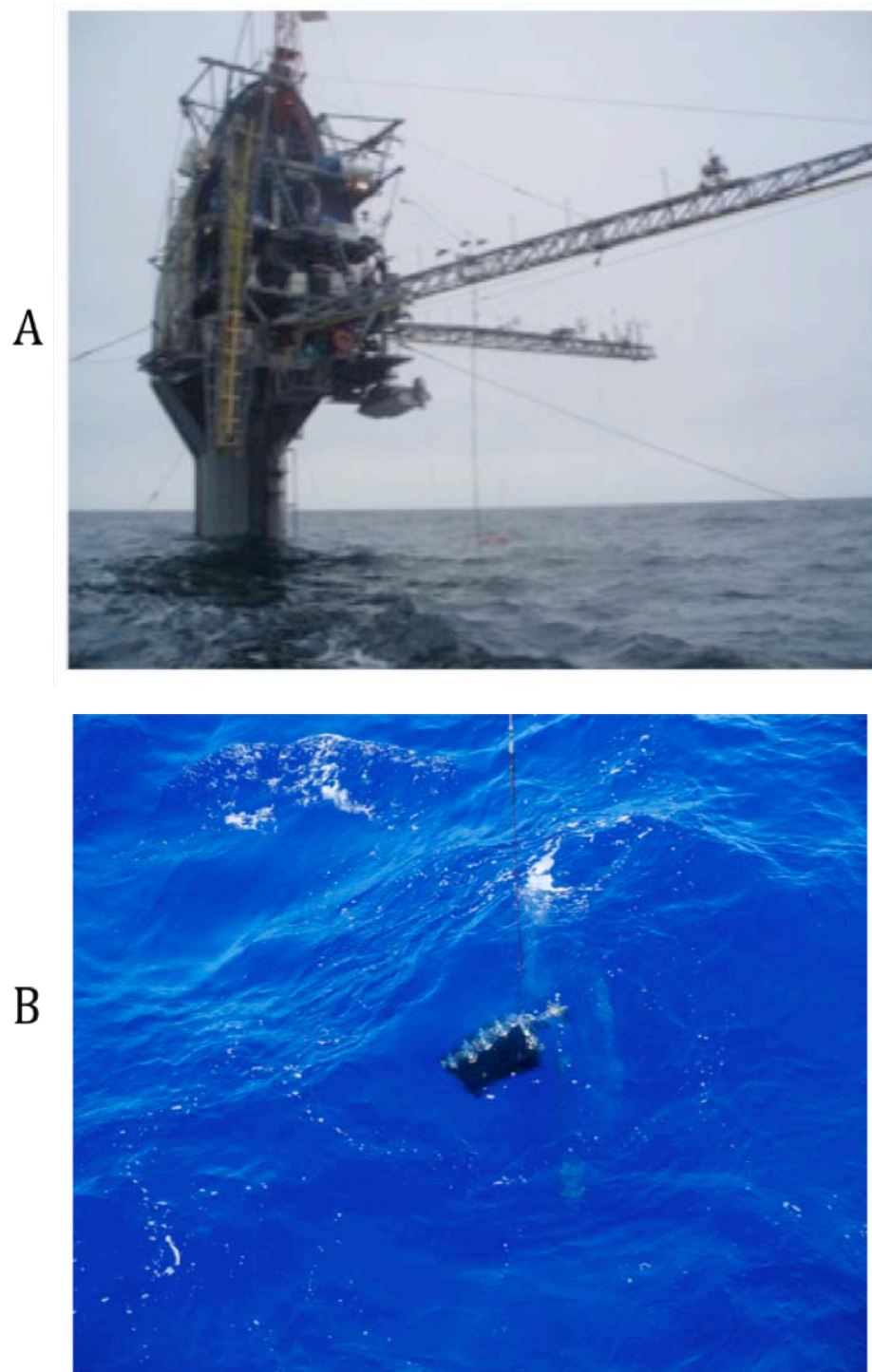


Fig. 5.1 (A) Picture of the R/P FLIP when it is flipped. Sky-Cam can be seen close to the end of the face boom. These booms are used to deploy the instruments in the water as well. (B) DPOL camera system while being deployed under the Sky-Cam.

images are obtained at each wavelength. In these sequences, dark images are collected for each of the integration time used. If we use all 7 spectral filters, it takes about 11 minutes to complete these 5 sequences. The images taken for each wavelength are then separated by approximately 140 seconds. Thus, with time required for data storage and changing the spectral filter, one frame can be collected every 17 s. Generally, at high solar zenith angles (SZA) (i.e. during sunset and sunrise), when the sky was not too bright, the DPOL measurements were done near the surface, and during low SZA the measurements were done at higher depths. During our measurements, there was no shadow of FLIP on the DPOL instrument as the boom used to deploy the instrument always faced towards sun.

There were also other collaborators who collected data from R/P FLIP and from another research vessel, R/V Kilo Moana, to study various characteristics of the ocean water (such as inherent optical properties, IOP's) and the atmosphere (such as aerosol optical depth, AOD). In this dissertation, I will also show their data when necessary.

## **5.2. Data Description**

For the DPOL data, the data reduction process includes the subtraction of the dark count image, correction for flat field response for the total optical system and camera lens/system rolloff, and calibration factors for absolute calibration and window immersion effects. The major portion of the data reduction is application of the transformation matrix which combines the four images obtained by the separate lenses into the 4 Stokes vector parameters, as described earlier. Angular calibration data is used to transform the native CCD resolution to a 180 x 180 pixel image. The final step is to

geometrically correct the image so that the image center is moved to the true zenith direction rather than a direction perpendicular to the instrument face. At deeper measurement depths, where the camera orientation did not change rapidly, I used a tilt-roll sensor built into the camera system to determine the absolute orientation of the system. At shallow measurement depths, when the instrument was suspended by a wire, there was more rapid movement of the instrument due to wave action on the instrument and supporting cable. At these depths I used the Snell's circle, obvious in the image, to re-center the image. I also rotated all images (both DPOL and Sky-Cam) to place the sun on the top of the figures. In all of the DPOL images the two semi-circular areas of missing data on the edge of the in-water images are portions of the images that have no data. These are areas obstructed by clamps which hold the glass dome windows on the instrument. They are arranged so that similar areas are obstructed on each lens, since all four images are required to obtain the Stokes vector for a specific direction.

In the fisheye format data images, the center represents the zenith, the edges represent the horizon ( $90^\circ$  zenith) and the zenith angle is directly proportional to the radius from the center. For DPOL (in-water) images, the white circle represents the boundary of the theoretical Snell's cone, determined by the critical angle.

Figure 5.2A is a sample raw fisheye image, 1600 x 1200 pixels, taken with the DPOL camera system at sea. In the 4 fisheye images, we can see the Snell's window and the surface waves effects. During the data reduction process, with the application of the calibration parameters, we transform these raw images into a linear array (Fig. 5.2B) so that each fisheye image is 180 x 180 pixels in size, and the radius is directly proportional to the zenith angle.

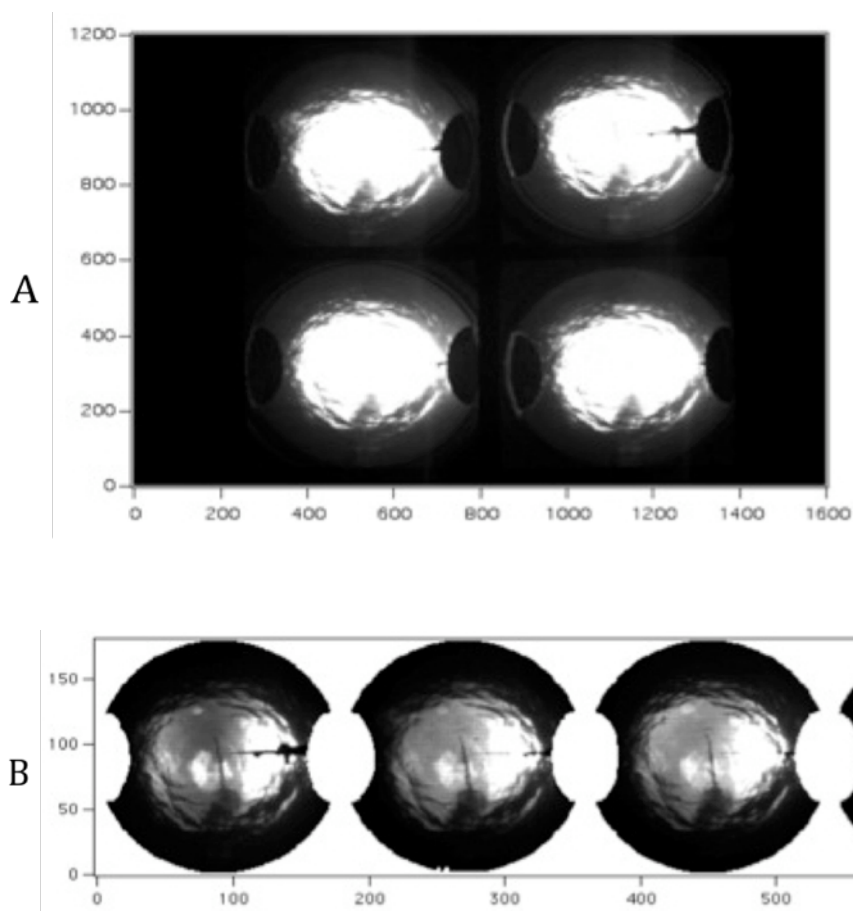


Fig. 5.2 (A) A sample of raw fisheye image (1600 x 1200 pixels) taken with the DPOL camera system. (B) Raw images transformed into a linear array after applying the calibration parameters. Each transformed fisheye image is 180 x 180 pixels in size, and the radius is directly proportional to the zenith angle.

### 5.3. IOP's and AOD Data

Table 5.1 and Fig. 5.3 show the inherent optical properties, IOP's (total absorption coefficient ( $a_t$ ), total scattering coefficient ( $b_t$ ) and total attenuation coefficient ( $c_t$ )) from SBC (September 21, 2008) and Hawaii (September 05, 2009). In Hawaii we will present DPOL data from both September 5 and 7, the IOP's on September 7 are very close to those shown for September 5. For SBC, since we do not have data on September 22, the date of our DPOL measurements, I have shown typical

data from September 21. The data in Table 5.1 for each wavelength corresponds to the average and the corresponding standard deviation (std) values from the surface to 30 m depth for SBC and to 50 m depth for Hawaii. Table 5.2 lists the average Aerosol Optical Depth (AOD) for the measurement period of the data presented in this dissertation. This data was collected using a Microtops Sunphotometer, and is also available through the Marine Aerosol Network

([http://aeronet.gsfc.nasa.gov/new\\_web/maritime\\_aerosol\\_network.html](http://aeronet.gsfc.nasa.gov/new_web/maritime_aerosol_network.html)).

Table 5.1 Coefficients for total absorption  $a_t(\lambda)$ , total scattering  $b_t(\lambda)$  and total attenuation  $c_t(\lambda)$  from the SBC and Hawaii experiments. For each wavelength, the average and the corresponding standard deviation (std) are shown for the data from the surface to 30 m depth for SBC and to 50 m depth for Hawaii.

Location and Date	$\lambda$ nm	$a_t \pm \text{std}$ $\text{m}^{-1}$	$b_t \pm \text{std}$ $\text{m}^{-1}$	$c_t \pm \text{std}$ $\text{m}^{-1}$
SBC Sept. 21, 2008	440	0.166±0.007	0.393±0.099	0.560±0.101
	488	0.127±0.006	0.393±0.095	0.521±0.097
	510	0.125±0.005	0.396±0.092	0.520±0.094
	532	0.124±0.004	0.388±0.090	0.512±0.091
	555	0.126±0.004	0.384±0.086	0.510±0.088
	650	0.388±0.004	0.328±0.073	0.716±0.076
Hawaii Sept. 05, 2009	488	0.022±0.001	0.056±0.004	0.078±0.004
	510	0.040±0.001	0.053±0.004	0.093±0.004
	532	0.049±0.001	0.053±0.003	0.102±0.004
	555	0.062±0.001	0.051±0.003	0.114±0.004
	650	0.341±0.001	0.046±0.003	0.0387±0.003

Table 5.2 Average Aerosol Optical Depth (AOD).

Date	AOD 380 nm	AOD 440 nm	AOD 500 nm	AOD 675 nm	AOD 870 nm
Sept. 22, 2008	0.23±0.02		0.16±0.02	0.11±0.02	0.09±0.13
Sept. 05, 2009	0.13±0.01	0.11±0.01	0.10±0.01	0.09±0.01	0.08±0.01
Sept. 07, 2009	0.29±0.05	0.27±0.04	0.25±0.04	0.19±0.02	0.14±0.02

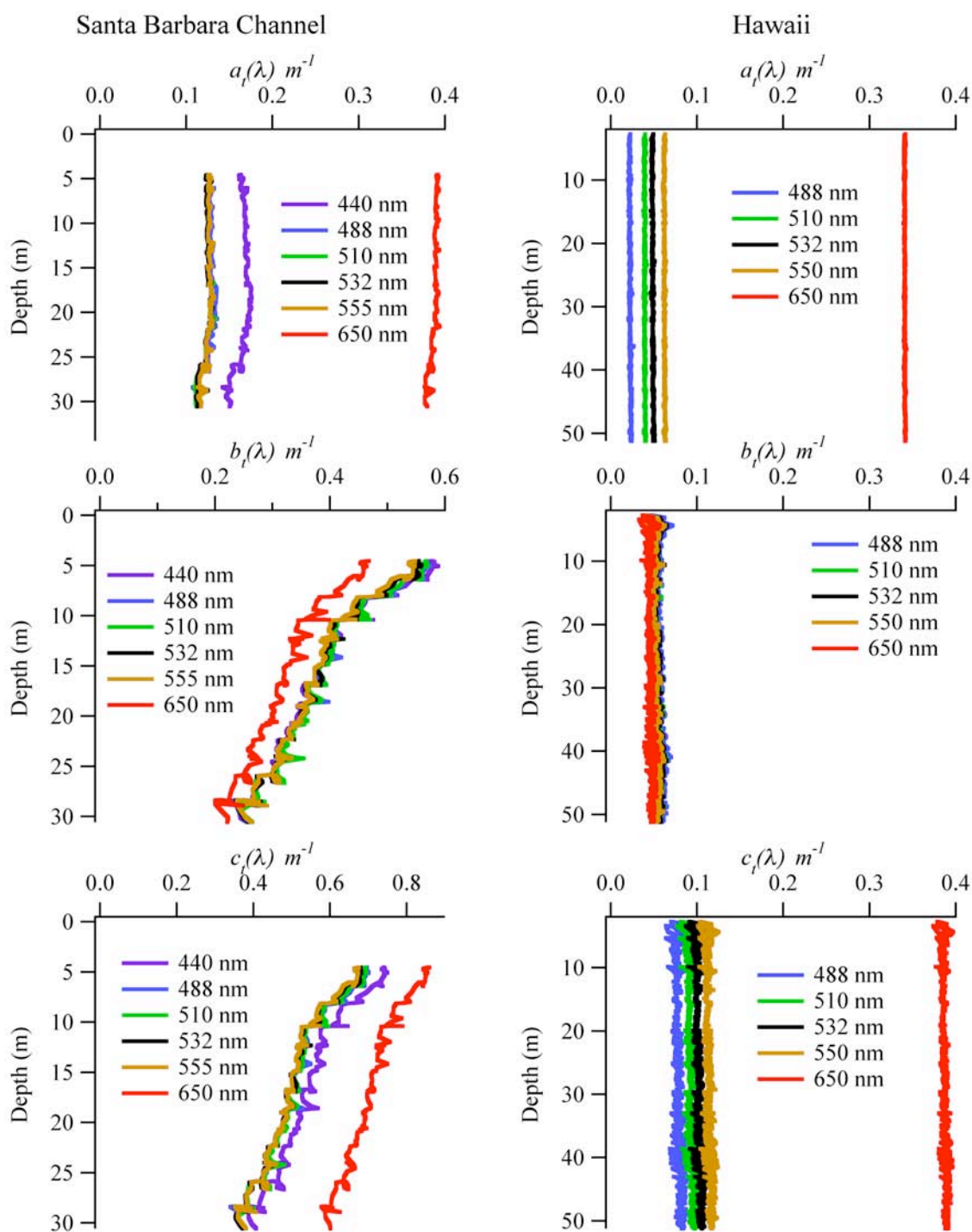


Fig. 5.3 Total absorption coefficient  $a_t(\lambda)$ , total scattering coefficient  $b_t(\lambda)$  and total attenuation coefficient  $c_t(\lambda)$  from SBC (September 21, 2008) and Hawaii (September 05, 2009).

## CHAPTER 6. DATA AND RESULTS

### 6.1. SBC Experiment

During the SBC experiment we confined our measurements to five wavelengths (442 nm, 488 nm, 520 nm, 550 nm and 589 nm). Thus, similar wavelength images are separated by approximately 97 seconds. At the measurement site, the water depth was 168 m. In Figs. 6.1-5, we show the variation of the downwelling radiance distribution, the normalized  $Q$  and  $U$ , the degree of linear polarization ( $DoLP$ ), and the angle of plane of polarization ( $\chi$ ) for the DPOL and Sky-Cam data from Santa Barbara channel (SBC) experiment on September 22, 2008.

Figure 6.1 shows the angular distribution of downwelling radiance as a function of depth for the in-water radiance distribution and the corresponding sky radiance distribution from the SBC experiment on September 22, 2008. I have selected data for various depths (1 m to 30 m) at a single wavelength, 520 nm. The graphs on the left, are the radiance distributions along the solar principal plane. Vertical lines at  $\pm 48^\circ$  correspond to the nominal edge of the Snell's circle, while the refracted solar zenith angle (SZA') is shown with an arrow on the horizontal axis. Positive zenith angles are towards the sun and negative are opposite the sun. The blue curves represent the sky data and the red curves the in-water data samples. The black curve is the average of in-water data samples. In the fisheye format images, which are 180 x 180 pixels and are in SI radiance units, the center represents the zenith, the edges represent the horizon ( $90^\circ$  zenith), and the zenith angle is directly proportional to the radius from the center. The first and the

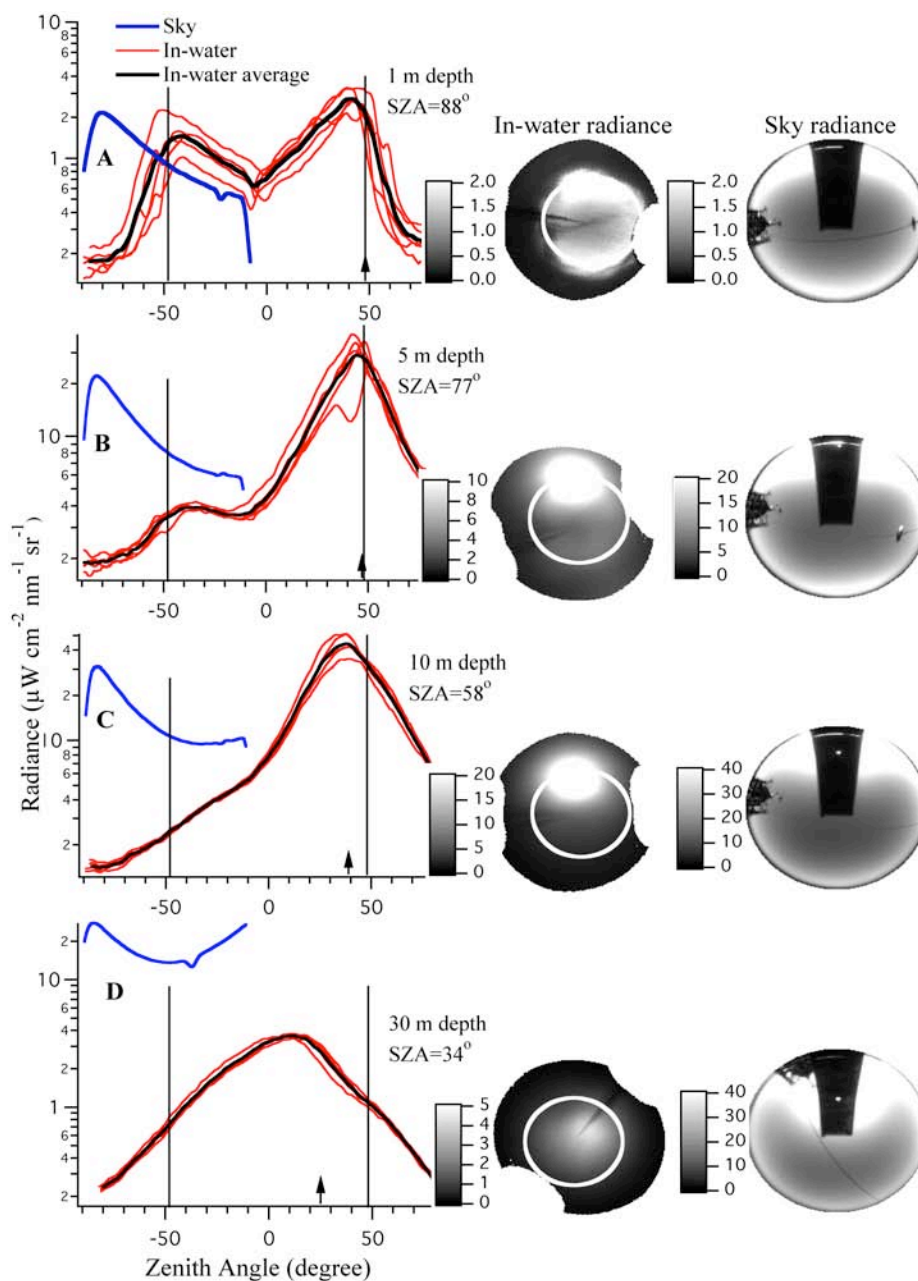


Fig. 6.1 Angular distribution of radiance as a function of depth from SBC experiment on September 22, 2008. Graphs are radiation distribution in solar principal plane. The first and second columns of fisheye images are the in-water and sky downwelling radiation distribution, respectively. All images have been rotated to place the sun on the top of the figures. In the graphs, positive zenith angles are towards the sun, negative values are away from the sun. Vertical lines at  $\pm 48^\circ$  correspond to edge of Snell's cone (white circle), while the refracted solar zenith angle ( $\text{SZ}'$ ) is shown with an arrow. A) 1 m depth,  $\text{SZ}'=88^\circ$  and  $\text{SZ}'$  (refracted)  $=48^\circ$ . B) 5 m depth,  $\text{SZ}'=77^\circ$ ,  $\text{SZ}'=47^\circ$ . C) 10 m depth,  $\text{SZ}'=58^\circ$ ,  $\text{SZ}'=39^\circ$ . D) 30 m depth,  $\text{SZ}'=34^\circ$ ,  $\text{SZ}'=25^\circ$ .

second columns of fisheye images represent the in-water and sky radiances respectively. In most of the in-water images, we can see the boom on FLIP from which the instrument is suspended and the cable (that supports the camera) as thick dark lines passing near the image center. The dark rectangular part on the top of sky images is the occulter used to block the lens from direct sunlight. The data lying in this area is not shown in the radiance graphs. Also evident in the sky images are the superstructure of FLIP, which is on the edge of the images, and support cables for the booms that pass above the camera.

Figure 6.1A is the data at 1 m depth and the corresponding sky. The solar zenith angle (SZA) is  $88^\circ$  and the refracted solar zenith angle (SZA') is  $48^\circ$ . These images were collected between 01:51 and 01:57 UTC on September 23, 2008 with an exposure time of 0.1 s. The sky is predominately clear, however there was a marine layer on the horizon and the sun is about to set. Wind speed is about 6 m/s, but there were almost no white caps. In the in-water images, we can see the sharp gradient in radiance at the theoretical Snell's cone boundaries (white circle). However, the Snell's cone moves along with the surface waves (Sabbah and Shashar, 2006) and the boundary of the Snell's cone is blurred by the surface waves with a unique shape determined by the local wave slope (You et al., 2009). In the principal plane, the graph of the in-water radiance (red and black curves), clearly show two peaks at the boundaries of the Snell's cone then a rapid drop of the radiance just outside the Snell's cone. The ratio of the two peaks is 1.9. While we do not have data for the sky radiance on the sun side of the horizon, we can look at the radiance to either side of the occulter, near the horizon. The ratio of this radiance to the radiance on the horizon opposite the sun is also about 2.0. Thus the relative size of these peaks is the result of the refraction of the sky radiance into the

water. At this depth and inside the Snell's circle, the radiance distribution is mainly due to the refracted skylight. The ratio of the radiance below the surface to that above the surface is 0.67. This is a result of offsetting factors of an increase in radiance due to the Snell's law and the  $n^2$  effect of the interface ( $n$  is the index of refraction), the water attenuation, and the reflectance of the surface at these large angles. The fluctuations between data sets can be large, and are due to the varying surface angles caused by surface waves. At this low sun angle, the direct solar beam does not appear in the subsurface radiance image. This is probably due to the high attenuation of the solar beam through the marine layer that was on the horizon.

In Fig. 6.1B I show the data at 5 m depth, collected between 00:50 and 00:57 UTC on September 23, 2008 with an exposure time of 0.1 s. The solar zenith angle (SZA) is  $77^\circ$  and the refracted solar zenith angle (SZA') is  $47^\circ$ . The sky and water surface conditions are similar to the previous case. In 6.1B, 6.1C, and 6.1D, the in-water image is the average of 5 data sets at that depth. At 5 m, the peak opposite to the sun is only 13% of the peak on the sun side. At the higher solar elevation, the sky radiance opposite the sun is much less than that on the sun side, hence the difference in the subsurface peaks. While the edge of the Snell's circle is evident, particularly on the side opposite the sun, it is not as sharply defined as at 1 m. There is only a factor of 2 between the radiance at  $-90^\circ$  and  $-48^\circ$ , versus a factor of 10 at 1 m.

In Fig. 6.1C I show the data at 10 m depth. The solar zenith angle (SZA) is  $58^\circ$  and the refracted solar zenith angle (SZA') is  $39^\circ$ . The images were collected between 23:15 and 23:22 UTC on September 22, 2008 with an exposure time of 0.1 s. The sky and water surface conditions are similar to previous cases. In this case there is no obvious

break in the radiance at the edge of the Snell's cone. The in-water radiance peak opposite to sun has disappeared. This is due to both scattering along the path to the surface at this angle, and the higher solar zenith angle, which decreases the brightening of the sky radiance on the horizon. One can also see the beginning of the radiance peak moving towards zenith from the refracted solar position. This effect has been seen earlier in studies by Tyler (1960) and Jerlov and Fukuda (1960).

In Fig. 6.1D I show the data at 30 m depth. The solar zenith angle (SZA) is  $34^\circ$  and the refracted solar zenith angle (SZA') is  $25^\circ$ . The images were collected between 19:45 and 19:52 UTC on September 22, 2008 with an exposure time of 0.3 s. The wind speed was about 3 m/s and the water is very calm. At this depth, the edge of the Snell's cone has completely disappeared, and the radiance peak has shifted significantly (about  $15^\circ$ ) towards the center from the refracted solar position. Moreover, at this depth the individual data sets are very similar, as shown in the radiance plot. This is a combination of the effects of scattering, smoothing out the variations, and greater surface averaging, since a  $1^\circ$  by  $1^\circ$  data point is sampling a much larger area on the surface (increases as the square of the depth). The radiance distribution is also much more symmetric around its peak value.

In Fig. 6.2, I show  $Q/I$  and  $U/I$  for both DPOL and Sky-Cam measurements (values vary from -1 to 1). The images in the first and second column are the in-water data, while the third and the fourth columns are the sky data shown in Fig. 6.1. In Fig. 6.2A and at 1 m, the sky  $Q/I$  and  $U/I$  patterns have been refracted into the in-water Snell's cone. In these figures, the minimum (-1) and the maximum (+1) of  $Q/I$  (or  $U/I$ ) are at right angles with each other. The minimum of  $Q/I$  lies along the solar principal

plane, where the r-component of the E-field is predominant (Eq. 2.4b).  $U/I$  is 0 (i.e.,  $I_{45} = I_{-45}$ ) where  $Q/I$  has either maximum or minimum values. The magnitude of  $Q/I$  and  $U/I$  is larger on the side opposite of the sun.

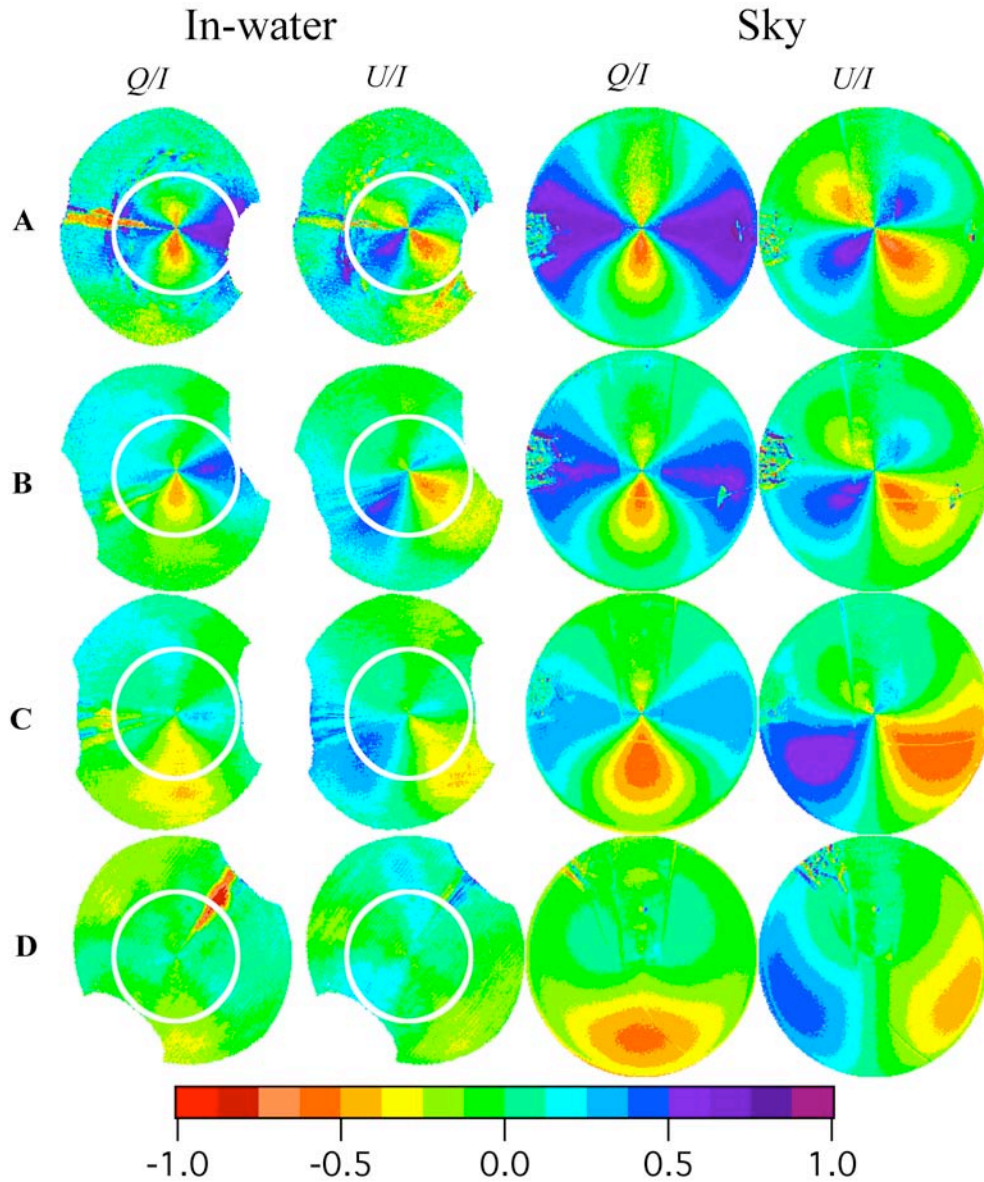


Fig. 6.2 Angular distribution of  $Q/I$  and  $U/I$  at several depths from the SBC experiment on September 22, 2008. The first two columns of images correspond to in-water and the last two columns correspond to sky data. The white circle corresponds to the boundary of Snell's cone. Data corresponds to images shown in Fig. 6.1.

The sky images show the effect of the changing solar zenith angle, with the increase in the area of negative  $Q/I$ , and decrease in the area of positive  $Q/I$ . Similarly the maximum value of  $U/I$  first increases then starts to decrease. In the water, the pattern inside the Snell's circle at shallow depths reflects the sky polarization pattern. However at greater depths, the polarization pattern inside the Snell's circle is muted. At shallow depths, there is a large discontinuity in the polarization pattern at the edge of the Snell's circle, while by 10 m (Fig. 6.2C) there is no obvious change in the pattern at the edge of the Snell's circle.

Figure 6.3 shows the angular distribution of the degree of linear polarization ( $DoLP$ ) as a function of depth for water and sky, for the cases shown in Figs. 6.1 and 6.2. The plots show the variation of  $DoLP$  along the solar principal plane. At 1 m (Fig. 6.3A), there are two polarization patterns, one within the Snell's cone and the other outside it (Waterman, 1954). The polarization within the Snell's cone arises due to the refracted skylight. The polarization outside the Snell's cone arises from scattering and internal reflections of light field (Ivanoff, 1974). At 1 m depth (Fig. 6.3A) most of the polarization behavior is confined within the Snell's cone and is similar to sky pattern. At this depth, the maximum  $DoLP$  is similar to that in the sky, approximately 65%. This maximum occurs at a scattering angle of  $90^\circ$  in the sky, due to Rayleigh scattering (Coulson, 1988), and  $100^\circ$  in oceanic scattering (Voss and Fry, 1984). Because each lens is separated by 11 cm in the DPOL system, when only 1 m from the surface, each camera sees a slightly different area of the surface within a  $1^\circ \times 1^\circ$  pixel. Hence in areas of rapid change (the Snell's circle), this can lead to more noise/error in the polarization calculation. By 5 m (Fig. 6.3B) this is no longer an important factor. In addition, the

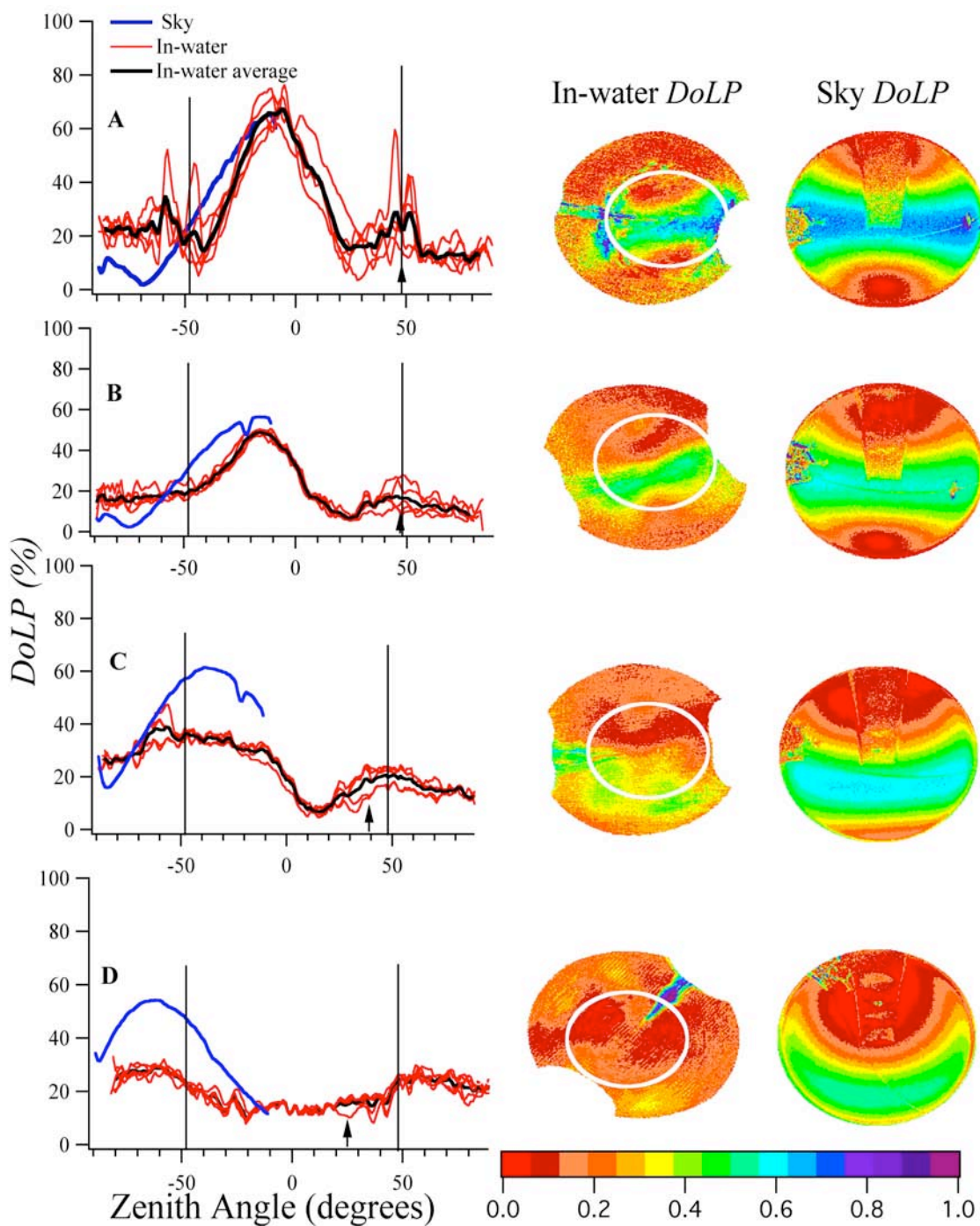


Fig. 6.3 Angular distribution of  $DoLP$  for data shown in Figs. 6.1 and 6.2. Graphs show the  $DoLP$  along the solar principal plane. The first and second columns of images correspond to in-water and sky data respectively.

surface waves (Maximov, 2000) and scattering of light (Shashar et al., 2004) also cause certain distortions of the polarization within the Snell's cone. Outside the Snell's cone, the internal reflections of light off the dynamic water surface increase the variations in the radiance field (Sabbah and Shashar, 2006). Furthermore, the Snell's cone can also move along with the motion of the surface waves (see video associated with You et al., 2011). Because of these reasons, we can see two small peaks in the *DoLP* data near the Snell's boundary (Fig. 6.3 A). As the depth of water increases, the polarization also extends outside the Snell's cone, while the *DoLP* decreases. At 5 m depth (Fig. 6.3B), the maximum *DoLP* is about 45%, which is still close to the 58% in the sky. At 10 m depth (Fig. 6.3C), the maximum *DoLP* is about 35%, which is significantly less than the 60% in the sky, indicating that scattering in the water has significantly modified the polarization pattern. In addition the maximum polarization is now nearly  $100^\circ$  from the refracted solar position. This is now indicative of the polarization pattern due to scattering in the water, as opposed to the refracted skylight polarization pattern. At 30 m depth (Fig. 6.3D), the polarization behavior is mainly outside the Snell's circle at an in-water scattering angle of  $100^\circ$  also showing that light scattering in the water has dominated the refracted skylight. In this case, the maximum *DoLP* is about 28%, which is about half that in the corresponding sky (55%).

In Fig. 6.4, we can see the variation of angle of plane of polarization ( $\chi$ ) in different planes for the data shown in Figs. 6.1, 6.2, and 6.3. The angle  $\chi$  is defined according to Eq. 2.7. The plots show  $\chi$  for water (red curve) and for the corresponding sky (blue curve) along an almucanter at  $27^\circ$  in air and the corresponding almucanter at  $20^\circ$ , due to refraction, in water. The data are shown for angles between  $90^\circ$  to  $270^\circ$  from

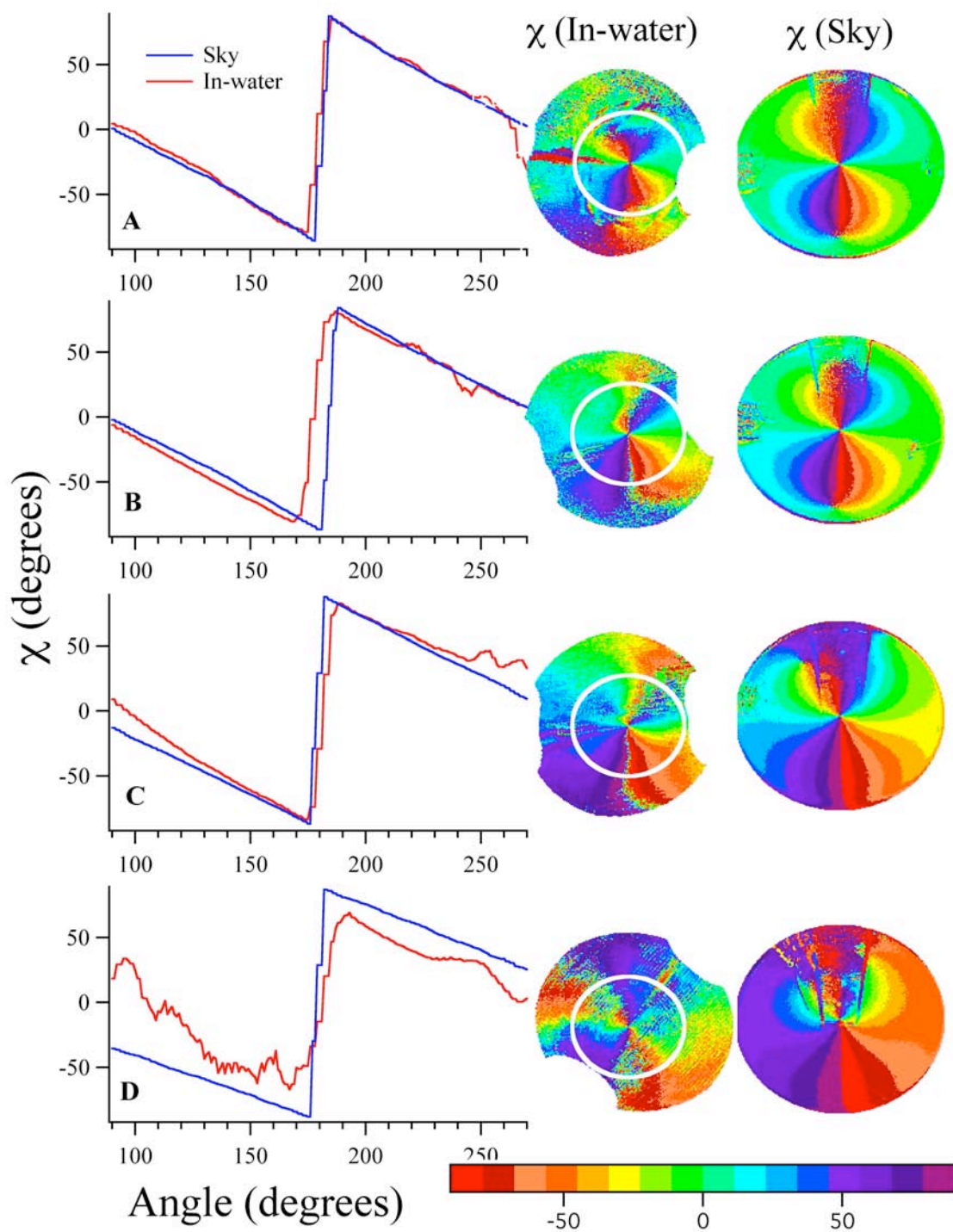


Fig. 6.4 Variation of  $\chi$  for data shown in Figs. 6.1, 6.2, and 6.3. The plot shows  $\chi$  for water (red curve) and for the corresponding sky (blue curve) along an almucanter at  $27^\circ$  in air and the corresponding almucanter at  $20^\circ$ , due to refraction, in water. The first column of the image represents the in-water data and the second column represents the sky data.

the sun along clockwise direction. It is seen from these figures and graph that  $\chi$  is about  $0^\circ$  (i.e., the E-vector of polarization is along the meridian plane) in azimuths  $90^\circ$  to the principal plane, then increases (or decreases) to  $90^\circ$  (or  $-90^\circ$ ) on either side of the principal plane. The principal plane is a line of discontinuity. It has been hypothesized that this plane of polarization is the most stable and predictable parameter even under a wide range of atmospheric variations (Brines and Gould, 1982; Pust and Shaw, 2008) and is used by animals in the water for navigation (Horvath and Varju, 2004; Waterman, 2006). Similar to the case of  $Q/I$  and normalized  $U/I$  (Fig 6.2), at shallow depths, there is a large discontinuity in the polarization pattern at the edge of the Snell's circle (Fig 6.4A, 1 m depth), while by 5 m (Fig. 6.4B) the  $\chi$  pattern is continuous inside and outside the Snell's boundary. Moreover, it is seen from Fig. 6.4 that the  $\chi$  pattern is more stable along the solar principal plane than in a plane perpendicular to the principal plane in both in-water and sky images. In Fig 6.2, we have seen that the  $Q/I$  and  $U/I$  pattern change with the solar zenith angle. Because of this effect, particularly in the sky images, the  $\chi$  pattern along a plane perpendicular to the solar principal plane is changing with the change in the solar zenith angle.

Figure 6.5 displays the angular variation of downwelling radiance and  $DoLP$  with  $\lambda$  at 1 m and 30 m depths. In this result I have not used 410 nm and 650 nm wavelengths as they were out of focus during the calibration process. The data for 520 nm is the same as discussed above, with corresponding environmental conditions. The first column of graphs (Figs. 6.5A, 6.5C, 6.5E and 6.5G) are in-water data and the second column (Figs. 6.5B, 6.5D, 6.5F and 6.5H) are sky data. Figures 6.5A, and 6.5E are at 1 m depth and Figs. 6.5C and 6.5G are at 30 m depth. Five data sets were averaged for each in-water

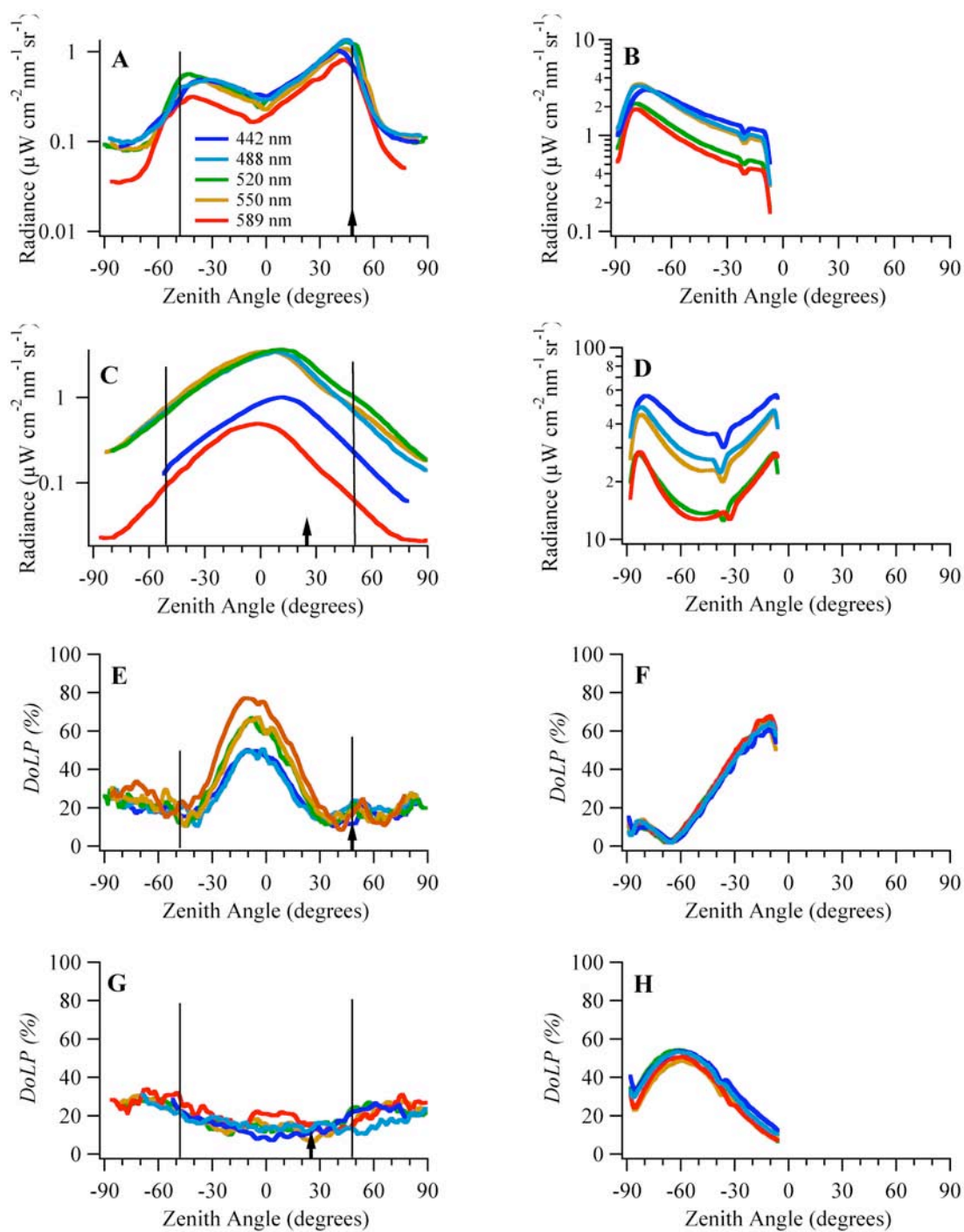


Fig. 6.5 Angular variation of downwelling radiance and *DoLP* with wavelength at 1 m and 30 m depths. The first column of graphs (Figs. 6.5A, 6.5C, 6.5E and 6.5G) is in-water data and the second column (Figs. 6.5B, 6.5D, 6.5F, and 6.5H) is the sky. Figures 6.5A, 6.5E are for 1 m depth (and SZA=88°) and Figs. 6.5C and 6.5G are for 30 m depth (and SZA=34°). Five data sets were averaged for each in-water measurement shown.

measurement shown. In Figs. 6.5B and 6.5D the clear, unsurprising, trend is that the sky radiance is highest at the short wavelengths, decreasing at large wavelengths. Interestingly in Fig. 6.5A it can be seen that all the radiances, except for the longest wavelength, are quite similar. In Fig. 6.5C, at 30 m, the effect of the greater absorption at 442 nm and 589 nm (seen in Table 5.1 and Fig. 5.3) has caused these radiances to decrease significantly with respect to the other wavelengths. Also interestingly, the large attenuation at 589 nm has caused this radiance distribution to become basically symmetric around the zenith direction, as is predicted for an asymptotic radiance distribution (Shuleikin, 1933; Timofeeva, 1974). At 589 nm, 30 m represents over 17 attenuation lengths.

The *DoLP* of the sky has almost no wavelength dependence (Figs. 6.5F and 6.5H). However in the water, at shallow depths, the *DoLP* is much larger for the longer wavelengths (Fig. 6.5E) than the shorter wavelengths. This could be expected if the single scattering albedo was higher in the blue wavelengths than red, however the IOP data does not reflect this, except for the longest wavelength. The *DoLP* will also depend on the color of the water mass concerned (Ivanoff and Waterman, 1954). The downwelling light field combines the direct refracted skylight as well as the light that is incident onto the surface from below the water and is reflected downward. This reflected light will cause a depolarization of light field, and depends on the absorption and scattering coefficients of the medium. As can be seen in Fig 6.5A, by looking at the ratio of the radiance on the edge of the Snell's cone to that outside the Snell's cone, one can see that there is more upwelling light in the shorter wavelengths than the red wavelength. So this depolarization may be in part due to the upwelling light field. Another source of

depolarization is scattered skylight. Since the skylight makes up a much larger portion of the total incoming irradiance in the blue wavelengths than the red wavelengths, the radiance scattered into a particular direction (the path radiance) due to skylight will be a larger depolarization factor in the blue than the red. With the high scattering coefficient in this data set, this could be an important contribution to the depolarization. At 30 m (Fig. 6.5G), the in-water light field polarization is basically spectrally independent, and has a maximum at 90-100 degrees from the refracted solar direction as expected for water scattering.

## 6.2. Hawaii Experiment

I will be presenting data collected on September 05 and 07, 2009. The sky was predominantly clear during these measurements. The water IOP's are shown in Table 5.1 and Fig. 5.3. The water depth during the Hawaii experiment was approximately 5000 m.

Many of the features of our data during the Hawaii experiment are similar to the SBC experiment, with differences reflecting the increased water clarity. Additionally, during the Hawaii experiment the winds were generally stronger, generating higher sea states and more whitecaps. This caused much more variation in the individual downwelling images for a given depth, particularly near the surface.

In Figs 6.6-9, I show the angular variation of the downwelling radiance distribution,  $Q/I$  and  $U/I$ , the degree of linear polarization ( $DoLP$ ), and the variation of the radiance and  $DoLP$  with wavelength and depth for in-water (4 m to 50 m depths) and the sky. Each image shown below is one of the 5 images in a sequence.

Figure 6.6 presents the angular distribution of downwelling radiance for the in-water data and the corresponding sky data. As in Fig 6.1, the first column of images corresponds to the in-water data and the second column corresponds to sky data. In Fig. 6.6A the angular variation of the downwelling radiance distribution at 4 m depth at 520 nm wavelength is shown. The data were collected around 3:30 (UTC, September 08, 2009) with an integration time of 0.1 sec, and  $SZA=75^\circ$ . The latitude is  $17.54^\circ$  N and the longitude is  $157.68^\circ$  W. The sky is almost clear and the wind speed is about 6 m/s. In the image the boom and the cable supporting the camera pass almost vertically through the image center. In general the features are similar to the SBC case. However, because of the higher wind and wave conditions, more white caps, and clarity of the Hawaiian water, there are some differences in the case of the in-water data. The in-water radiance in Fig. 6.6A shows dark bands at the edge of the Snell's cone, resulting from the passage of a larger wave. On the upper part of the in-water image the white line that passes almost horizontally through the edge of white circle is caused by multiple reflections of light within the camera system, which is more significant near the surface when sun is very bright, often with a radiance over 4 orders of magnitude greater than the neighboring pixels. In the in-water radiance image, we can see a very well defined edge to the Snell's cone well within the white circle, much more distinct than in the SBC case (Fig. 6.1B) at a similar depth. In the graph of the principal plane in Fig. 6.6A there are clearly two radiance peaks around the Snell's cone, which fall off rapidly just beyond the Snell's boundary.

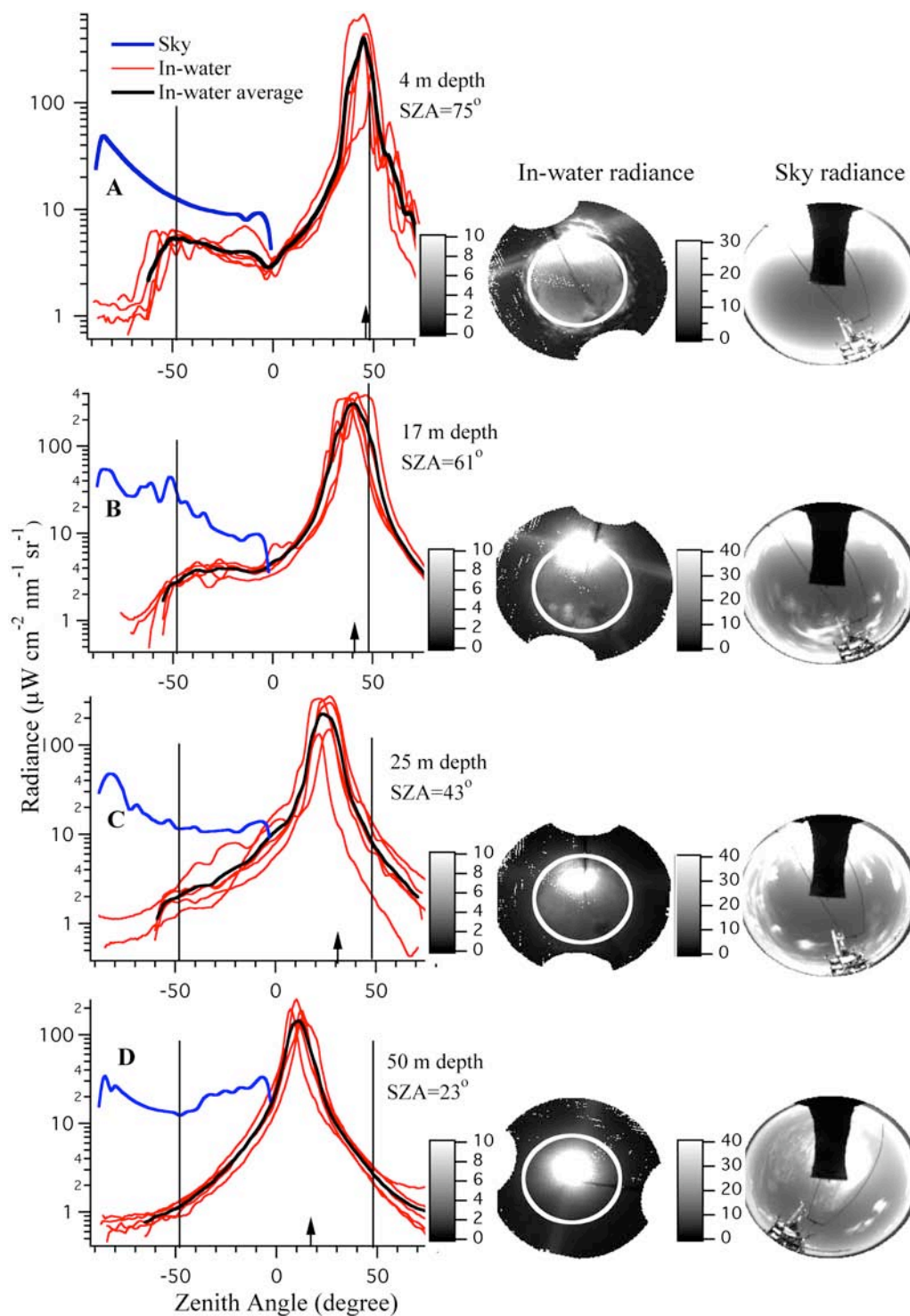


Fig. 6.6 Angular distribution of radiance as a function of depth during Hawaii experiment on September 05 (Figs. 6.6B, C, and D) and September 07 (Fig. 6.6A), 2009. Graphs are radiation distribution in the solar principal plane. The description of figures and graphs are similar to that of SBC experiment (Fig. 6.1). A) 4 m depth,  $SZA=75^\circ$  and  $SZA'=46^\circ$ . B) 17 m depth,  $SZA=61^\circ$ ,  $SZA'=41^\circ$ . C) 25 m depth,  $SZA=43^\circ$ ,  $SZA'=31^\circ$ . D) 50 m depth,  $SZA=23^\circ$ ,  $SZA'=17^\circ$ .

In Figs. 6.6B, 6.6C and 6.6D I show the results from September 05 2009 at 520 nm wavelength, a day with nearly the same water IOP's, and a mostly clear sky. The latitude and the longitude of the measurement site are  $17.54^{\circ}$  N and  $157.11^{\circ}$  W respectively. The sky was very clear throughout the day and the wind speed ranged from 6 to 8 m/s from morning to evening. In Fig 6.6B, we show the radiance distribution at 17 m depth. The data was collected around 02:30 (UTC, September 06, 2009) with the integration time of 0.02 sec. The SZA is  $61^{\circ}$ . There were some clouds, which can be seen in both in-water and sky radiance images. At this depth, there is a clearly defined Snell's cone and there are two radiance peaks, as opposed to SBC, where, by 10 m, the edge of the Snell's cone, and the peak opposite the sun was not significant (Fig. 6.1C). It is also noted from the graph that the in-water radiance peak towards the sun coincides with the refracted SZA, while in the SBC data the peak has shifted slightly towards the center even at 10 m depth.

In Fig. 6.6C, I show the result at 25 m depth. The data were collected around 01:15 (UTC, September 06, 2009) using an integration time of 0.02 sec. The SZA is  $43^{\circ}$ . During the measurement, there were some clouds and some white caps. The wind speed is about 8 m/s. There is no presence of an in-water radiance peak opposite the sun and the peak on the sun side is shifted towards the center by about  $5^{\circ}$  from the refracted solar position. In most of the 5 in-water images, the images of the cable (supporting the camera) and the support boom lie along the solar principal plane, which causes variation in the radiance plots (Fig. 6.6C). The edge of the Snell's cone is now not clearly defined on either side of the principal plane.

In Fig. 6.6D, I show the results at 50 m depth at solar zenith angle of about  $23^\circ$ . The data were collected on September 05, 2009 around 23:45 (UTC) with an integration time of 0.2 sec. There were a few white clouds and white caps during the measurement. The wind speed was about 7 m/s. At this depth, the 5 in-water principal plane measurements were quite consistent, the small scale features on the surface are no longer important. The radiance distribution is symmetric around the peak with no significant radiance peak at either edge of the Snell's cone. The peak on the sun side has shifted by about  $7^\circ$  towards the center from the refracted solar position. In the case of the SBC experiment at 30 m depth, this shift was almost double:  $15^\circ$ .

In Fig. 6.7, I show the angular variation of  $Q/I$  and  $U/I$  for in-water and sky for the data shown in Fig. 6.6. Basically, these are similar to the SBC experiment. The polarization behavior is confined within the Snell's cone at shallow depths (4 m, Fig. 6.7A) and at greater depths, it starts extending outside the Snell's cone (white circle). At 50 m depth, most of the polarization behavior is outside the Snell's cone. The transition between the polarization dominated by the sky, and that dominated by the water occurs between 17 m and 25 m, the same depths where the Snell's cone has become less distinct as shown in Figs. 6.6B and 6.6C.

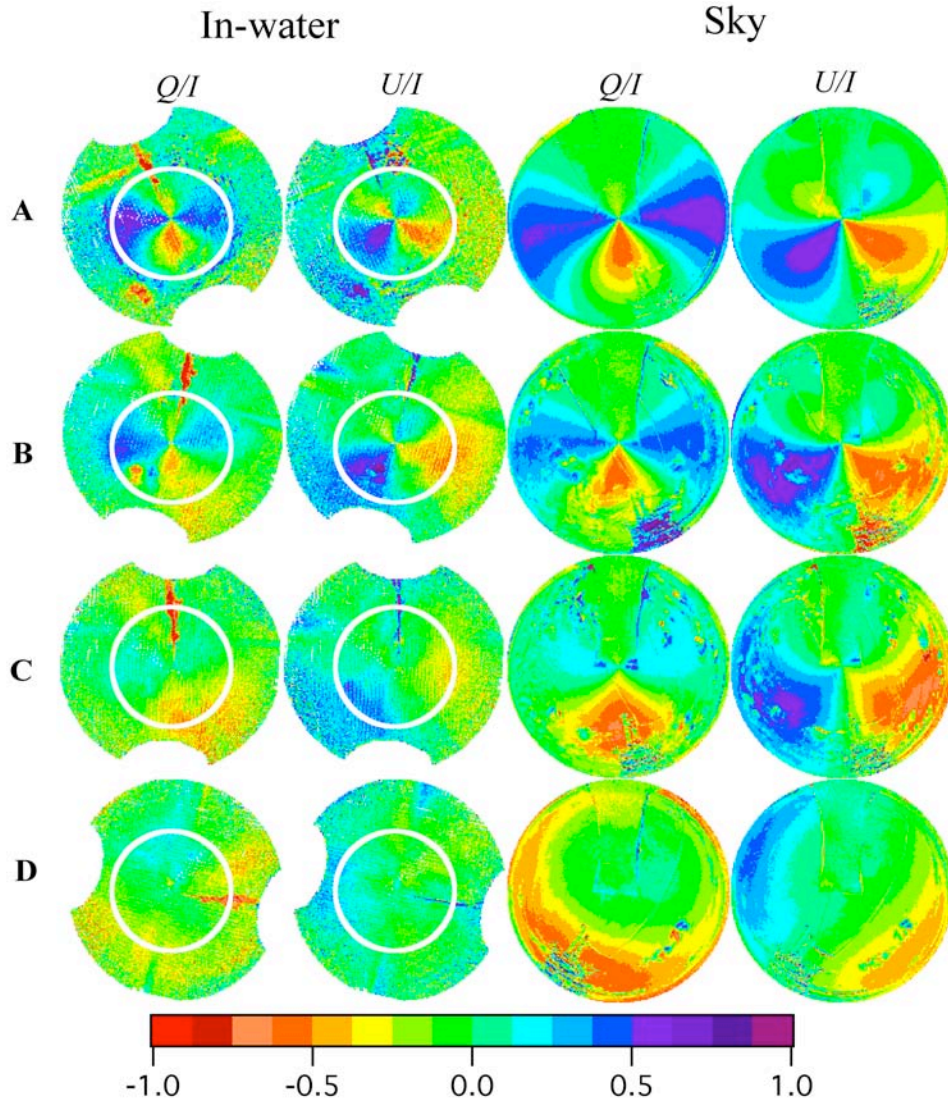


Fig. 6.7 Angular distribution of  $Q/I$  and  $U/I$  at several depths during the Hawaii experiments on September 05 and 07, 2009. The first two columns of images correspond to in-water and the last two columns correspond to sky data. The white circle corresponds to the boundary of Snell's cone. Data corresponds to images shown in Fig. 6.6.

In Fig. 6.8, I show the angular distribution of the  $DoLP$  for in-water and the corresponding sky for the data shown in Fig. 6.6 and 6.7. At 4 m depth (Fig. 6.8A), the distribution of polarization inside the Snell's cone is similar to that of the corresponding sky. The maximum polarization is about 60% and occurs at  $90^\circ$  scattering angle in the

sky (with appropriate refracted angle in the water). The in-water peaks around the Snell's boundary on the principal plane opposite the sun are due to the camera lens separation. With this separation, and so close to the surface, each lens views a slightly different portion of the surface at the same angle. When the light field is changing rapidly this can lead to errors in co-registering data. The even higher peak on the sun side is caused by the cable that supports the camera, coming in and out of view of the individual lenses. The fluctuation, around  $10^\circ$  zenith angle, of several of the in-water *DoLP* measurements is caused by the image of the supporting boom that passes through the center of the image. At 17 m depth (Fig. 6.8B), the maximum *DoLP* has decreased to about 40%, as opposed to 60% in the corresponding sky. The small peaks around the Snell's cone boundary are due to the reason described above. At 25 m depth (Fig. 6.8C), the images of the support cable and the boom lie along the solar principal plane above  $30^\circ$  zenith angle in most of the in-water data, and the effect of this can be seen in the graph. The maximum, non artifact, *DoLP* at this depth is about 38%, also less than the 65% in the corresponding sky. It has also shifted to a  $90^\circ$  scattering angle in water, rather than the refracted  $90^\circ$  scattering angle in air. This is much larger than the SBC case at 30 m (Fig. 6.3D), and nearly the same as the 10 m case in SBC (Fig. 6.3C). At 50 m depth (Fig. 6.8D), the polarization is seen to have extended well outside the Snell's cone and is still approximately 30%.

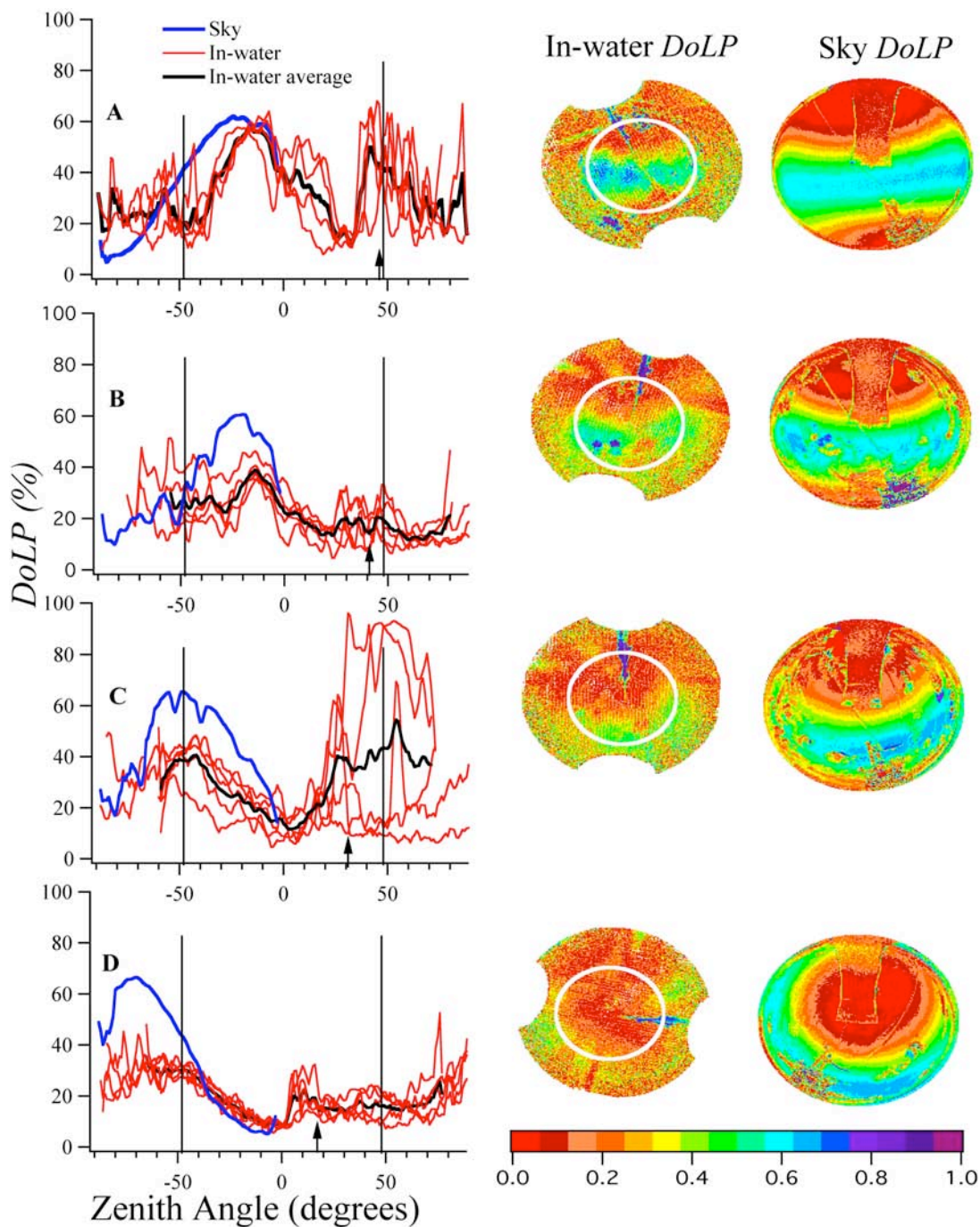


Fig. 6.8 Angular distribution of  $DoLP$  for data shown in Figs. 6.6 and 6.7. Graphs show the  $DoLP$  along the solar principal plane. The first and second columns of images correspond to in-water and sky data respectively.

In Fig. 6.9, we show the angular variation of the downwelling radiance and polarization with wavelength and depth for the Hawaii data. The data shown are averages over the 5 images collected at each depth and wavelength. We have shown 4 m and 50 m depths corresponding to the 520 nm dataset that has been presented above. The spectral variation of the radiance data is similar to that seen in the SBC case. Since we did not have sky data on 442 nm wavelength, it is not shown in the result.

What is interesting though, is that in this clearer water at the shallow depth, the *DoLP* seems to be spectrally independent, without the large wavelength dependence seen in SBC. In this clear water at shallow depths, path radiance from skylight would be a much smaller factor, so the *DoLP* would be predominately determined by the polarization of the skylight above the surface. Since this skylight polarization is spectrally independent, the water polarization is also spectrally independent. At larger depths (Fig. 6.9G), the polarization is also spectrally independent, as seen in the SBC data, indicating that the polarization matrix for scattering in the water, measured only at one wavelength by Voss and Fry (1984), is probably independent of wavelength.

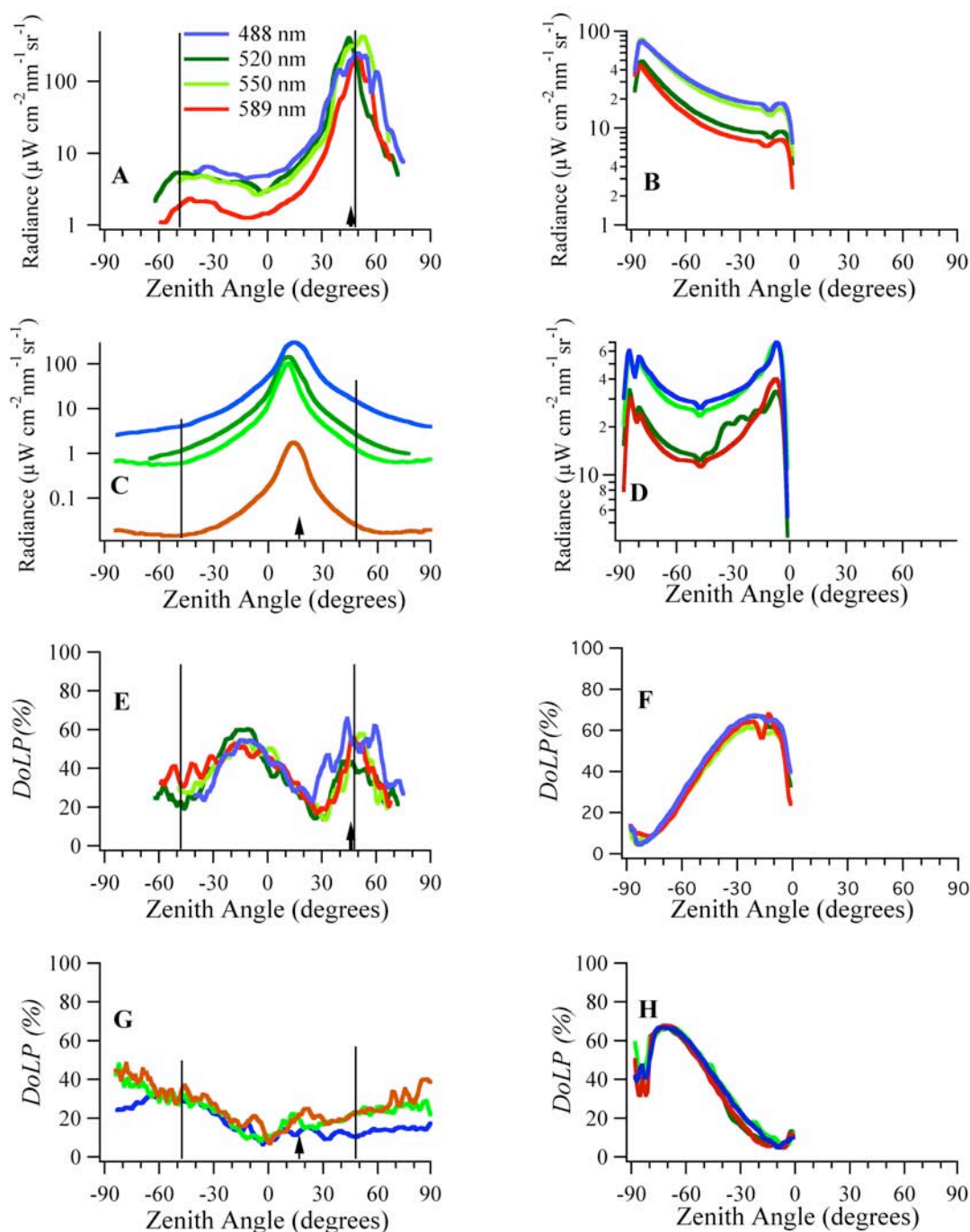


Fig. 6.9 Angular variation of downwelling radiance and the *DoLP* with wavelength at 4 m and 50 m depths. The first column of graphs (Figs. 6.9A, 6.9C, 6.9E, and 6.9G) is for in-water data and the second column (Figs. 6.9B, 6.9D, 6.9F, and 6.9H) for the sky. Figures 6.9A, and 6.9E are for 4 m depth (and  $SAZ=75^\circ$ ), and Figs. 6.9C and 6.9G are for 50 m depth (and  $SAZ=23^\circ$ ). Five data sets were averaged for each in-water measurement shown.

## CHAPTER 7. CLOUDLIGHT AND ELLIPTICAL POLARIZATION

### 7.1. Cloudlight Polarization

The polarization due to cloudlight (i.e. light originating from an area of the sky covered by clouds) can be assumed to have three components (Horvath and Varju, 2004; Pust and Shaw, 2008):

1. Originating from the Mie scattering of light by the cloud particles (crystals or water droplets) itself. The polarization due to this component is caused by both the single and multiple scattered light. The single scattered component can be polarized either perpendicular or parallel to the scattering plane (the plane containing the sun, the scattering object, and the observer)- depending upon cloud parameters such as drop size and cloud optical depth. Polarization in cloudlight arises from single scattering while multiple scattering primarily reduces the polarization. However, the  $\chi$  patterns of both single and multiple scattered light are the same (Kattawar and Plass, 1972).
2. Originating from Rayleigh scattering of light within the air column between the cloud and the observer. This light is polarized perpendicular to the scattering plane.
3. Originating from Rayleigh scattering of light from the air column above the cloud and is polarized perpendicular to the scattering plane. For a thick cloud layer, this component can be neglected.

In general, the first component dominates as its intensity is much higher than that of the second or third. However, the intensity and the *DoP* of cloudlight depend upon the type (particle size, density, composition etc.) and thickness of the clouds. Darker and thicker clouds decrease the radiance and the polarization of light. In a partly cloudy sky, under thin cloud or fog, the radiance and the *DoP* has a much lower value (the maximum value of *DoP* reaches about 40% at 90 degrees from the sun, Konnen, 1985) than the clear sky because of the randomizing effect of the multiple scattering, whereas the  $\chi$  pattern is similar to that of the clear sky. It is believed that  $\chi$  is the most stable and predictable parameter under a wide range of atmospheric variations (Brines and Gould, 1982; Pust and Shaw, 2008) and this is the reason that  $\chi$  is used as an orientation cue by animals (Auburn and Taylor, 1979; Horvath and Varju, 2004). On the other hand, under a heavily overcast sky, when the cloud layer is several km thick, the *DoP* of cloudlight is strongly reduced. In such conditions, light coming from the zenith has a shorter path length through the cloud and will have more intensity than the light coming from the horizon. In this situation, the cloudlight is horizontally polarized just above the horizon where the *DoP* can reach about 10-20%, and it decreases rapidly to 0% towards the zenith (Konnen, 1985). However, the decrease in *DoP* due to multiple scattering of light in the longer path length should also be taken into account. If the *DoP* drops to 0%, the  $\chi$  pattern is obviously lost.

As an example of this situation in our data, Fig. 7.1 shows the fisheye images of the radiance, *Q/I* and *U/I*, *DoLP* and the  $\chi$  for the DPOL and Sky-Cam during a cloudy day. The data shown corresponds to 520 nm wavelength and were taken at around

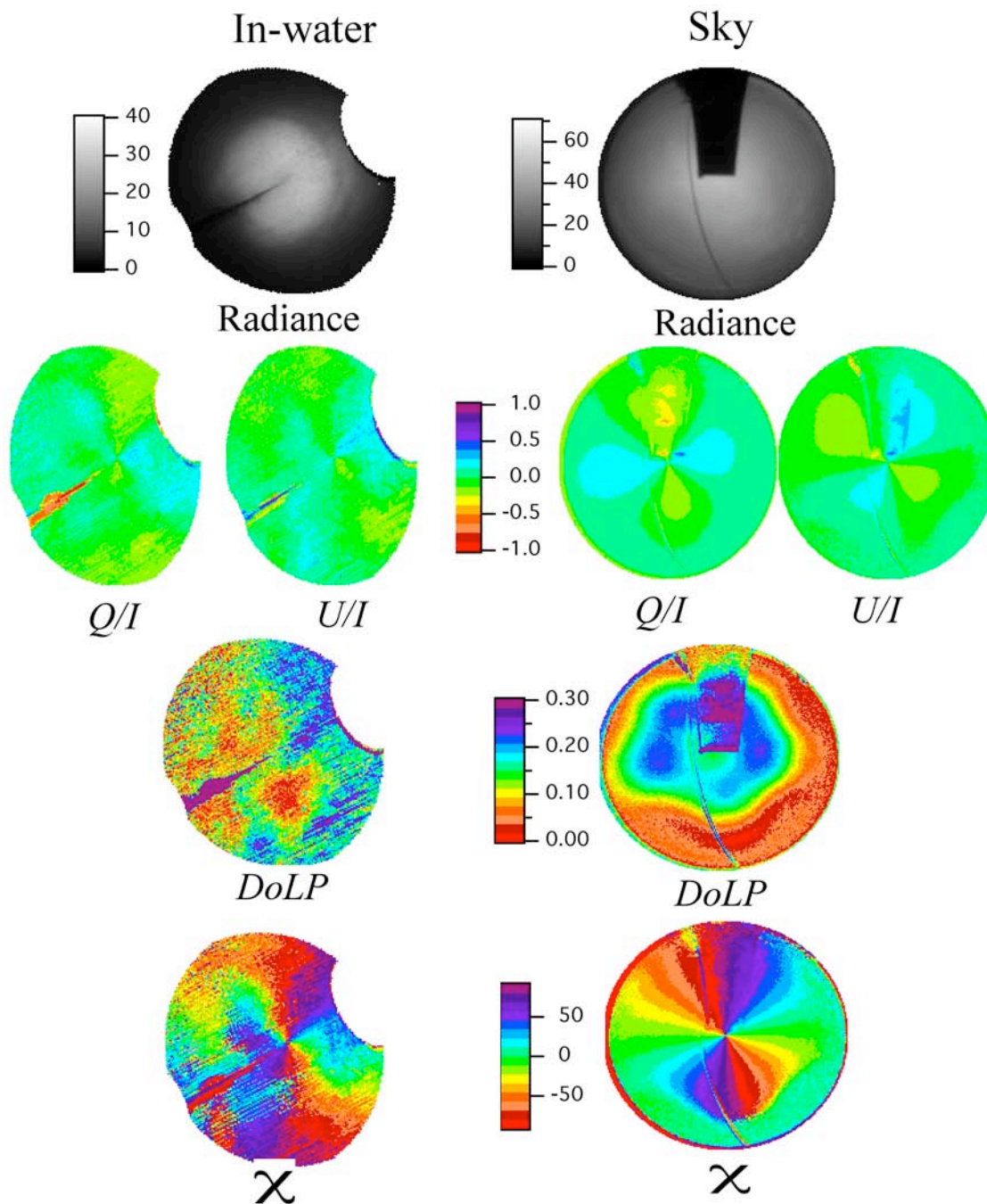


Fig. 7.1 Polarization behavior of the downwelling radiance light field during a cloudy day. The first column images correspond to the in-water data and the second column images are for the sky. The sun is barely visible, as can be seen in the radiance images (first row).

19:30:00 on September 13, 2008 (UTC) in SBC. The SZA is about  $31^\circ$ . The images in the first column are for in-water data (DPOL camera system) at 4 m depth and in the second column correspond to the sky data. The images have been rotated to place the sun on the top of all the images. In the radiance images (Fig 7.1, first row), the thick layer of clouds all around the sky can be clearly seen while the sun is barely visible. Comparing the  $Q/I$  and  $U/I$  images (Fig. 7.1, second row) with those during the clear sky (Fig. 6.2 and Fig. 6.7), we can see that the pattern is largely depressed due to the presence of cloud. The  $DoLP$  is only up to 22% in the sky data while that in the corresponding water reaches about 20% (Fig 7.1, third row). In the in-water image, the  $DoLP$  is higher around the horizon than at the zenith. Although  $Q/I$  and  $U/I$ , and the  $DoLP$  are greatly affected and reduced by the presence of clouds, the  $\chi$  (Fig. 7.1, fourth row) still has almost the same pattern as in the clear sky (Fig. 6.4).

In general though, looking through our data set, 40% of the cases are similar to the example shown above and in 60% of the data the pattern for  $\chi$  is fairly random. Thus while the clear sky pattern seems to be evident sometimes, it is clearly not there all the time. On the other hand, the sky measurements during the cloudy sky condition must be viewed carefully. This instrument is designed for the clear sky case, when the sky can be considered stable during the sequential measurement process. In most cases, the radiance under a cloud covered sky is not totally uniform, but varies depending on the detailed structure of the cloud. Since the clouds are often not stationary, this pattern varies during the measurement period and can show up as a larger degree of polarization, in probably a random  $\chi$  pattern. The DPOL system is designed to avoid this problem, and probably a more reliable measurement in this situation.

## 7.2. Elliptical Polarization

Ivanoff and Waterman (1958) showed the existence of elliptical polarization in the in-water light field due to the total internal reflection of linearly polarized light near the surface at a zenith angle slightly greater than the critical angle. Their results showed that the EP decreased when there were clouds in the sky, when the solar zenith angle is less than  $50^\circ$ , and when the slope of the sea surface is more than  $\pm 10^\circ$ . Although the DPOL (in-water camera) is characterized to measure the elliptical polarization of the light field, almost all of our data from SBC and Hawaii experiments did not show any clear areas of EP. In both of these experiments, however, the surface waves were generally large.

There was one case, during the SBC experiment, in which we saw a signature for elliptical polarization. This is shown in Fig 7.2. During these measurements the sky was overcast ( $SZA = 62^\circ$ ), the measurement was taken at 1 m depth, at 520 nm wavelength, and the wind speed was 4 m/s with a very calm (flat) water surface. Here, there was evidence of a  $V/I$  component right on the outside edge of the Snell's cone. As discussed earlier, the noise resulting from near surface measurement might have contributed to some of this  $V/I$ . At greater depths this  $V/I$  component disappeared, as it did at higher wind/sea state conditions.

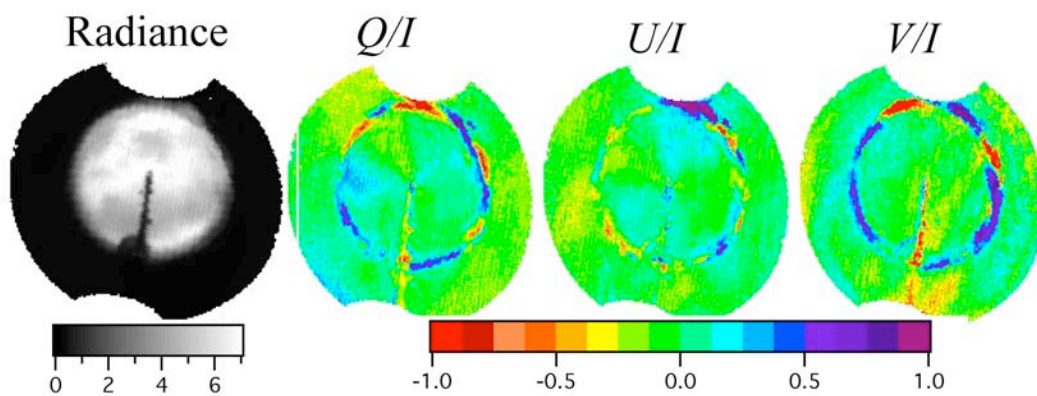


Fig. 7.2 Elliptical polarization signature found in SBC measurement at 1 m depth, when the sky was overcast, the wind speed was 4 m/s with a very calm (flat) water surface.

## CHAPTER 8. CONCLUSION

In this dissertation, a new polarimeter (DPOL camera system) that is capable of measuring all the four Stokes parameters of a polarized scene has been discussed in detail. Various aspects pertaining to the characterization of this instrument have been discussed, particularly a circular/elliptical polarization calibration to determine the 4 x 4 transformation matrix of the instrument. With this system each CCD image contains four fisheye images of a hemisphere and these images are used to calculate the 4 Stokes parameters, the  $DoP$  and the  $\chi$  of the downwelling polarized light field. After performing appropriate characterization and calibration steps, we determined that the expected accuracy of the radiance,  $Q/I$ ,  $U/I$  and  $V/I$  are 6%, 0.06, 0.06, and 0.07 respectively. The uncertainties of the derived  $DOP$  and  $DOLP$  are 0.05 and 0.04 respectively. The DPOL has been used in two field experiments; in Santa Barbara Channel (during September 9-23, 2008) and in Hawaii (during September 1-12, 2009). In these experiments, we also used a separate camera (Sky-Cam) to collect data on sky polarization simultaneous with DPOL. In this dissertation, I showed and compared the data and the results obtained from both of these camera systems from these experiments. From the data I have found that the radiance and polarization behavior of the light field in the water depended on various factors such as sky condition, waves at the air-sea interface, inherent optical properties of water, light wavelength, instrument's depth, viewing direction and position of the sun. I found that the polarization behavior of the light field in the water near the surface is dominated by the refracted sky light, and depends strongly on the wave-induced curvature of the water surface. Therefore, near the surface the polarization is

predominately inside the Snell's cone. At about one meter depth the maximum *DoLP*, for 520 nm, was found to be about 65%, similar to the skylight. Near the surface in clear water this *DoLP* was spectrally independent, however for more turbid waters, the path radiance from skylight decreases the *DoLP* in proportion to the available skylight. As one progresses in the water column the polarization due to light scattering by the water increases, thereby reducing the effect of refracted sky light. Thus, at increased water depths, the maximum in the *DoLP* moves from the refracted direction of  $90^\circ$  scattering in air, to 90-100 degree scattering angle in water, as expected from the oceanic Mueller matrix (Voss and Fry, 1984). The peak of the radiance also shifts towards the zenith away from the refracted solar position. This shift is more prominent when the water attenuation coefficient increases, as in coastal waters (SBC). The maximum *DoLP* also decreases with increasing depth. Our data showed that, at a comparable depth, the maximum *DoLP* in clear water is larger than in turbid water. Finally, I discussed the effect of clouds on the polarization of the light field. My data showed that during cloudy skies the polarization pattern of the light field is greatly affected and the magnitudes of the *Q/I* and *U/I* vectors and that of the *DoLP* were considerably decreased. However, there was no consistent  $\chi$  pattern under the cloudy sky conditions. This may be in part because our Sky-cam is not suited to rapidly changing light fields.

In spite of the difficulties encountered in the studies of light polarization in the dynamic ocean, the understanding of the general features and its role on aquatic animal behavior are emerging. However, there are still many issues to be answered properly, such as underwater communications sensing, polarization signaling, polarization camouflage, polarization vision and mechanisms by which polarization sensitive animals

detect, analyze and change the state of polarized light. To address some of these issues, it would be helpful to build a video polarimeter that could be used to study the animal behavior and polarization of light simultaneously.

**Acknowledgement:**

This project was supported by the Office of Naval Research (ONR) under RaDyO (Radiance under a Dynamic Ocean) program through contract N000140610720.

## REFERENCES

- Auburn, J. S., and D. H. Taylor (1979): Polarized light perception and orientation in larval bullfrogs *Rana catesbeiana*. *Anim. Behav.* **27**, 658-668.
- Aas, E. and N. K. Hojerslev (1999): Analysis of underwater radiance observations: apparent optical properties and analytic functions describing the angular radiance distribution, *J. Geophys. Res.* **104**, 8015-8024.
- Bhandari, P., K. J. Voss, and L. Logan (2010): The variation of the polarized downwelling radiance distribution with depth in coastal water, in *Ocean Optics Conference XX, 2010* Anchorage, Alaska.
- Boyd, R. W. (1983): *Radiometry and the Detection of Optical Radiation*, John Wiley & Sons, New York.
- Brines, M. L., and J. L. Gould (1982): Skylight polarization patterns and animal orientation, *J. Exp. Biol.* **96**, 69-91.
- Carol B. J., S. Bruce, E. A. Early, J. M. Houston, T. R. O'Brain, A. Thompson, S. B. Hooker, and J. L. Mueller (1995): The Fourth SeaWiFS Intercalibration Round-Robin Experiment (SIRREX-4), NASA Vol. **37**.
- Chandrasekhar, S. (1950): *Radiative Transfer*, Clarendon Press, Oxford.
- Coulson, K. L. (1988): *Polarization and Intensity of light in the atmosphere*, A. Deepak Publishing, Hampton, Virginia, USA.
- Cronin, T. W., N. Shashar, and L. B. Wolff (1994): Portable imaging polarimeters, in *Proc. 12<sup>th</sup> IAPR Int. Conf. on Pattern Recognition, Jerusalem, Israel, 9-13 October 1994*, 606-609.
- Dougherty, L. M., and A. Dollfus (1989): F. D. Arago's polarimeter and his original observation of extraterrestrial polarization in 1811, *J. of British Astronomical Association*.
- Egan, W. G. (1986): Proposed design of an imaging spectropolarimeter/photometer for remote sensing of earth resources, *Optical Engineering* **25**, 1155-1159.
- Gal, J., G. Horvath, V. B. Meyer-Rochow, and R. Wehner (2001): Polarization Patterns of the Summer Sky and its Neutral Points Measured by Full-Sky Imaging Polarimetry in Finish Lapland North of the Arctic Circle, *Proc. Royal Society London A***457**, 1385-1399.
- Goldstein, D. (2003): *Polarized Light Second Edition, Revised and Expanded*, Marcel Dekker, New York.

- Horvath, G., A. Barta, J. Gal, B. Suhai, and O. Haiman (2002): Ground-based full-sky imaging polarimetry of rapidly changing skies and its use for polarimetric cloud detection, *Appl. Opt.* **41**, 543- 559.
- Horvath, G., and D. Varju (1995): Underwater refraction-polarization patterns of skylight perceived by aquatic animals through Snell's window of the flat water surface, *Vision Res.* **35**, 1651-1666.
- Horvath, G., and D. Varju (2004): *Polarized Light in Animal Vision*, Springer, *New York*.
- Ivanoff, A. (1974): *Optical Aspects of Oceanography*, edited by N. G. Jerlov and E. Steemann Nielsen, *Academic Press, ed.*, 151-175.
- Ivanoff A., and T. H. Waterman (1958): Elliptical polarization of submarine illumination, *J. Mar. Res.*, **16**, 255-282.
- Jerlov, N. G., and M. Fukuda (1960): Radiance distribution in the upper layers of the sea, *Tellus*, **12**, 348-355.
- Kattawar, G. W., and C. N. Adams (1989): Stokes vector calculations of the submarine light-field in an atmosphere-ocean with scattering according to a Rayleigh phase matrix - Effect of interface refractive-index on radiance and polarization, *Limnol. Oceanogr.*, **34**, 1453-1472.
- Kattawar, G. W., and G. N. Plass (1972): Degree and direction of polarization of multiple scattered light. 1: homogeneous cloud layers, *Appl. Opt.* **11**, 2851-2865.
- Kokhanovsky, A. A. (2008): Optical remote sensing of atmospheric aerosol, in *Aerosol Optics: light absorption and scattering by particles in the atmosphere*, Springer
- Konnen, G. P. (1985): *Polarized light in nature*, Cambridge Univ Press, Cambridge, 40-43.
- Liu, Y. (1996): Measurement of the intensity and polarization of light in the atmosphere, *Ph. D. dissertation, University of Miami, FL*.
- Maximov, V. V. (2000): Environmental factors which may have led to the appearance of color vision, *Philos. Trans. R. Soc. London Ser. B* **355**, 1239-1242.
- Miyamoto, K. (1964): Fisheye lens, *J. Opt. Soc. Am.* **54**, 1060-1061.
- Mobley, C. D. (2000a): Radiative Transfer in the Ocean, Invited chapter in *Encyclopedia of Ocean Science*, Academic Press.
- North, J. A., and M. J. Duggin (1997): Stokes vector imaging of the polarized sky-dome, *Appl. Opt.* **36**, 723-730.

- Pust, N. J. and J. A. Shaw (2008): Digital all-sky polarization imaging of partly cloudy skies, *Applied Optics*, Vol **47**.
- Sabbah, S., and N. Shashar (2006): Underwater light polarization and radiance fluctuations induced by surface waves, *Appl. Opt.*, **45**, 4726-4739.
- Schenck, H. (1957): On the focusing of sunlight by ocean waves, *J. Opt. Soc. Am.*, **47**, 653 – 657.
- Sekera, Z. (1957): Light scattering in the atmosphere and the polarization of skylight. *J. Opt. Soc. Am.* **47**, 484-490.
- Shashar, N., T. W. Cronin, G. Johnson and L. B. Wolff (1995): Portable imaging polarized light analyzer, *Proc. SPIE* **2426**, 28-35.
- Shashar, N., S. Sabbah, and T. W. Cronin (2004): Transmission of linearly polarized light in seawater: implications for polarization signaling, *J Exp Biol*, **207**, 3619-3628.
- Shaw, G. E. (1975): Sky brightness and polarization during the 1973 African eclipse. *Appl. Opt.* **14**, 388-394.
- Shettle, E. P. and R. W. Fenn (1979): Models for the Aerosols of the lower atmosphere and the effects of humidity variations on their optical properties, *Optical Physics Division, Air Force Geophysics Laboratory*.
- Shuleikin, V. V. (1933): Data on the optics of a strongly scattering medium, applied to sea water, fog and cloud, *Geofizika*, **3**, 3-5.
- Stokes, G. C. (1852): On the composition and resolution of streams of polarized light from different sources, *Trans. Cambridge Philos. Soc.* **9**, 399–416.
- Synder R. L., and J. Dera (1970): Wave-induced light-field fluctuations in the sea, *J. Opt. Soc. Am.* **60**, 1072-1079.
- Timofeeva, V. A. (1962): Spatial Distribution of the degree of polarization of natural light in the sea, *Izv. Acad. Sci. USSR Geophys. Ser.* **12**, 1160-1164.
- Timofeeva, V. A. (1974): Optics of turbid waters (Results of laboratory studies), in *Optical Aspects of Oceanography*, edited by N. Jerlov and E. Nielsen, *Academic Press, London*, 177-219.
- Tyler J. E. (1960): Radiance Distribution as a Function of Depth in an Underwater Environment, *Scripps Inst. Oceanogr. Bull.* **7**, 369-386.
- Tyo, J. S., D. L. Goldstein, D. B. Chenault, and J. A. Shaw (2006): Review of passive imaging polarimetry for remote sensing applications, *Applied Optics*, **45**, 5453 – 5469.
- van de Hulst, H. C. (1981): Light scattering by small particles, *Dover, New York*.

- Voss, K. J. (1989): Electro-optic camera system for measurement of the underwater radiance distribution, *Optical Engineering*, **28**, 241-247.
- Voss, K. J. (1989b): Use of the radiance distribution to measure the optical absorption coefficient in the ocean, *Limnol. and Oceanography*, **34**, 1614-1622.
- Voss, K. J., P. Bhandari, L. Logan (2008): A new spectral polarized radiance distribution camera system, DPOL, *Ocean Optics XIX, Barca, Italy*.
- Voss, K. J., and A. L. Chapin (2005): Upwelling radiance distribution camera system, NURADS, *Opt. Express*, **13**, 4250 – 4262.
- Voss, K. J., and E. S. Fry (1984): Measurement of the Mueller matrix for ocean water, *Appl. Opt.*, **23**, 4427-4439.
- Voss, K. J., and Y. Liu (1997): Polarized radiance distribution measurements of skylight: I. system description and characterization, *Appl. Opt.*, **36**, 6083-6094.
- Voss, K. J., A. Morel, and D. Antoine (2007): Detailed validation of the bidirectional effect in various Case 1 waters for application to ocean color imagery, *Biogeosciences*, **4**, 781-789.
- Voss, K. J., and N. Souaidia (2010): POLRADS: polarization radiance distribution measurement system, *Opt. Express*, **18**, 19672-19680.
- Voss, K. J., and G. Zibordi (1989): Radiometric and geometric calibration of a spectral electro-optic “fisheye” camera radiance distribution system, *J. Atmosph. and Ocean. Techn.*, **6**, 652-662.
- Walraven, R. L. (1981): Polarization Imagery, *Optical Engineering*. **20**, 14-18.
- Waterman, T. H. (1954): Polarization patterns in submarine illumination, *Science*, **120**, 927-932.
- Waterman, T. H. (1955): Polarization of scattered sunlight in deep water, *Deep-Sea Res.*, **426-434**.
- Waterman, T. H. (2006): Reviving a neglected celestial underwater polarization compass for aquatic animals, *Biological Reviews*, **81**, 111–115.
- Wolff, L. B. (1994): Polarization camera for computer vision with a beam splitter, *J. Opt. Soc. Am. A***11**, 2935-2945.
- Wolff, L. B., and A. G. Andreou (1995): Polarization camera sensors, *Image Vision computing*, **13**, 497 – 510.
- You, Y., G. W. Kattawar, K. J. Voss, P. Bhandari, C. J. Zappa (2011): Polarized light field under dynamic ocean surfaces: numerical modeling compared with measurements, *J. Geophys. Res.*.

You, Y., P.-W. Zhai, G. W. Kattawar, and P. Yang (2009): Polarized radiance fields under a dynamic ocean surface: a three-dimensional radiative transfer solution, *Appl. Opt.*, **48**, 3019-3029.

Young, T. (1804): Experiments and Calculations Relative to Physical Optics, *Proc. Roy. Soc. Long. A* **94**, 1-16.